A Pore-Scale Study on Cyclic Flows in Porous Underground Hydrogen Storage

Celine Marie Solstad

Department of Physics and Technology
University of Bergen

June 1, 2022

The master's thesis is written as a part of the Integrated Master's programme in Energy at Geophysical Institute at the University of Bergen.

Abstract

A solution for energy storage is needed to balance supply and demand in future energy markets with an increased share of fluctuating renewable wind and solar energy. A key enabler is large-scale, seasonal energy storage, where porous underground formations are suitable storage solutions. An experimental pore-scale study was performed with the objective to investigate hydrogen flow, gas saturations, residual trapping and contact angles in porous media. Hydrogen injections were performed on a water saturated two-dimensional micromodel with pore network based on a natural sandstone relevant for underground hydrogen storage in an aquifer. The effect of capillary number on primary drainage and cyclic hydrogen injection was studied with a pore pressure of 40 bar and room temperature. An image segmentation algorithm was developed to extract gas saturation from microscope images of the pore space. A sensitivity analysis showed that the image segmentation algorithm had on average a relative uncertainty of 12%, predominantly caused by water accumulations and uneven light source distribution. During primary drainage the hydrogen saturation increased for increasing capillary numbers. During imbibition the hydrogen saturation decreased until it stabilised at the residual gas saturation, where hydrogen was disconnected from the main flow, immobile and unable to recover. Static contact angles for primary drainage and imbibition varied between 19 to 71°. Local gas displacement through the field of view was observed during drainage and imbibition, resulting in fluctuating hydrogen saturation despite an expected increase for drainage and decrease for imbibition. Experiments showed that gas recovery should increase for higher capillary number, but a lower recovery was observed for the highest capillary number caused by local displacement through the field of view.

Cyclic injections were performed at different capillary numbers and the development in hydrogen saturation was studied. Local gas displacements in and out of the field of view affected the end-point hydrogen saturation for each cycle. The end-point hydrogen saturation showed hysteresis where both gas development and end-points varied between cycles and repeated injections with equal capillary numbers. The gas saturation dependency on capillary number was weaker when gas was injected over several cycles. The relationship between increased gas saturation with increased capillary number was weaker for cyclic injections compared with primary drainage.

Hydrogen loss during cyclic injection was studied by identifying the overlapping hydrogen distribution during drainage and imbibition. Trapped gas relative to initial gas saturation after drainage decreased with increasing capillary number. The results indicated increasing trapped gas with increasing cycles, but no clear trend was observed.

Acknowledgements

I would like to thank my supervisors Professor Martin Fernø, Post-doc Na Liu and Associate Professor Velaug Myrseth Oltedal for guidance during the last year of my studies. I am grateful that I got the opportunity to be a part of the the exciting research project in the reservoir group at the University of Bergen. I would like to thank the reservoir group for feedback and discussion that increased the quality of my work.

A special thanks to Martin and Na for guidance in the completion of my master thesis. I would like to thank Na for assistance in the laboratory and discussion of the results of the experiments.

Thanks to my classmates for friendship and support during my five years at the University of Bergen.

Celine Marie Solstad
Bergen, June 2022

Nomenclature

θ	Contact angle	[°]
ϕ	Porosity	-
σ	Inter facial tension	[N/m]
%vol	percent by volume	-
%rel	percent relative uncertainty	-
N_c	Capillary Number	-
P	Pressure	[bar]
Q	injection rate	[ml/h]
S_g	Hydrogen gas saturation	[frac]
$S_{g,dr}$	Drainage gas saturation	[frac]
$S_{g,imb}$	Imbibition gas saturation	[frac]
S_r	Residual gas saturation	[frac]
$S_{r,all}$	Residual gas saturation present in all cycles	[frac]
S_w	Water saturation	[frac]
U	Darcy velocity	[m/s]
R_f	Hydrogen recovery	[%]
u(x)	Uncertainty to the parameter x	[unit of x]
$u_R(x)$	Relative uncertainty to the parameter	[%]

Abbreviations

CCS	Carbon Capture and Storage
CDC	Capillary Desaturation Curve
CH_4	Methane
CO_2	Carbon dioxide
GSm^3	Giga standard cubic meter
HVDC	High Voltage Direct Current
H_2	Hydrogen
IFT	Interfacial Tension
kWh	kilowatt hour
PEEK	Polyether Ether Ketone
PV	Pore Volumes
TWh	Terrawatt hour
UHS	Underground Hydrogen Storage

Contents

Chapter 1

Introduction

Norway needs to reduce the Carbon dioxide(CO_2) emissions by 55% by 2030 compared with 1990 levels to achieve its climate targets, with a further reduction down to net zero by 2050[1]. Therefore, an increase of renewable energy sources like hydropower, wind, and solar energy in the energy mix is urgent to fulfil the decarbonisation targets. Due to the strongly fluctuating behaviour of renewable sources, such as wind speed and sunlight, a solution for energy storage is needed to balance supply and demand in new energy markets. Hydrogen (H_2) as an energy carrier can be produced from renewable sources by Power-to-H_2 technologies, then stored in nearby underground formations and withdrawn to convert to electricity when the electricity demand is high. Large-scale and inter-seasonal storage solutions will be required to enable hydrogen as a low-carbon energy pathway.

Underground geological structures such as depleted oil and gas reservoirs, aquifers and salt caverns can be used for large scale seasonal gas storage [2]. An underground gas storage facility uses the natural trapping mechanisms of the geological environment. Gas can be injected into geological structures, where the storage capacity of both aquifers and reservoirs is dependent on available pore space. Salt caverns have been considered as a more feasible and flexible solution for pure hydrogen storage, however the storage capacity of salt caverns is typically only 10% of the area of depleted reservoirs [3]. Hydrogen has been stored successfully in three salt cavern locations in Texas (1983) and Teeside (1972) [4]. Saline aquifers may be suitable for gas storage with available large-scale storage capacity, but have not been proven to trap hydrogen and must be developed. Depleted oil and gas reservoirs are the most commonly used underground gas storage sites because of their wide availability and existing infrastructure. Most of the necessary installations and systems for injection and storage are already in place, resulting in lower investment costs for reservoirs than for other structures [5]. To enable H2 as an energy transition in future, the storage capacity of geologic formations is significantly important, especially for depleted gas reservoirs, where the potential volume could easily up to 250 GSm^3[6]. Even though a large number of studies focus on geological storage CO_2 and natural gas in depleted gas/oil reservoirs and aquifers, there is very little literature on the potential challenges of underground hydrogen storage(UHS). As the physico-chemical properties of hydrogen are different with CO_2 and methane(CH_4), mechanisms of hydrogen flow in porous media must be considered before UHS can be realised. Challenges of using depleted gas/oil reservoirs as storage sites are connected to biogeochemical, physiochemical, hydrodynamics, and microbial activities in porous media. The formation tightness is also

different for hydrogen than methane due to the small hydrogen molecule and increased possibility of gas migration into smaller fractures. Hydrogen flow behaviour and residual hydrogen trapping determine the working gas capacity, hence the hydrogen recovery from the formation. Residual hydrogen trapping occurs when the hydrogen is disconnected from the main flow into immobile, disconnected hydrogen bubbles that cannot be withdrawn, reducing the recovery efficiency. Gas migration and residual trapping is discussed for CO_2 storage [7],[8], but is not described for aquifer or reservoir UHS. Disconnected hydrogen bubbles may be reconnected and mobilised during cyclic H_2 injection. The effect is known as hysteresis and is described for hydrogen storage in nano-porous carbon tubes[9] and for cyclic CO_2 injection in porous media[7], but is not described for cyclic H_2 injection, as of the author's knowledge. The coexistence of cushion gas, water and CH4 and hydrogen should be addressed to study the hydrogen behaviour and residual trapping when other fluids are present. In addition, a mixture of formation fluids and hydrogen will be produced during the withdrawal of hydrogen for depleted reservoirs and aquifers, affecting the hydrogen purity. The amount of hydrogen loss by dissolution in water, biochemical reactions and microbial activities must also be quantified to identify the potential effect on hydrogen recovery. The study in this thesis focused on pore-scale mechanisms of hydrogen flow during UHS in porous media. Lab-scale experiments have been performed using a high-pressure two-dimensional micromodel to study gas saturation, residual trapping and contact angles during primary drainage, primary imbibition and cyclic injection. The results lead to the identification of reservoir storage capacity, potential losses and wettability changes during hydrogen storage in aquifers. The results of this study can give valuable insight into pore-scale behaviour of hydrogen in porous media of two-phase immiscible fluids for UHS.

Pore-scale mechanisms of hydrogen flow during UHS in porous media will be addressed to study hydrogen behaviour in a water filled aquifer. Lab-scale experiments have been performed using a high-pressure two-dimensional micromodel to study gas saturation, residual trapping and contact angles during primary drainage, primary imbibition and cyclic injection. The results lead to the identification of reservoir storage capacity, potential losses and wettability changes during hydrogen storage in aquifers. The results of this study can give valuable insight into pore-scale behaviour of hydrogen in porous media of two-phase immiscible fluids for UHS.

Chapter 2

Background

2.1 Future energy market

Forecasts on energy demand

The European Union has set a goal of net zero carbon emission by 2050, an ambitious target that requires changes for both consumers and industry. The emission target is necessary to limit the global average temperature in accordance with the 2°C or below target set in the Paris Agreement in 2015. The energy sector is responsible for 3/4 of the global greenhouse gas emissions, and clean and efficient energy technology is required to meet the targets [10]. Rapid deployment of solar and wind technologies is expected, and an increase in Norwegian solar capacity has already been observed, partly caused by high electricity prices [11]. IEA forecasts an additional capacity of 630 GW of solar photovoltaics and 390 GW of wind capacity by 2030 compared to 2020 level. Innovation of new technologies will also be important in the next decades. It is expected that technologies in the demonstration or prototype phase today will be important contributors in the reduction of emissions in the future.

Technology development in hydrogen, batteries and direct air capture and storage will have an important role in reducing CO_2 emissions between 2030 and 2050. New technologies and electrification will lead to higher electricity consumption in 2050: electricity will be responsible for almost 50% of the total energy consumption, requiring an increase of 2.5 times the total electricity generation in 2021 [10]. The petroleum industry has to follow new paths when investments and profitability in fossil fuels are reduced. IEA reports that there will be no need for investments in new fossil fuel supply in their net zero pathway, but it is expected that the annual investment in CO_2 pipelines and hydrogen infrastructure will increase from $1 billion in 2021 to around $40 billion in 2030.

The key feature of hydrogen as an energy carrier is the ability to store variable renewable energy. Renewable energy production cannot follow market demand due to the fluctuating energy sources, and energy is lost if the production is higher than the demand if the system is not connectd to storage solutions. Net Zero 2050 forecasts a need for 70 GW installed offshore wind globally, and the global hydrogen use is expected to increase from 90Mt in 2020 to more than 200 Mt in 2030. Offshore wind has higher capacity factors and lower variability than onshore wind and solar photovoltaics and has the potential to become an important contributor to future energy production [12]. Hydrogen can be produced

offshore for storage of offshore wind, but offshore hydrogen production is a relatively new concept without commercial experience as of today. Nevertheless, the competence from the oil and gas sector could be used directly within offshore hydrogen. It is forecasted that hydrogen production and demand will increase rapidly during the next decades [13], and an upscale of the hydrogen production will expand both market and infrastructure. In addition, roughly estimated, 1/3 of the produced green hydrogen and 20% of produced low carbon hydrogen must be stored before use in 2030, demanding about 3 million tonnes of hydrogen storage capacity [14].

Power system flexibility is a critical factor for the use of renewable energy. Variable renewable energy demands flexibility, including storage solutions for grid balancing at peak demand and storage when production exceeds the demand. Renewable wind and solar energy cannot follow demand patterns and must be balanced using energy carriers to sustain energy security. Flexible operation requires flexible storage solutions, like batteries and hydrogen. The Net Zero 2050 report forecasts an electricity demand for hydrogen production at 12 000TWh in 2050. Storage solutions that complement batteries must be developed and commercialised, and it will be necessary to develop low-carbon hydrogen industries to address climate change and energy security. The key element could be hydrogen combined with storage technologies that enables long term and seasonal storage [10].

2.2 Hydrogen

Properties and characteristics

Hydrogen is the most common element on Earth but rarely occurs naturally alone. Hydrogen atoms exist as components of other molecules and can be produced from water or hydrocarbons. The main properties of hydrogen are given in Table 2.1. Hydrogen can be produced from renewable energy by the water electrolysis reaction given in Formula 2.1, while Formula gives hydrogen production from natural gas (CH_4)2.2:

$$2H_2O \rightarrow 2H_2 + O_2 \tag{2.1}$$

$$CH_4 + 2H_2O + heat \rightarrow 4H_2 + CO_2 \tag{2.2}$$

Hydrogen is a colourless gas, but a colour categorisation is often used to clarify the production method [15]. Grey hydrogen is produced from fossil fuels without Carbon Capture and Storage (CCS), while blue hydrogen is produced from fossil fuels with CCS technology. Green hydrogen is produced from renewable energy, either directly from renewable sources or with renewable electricity from the grid. It is forecast that the hydrogen production in 2050 will be a combination of green and blue hydrogen to ensure a relatively quick increase in total hydrogen production. An increased share of green hydrogen is expected within 2050 in correlation with policy support, cost reduction and renewable energy capacity[16]. However, the production cost is expected to be lower for blue hydrogen in the first time period [17], and a combination of hydrogen produced from renewable energy and fossil fuels with CCS is expected to accelerate the hydrogen market [16].

Hydrogen properties and characteristics are important for understanding fluid behaviour and for security reasons. Hydrogen is an energy carrier, and the energy can be released

Table 2.1: Hydrogen properties [18].

Properties	**Hydrogen**
Molecular weight	1.008 g/mol
Boiling point	-253°C
Energy density	33.3 kWh/kg
Density at STP	0.09 kg/m^3
Density at 350bar(700bar)	31.5 kg/m^3(63 kg/m^3)
Flammability in air	4-75%vol
Ignition energy	0.017mJ

through combustion or chemical reactions. Hydrogen has the highest gravimetric energy density (kWh/kg) compared to traditional energy carriers like fossil fuels, batteries and methanol, but the low volumetric energy (kWh/L) is a disadvantage for transport and storage footprint. Hydrogen is self-igniting at 4-75 % by volume in air with ignition energy at 0.017mJ. In comparison, CH_4 is flammable with a concentration at 5-15%vol in air, a range 6-7 times narrower than for hydrogen. In addition, hydrogen has 15-20 times lower ignition energy and 6-7 times higher burning velocity than CH_4 [18]. The hazards for hydrogen explosion in air are greater than for CH_4 due to larger pressure, shock wave speed and flame propagation speed for a hydrogen/air explosion [19]. Traditional mitigation methods like venting or gas detection equipment will generally be too slow and would not work for hydrogen due to flammability and explosions properties, and hydrogen must be handled differently than traditional fuels where the focus should be on prevention leakage rather than leakage handling. However, an outdoor release would have a lower risk for hydrogen due to buoyancy and dilution if leakage occurs [18].

Offshore hydrogen production

There is a large potential in offshore hydrogen production due to high offshore wind capacities. The capacity factor of a power generation system is used to describe the average power produced relative to maximal capacity. Offshore wind has high energy potential due to high capacity factor, high average wind speeds [20] and reduced turbulence due to less obstacles offshore. Today, the capacity factor of onshore wind parks could be up to 40%, but an offshore installation could have a capacity factor up to 60 %[21]. In comparison, a typical capacity factor of solar photovoltaics is between 10 to 30%, with large variations in power production between summer and winter [22],[23]. Seasonal variations were observed for both wind and solar energy, where wind energy has highest capacity factor during winter and solar energy during summer. Offshore and onshore wind have a similar hourly variability in power output with hourly variability up to 20%, a narrower band than solar photovoltaics with typical fluctuations up to 40% [21]. Hydrogen can be produced offshore when the electricity demand is low to exploit the full potential of the variable renewable energy. Electricity transmission is an alternative to offshore hydrogen production, but the energy loss is estimated to be lower for hydrogen transport in pipelines compared to electricity transmission through cables to shore. An energy loss of 0.2 - 0.4 % was estimated for hydrogen transport in pipelines, while an offshore wind farm with HVDC cables to shore would have an average energy loss of ∼2.2% [24]. Nevertheless, offshore hydrogen production is still in its initial state, and the value chain is under development. Hydrogen produced offshore could potentially be stored in storage tanks on

platforms or on the sea bottom, or stored in nearby underground formations.

Hydrogen Storage Technologies

Hydrogen can be stored in different states and time perspectives. The most common storage technology is storage tanks, where hydrogen is compressed to increase volumetric density. Steel is a common material for pressurised gas storage, but lighter composite material would be preferred for hydrogen storage tanks where weight is essential[25]. Hydrogen can also be liquefied, but the process is energy consuming and requires cryogenic equipment due to the low boiling point (-253°C)[24]. Other opportunities are converting hydrogen to other chemical components like ammonia (NH_3) and liquid organic hydrogen carriers (LOHC), which can be stored in traditional storage tanks. It is also expected that hydrogen can be stored in geological formations similarly to CH_4 and CO_2. The volumetric density is a challenge for hydrogen storage, but UHS enables large-scale, seasonal energy storage in the range of 100 to 1000 MW [26]. Nevertheless, the small size of the hydrogen molecule can cause trouble and hydrogen behaviour must be studied. In terms of underground storage, the tightness of the reservoir could act differently when hydrogen is present. Safety, small surface footprint and availability of geological structures are some of the advantages of UHS compared to traditional storage tanks [5].

2.3 Underground gas storage

2.3.1 Gas storage in porous media

Gas can be injected into underground formations and stored under pressure. Gas will be compressed when injected into the reservoir due to the pressure increase with depth, and the reservoir pressure will increase when volumes are injected. It is important not to exceed the fracture pressure to avoid fractures in the formation. Fractures will reduce the tightness of the reservoir seal and could result in gas leakage. Hydrogen could easily diffuse in small fractions due to the small molecular size, where the tightness could act differently for hydrogen than for natural gas. The pressure gradient between the reservoir and the wellhead drives the extraction of the stored gas. If the pressure drops below the pressure at the wellhead, the pressure gradient will change direction, and the gas flow to the production well will stop. A certain amount of gas must be left in the reservoir to maintain a pressure gradient and cannot be extracted to maintain a minimum pressure in the reservoir. The permanently stored gas is called cushion gas, while the withdrawn gas is called the working gas [26] and defines the available capacity of the reservoir. Table 2.2 gives the typical working gas/cushion gas ratio for different geological formations. The working gas can be extracted between the minimum pressure and the maximums pressure of the reservoir. Storage in porous media is most suitable for seasonal and large scale storage due to flow resistance when the fluid is moving through the formation [27]. The residual CH_4 from depleted reservoirs can be used as cushion gas for hydrogen storage, but miscibility, diffusion and density must be considered in the choice cushion gases [28]. In contrast to permanent CO_2 storage, hydrogen storage is temporary, and, ideally, all stored gas could be extracted. However, disconnected hydrogen will be residual trapped in the pore space in a depleted gas reservoir and cannot be recovered. Residual gas and cushion gas will be miscible with injected hydrogen, and it is expected that the recovered hydrogen also contains proportions of other gases.

Table 2.2: Typical working/cushion gas ratio for different formations [26][5],[4].

	Salt caverns	Aquifer	Depleted Hydrocarbon Reservoir
Working gas ratio	70-80%	∼20%	40-50%
Cushion gas ratio	20-30%	∼80%	50-60%

An underground storage facility uses the natural trapping mechanisms of the geological environment. A suitable formation for gas storage has high porosity and high permeability. Effective porosity describes the storage capacity of the porous media and is defined as the ratio of connected pore volumes and the total reservoir volume. The recovery from the reservoir is also dependent on permeability, a measure of the ability to the porous media to transmit fluids. The high porosity enables storage of large volumes in the formation, while a high permeability indicates that the fluid can easily be transmitted through the formation. Porosity and permeability are not necessarily correlated, and a high porosity does not necessarily indicate high permeability and vice versa. Typical formations and rocks with these features are sandstones, limestones and conglomerates, and typical reservoir types are saline aquifers and depleted hydrocarbon reservoirs [26]. An illustration of storage opportunities for UHS is shown in Figure 2.1.

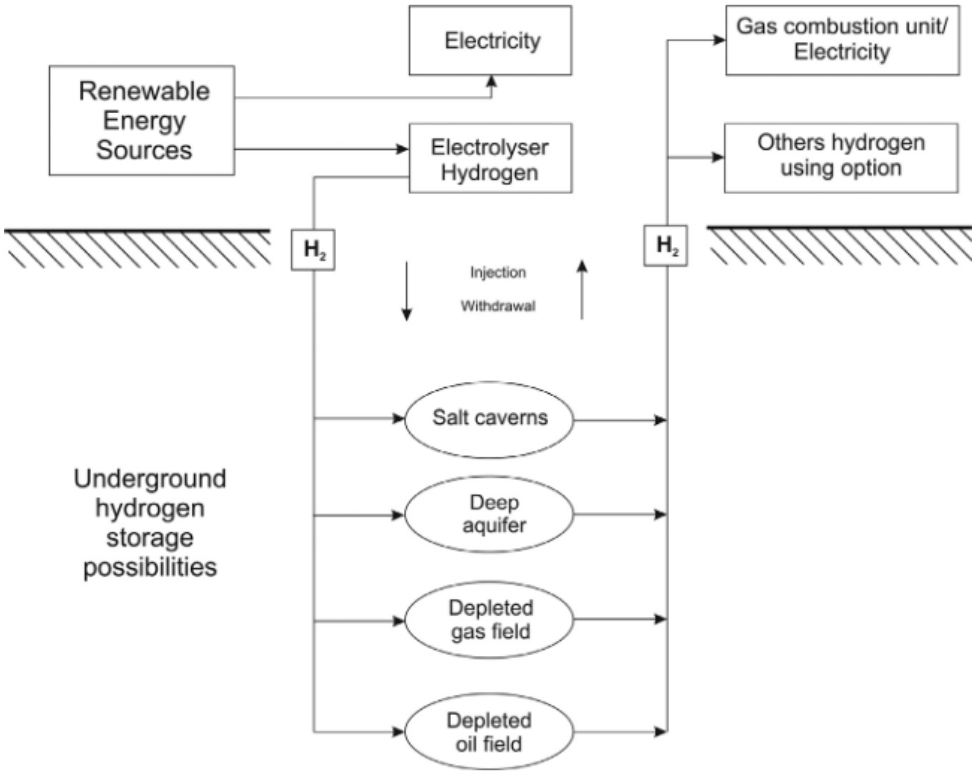

Figure 2.1: Schematic illustration for storage opportunities for a underground hydrogen storage facility [5].

Underground geological structures such as depleted oil and gas reservoirs, aquifers and salt caverns can be used for large scale seasonal gas storage [2]. An aquifers have similar characteristics as a depleted reservoir, but fresh or saline water fills the pore space, and hydrogen cannot ignite in such a structure due to the absence of oxygen [5]. Salt caverns have been considered as a more feasible and flexible solution for pure hydrogen storage, however the storage capacity of salt caverns is typically only 10% of the area of depleted reservoirs [3]. Depleted hydrocarbon reservoirs and natural aquifers may be suitable for natural gas storage with available large-scale storage capacity, but have not been proven to trap hydrogen and must be developed. The current experience in UHS is restricted to storage in salt caverns and storage of town gas. Hydrogen has been stored successfully in three salt cavern locations in Texas(1983) and Teeside(1972) [5]. Town gas, a gas mixture of CH_4, H_2, CO_2, carbon monoxide and nitrogen, has also been stored in depleted gas fields and aquifers since the middle of the 1900s in countries like the Czech Republic, France and Germany [29], [30], [31]. Table 2.3 gives an overview of the maturity for underground storage types for different gases.

Table 2.3: Suitability and maturity for different storage type, adapted from [32].

Storage types	CH_4	H_2	CO_2
Depleted hydrocarbon reservoirs	*	v	o
Aquifers and traps	*	v	o
Salt caverns	*	o	-
Abandoned Mines	v	-	-
Engineered cavities, host rocks	o	v	-

Legend: *:mature, widely implemented; o Proven, sparsely implemented; v:prospective: pre-commercial pilots and conceptual designs; -: not forseen to take place.

Hydrogen characteristics and behaviour in porous media must be considered before UHS can be realised. There is a gap in knowledge on the potential challenges of UHS in depleted reservoirs and aquifers, where the challenges are connected to gas mitigation, residual trapping, gas contamination and gas mixing. The formation tightness is different for hydrogen than CH_4 due to the small hydrogen molecule and increased possibility of gas migration into smaller fractures. Hydrogen flow behaviour and residual hydrogen trapping determine the working gas capacity, hence the hydrogen recovery from the formation. Residual hydrogen trapping occurs when the hydrogen is disconnected from the main flow into immobile, disconnected hydrogen bubbles that cannot be withdrawn, reducing the recovery efficiency. Gas migration and residual trapping is discussed for CO_2 storage [7],[8], but is not described for aquifer or reservoir UHS. Disconnected hydrogen bubbles may be reconnected and mobilised during cyclic H_2 injection. The effect is known as hysteresis and is described for hydrogen storage in nano-porous carbon tubes [33] and for cyclic CO_2 injection in porous media [7], but is not described for cyclic H_2 injection, as of the author's knowledge. The coexistence of cushion gas, water and CH_4 and hydrogen should be addressed to study the hydrogen behaviour and residual trapping when other fluids are present. In addition, a mixture of formation fluids and hydrogen will be produced during the withdrawal of hydrogen for depleted reservoirs and aquifers, affecting the hydrogen purity. The amount of hydrogen loss by dissolution in water, biochemical reactions and microbial activities must also be quantified to identify the potential effect on hydrogen recovery. The study of flow functions, residual trapping, biochemical reactions

and hydrogen loss is needed to determine the working gas capacity for UHS.

2.3.2 Drainage and imbibition

A drainage is performed when hydrogen is injected into water wet porous formations. Wettability is "the tendency of one fluid to spread on or adhere to a solid surface in the presence of other immiscible fluids" [34], where the water is the wetting fluid for a water wet formations. Historically, a reservoir was initially water wet and 100% water saturated before hydrocarbons migrated into the formation millions of years ago. A minimum pressure called the threshold pressure is needed for hydrogen to displace water in a water wet system, where the threshold pressure is dependent on pore radius and pressure difference between hydrogen and water. A primary drainage is performed hydrogen when hydrogen is stored in an 100% water or brine saturated aquifer [35].

The process where water displaces hydrogen stored in an water wet aquifer is called imbibition. Water will flow into the small and medium-sized pores with high capillary pressure during imbibition, while hydrogen will be transported to larger pores where hydrogen is easier displaced. Capillary pressure is the difference between hydrogen and water pressure in the pore space and will be described in the next chapter. Hydrogen that is trapped in the formation after imbibition is called residual gas, and is present as immobile disconnected hydrogen bubbles or clusters. Most gas will be recovered during water breakthrough, where most gas is displaced by the waterfront. Almost all remaining gas would be immobile when the waterfront has passed the smaller pores and channels, a mechanism called by-pass. The residual gas will typically be disconnected gas clusters extending over several pores or gas bubbles in small pores or in the centre of larger pores. Residual gas in smaller pores could block pore throats and reduces local relative water permeability [35].

The wettability during drainage and imbibition can evaluated by measuring the static contact angle θ between the hydrogen interface and the grain surface as illustrated in Figure 2.2. The relationship between wettability and contact angles is found in Table 2.4.

Wettability	Contact angle
Strongly water wet	0°
Neutral water wet	90°
Strongly oil wet	180°

Table 2.4: Wettability classification and contact angle.

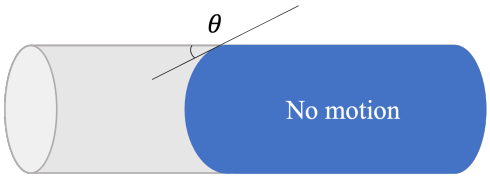

Figure 2.2: Shematic illustration of the static contact angle in a capillary tube.

2.3.3 Capillary pressure and residual trapping

Residual gas is caused by capillary trapping and structural trapping. Capillary trapping is a mechanism that occur due to the capillary pressure in the pore channels. The capillary pressure is defined as the pressure difference between the non-wetting and wetting fluid in a capillary tube and is dependent on wettability, saturation history and pore structure. The capillary pressure can be expressed by the Laplace equation:

$$P_c = \frac{2\sigma cos\theta}{r} \tag{2.3}$$

where σ [N/m] is the gas-water IFT, θ is the contact angle and r[m] is the pore radius, and the relation shows that the capillary pressure increase with decreasing pore radius. Hysteresis effect is observed where multiphase flow characteristics change for drainage and imbibition under equal conditions [36].The capillary pressure/gas saturation relationship is dependent on wettability, pore structure, initial gas saturation and saturation history, and gas saturation is also dependent on flow patterns [37]. The interaction and coupling of parameters could result in different flow behaviour for identical experiments, and is described as hysteresis.

Residual trapping will reduce the gas recovery for UHS. The main mechanisms for capillary trapping is by-pass and snap-off. Gas can be snapped off from the hydrogen flow when gas is displaced through narrow pore throats if the capillary pressure in the pore space is significantly smaller than the capillary pressure in the pore throat. When the waterfront is moving through the pore network, the gas could either be piston-like displaced by the waterfront, or capillary trapped by by-pass or snap-off [38]. Other trapping mechanisms like solubility- and mineral trapping occur on long term for gas storage and has been observed for CO_2 storage [39]. Dissolution of residual hydrogen has been observed in the literature[40], [41], but in in contrary to permanent storage of CO_2, the long term trapping of gas is not a desired mechanisms for UHS because the residual gas cannot be recovered. The dimensionless capillary number (N_c) is used to describe the relationship between viscous and capillary forces in capillary channels:

$$N_c = \frac{viscous forces}{capillary forces} = \frac{U\mu}{\sigma} \tag{2.4}$$

where U is Darcy flow velocity [m/s], $\mu = 0.001002$ is the water viscosity [Pas] at room temperature and σ is the hydrogen-water IFT [N/m]. The Darcy flow velocity is calculated by:

$$U = \frac{Q}{Ld\phi}$$

where Q is the hydrogen injection rate [ml/h] and L, d and ϕ are the micromodel's length[m], depth[m] and porosity, respectively.

The relationship between the irredusible water saturation and capillary number N_c is given by the capillary desaturation curve (CDC) presented in Figure 2.3. The irredusible water saturation is the lowest water saturation obtained for the capillary number. Capillary forces are dominating for low injection rates during drainage and imbibition[42], and increased viscous forces will give a lower irredusible water saturation due to less residual trapping. A CDC is fundamental in oil and gas recovery to increase recovery efficiency and describes the required flow conditions for oil displacement. The CDC curve could

be modified to describe the storage capacity of UHS, giving the relationship between irredusible water saturation during drainage [40] by capillary number. The N_c with the lowest water saturation will correspond to the highest gas saturation and the highest storage capacity.

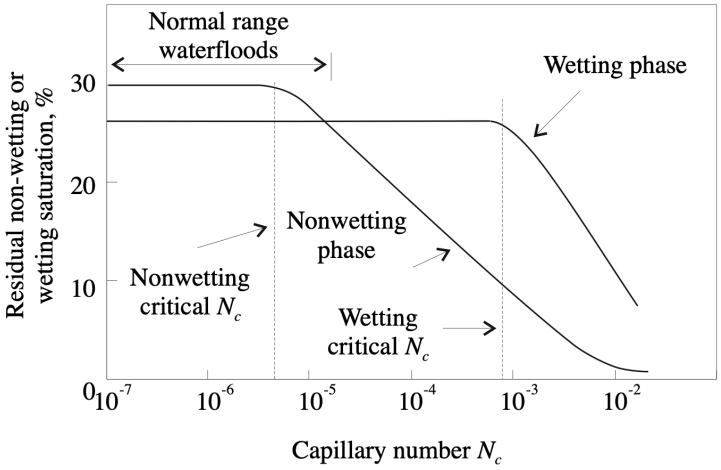

Figure 2.3: Schematic capillary desaturation curve [43].

2.3.4 Literature

UHS is a relatively new concept with few experimental data and scars experience. The following section will give an overview of state-of-art underground hydrogen storage solutions and present relevant published scientific articles on the topic.

Even though the experience of underground hydrogen storage is scarce, several projects for underground hydrogen storage have been initiated the past year. Seven European partners will demonstrate large-scale storage of green hydrogen in salt caverns in the HYPSTER project claiming its the first project of its kind. The HyStorIES project, funded by Horizon 2020 programme, aims to deliver technological developments for hydrogen storage in depleted fields and aquifers, including determination of the expected microbial activity and development strategies for long lasting wells. The Horizon 2020 funded project HyUsPre will research the feasibility and potential of implementing large-scale storage in porous media. The first parts of the delivery are a technical feasibility, risk and potential of large-scale UHS in porous reservoirs in Europe. A roadmap for the deployment of UHS up to 2050 will also be developed. Companies are also testing and proving CCS technologies[44], with broad experience of geological structures from the petroleum industry.

Most papers published in literature studies are modelling UHS behaviour or overviews of large-scale storage solutions. Fieldman et al. [45]have performed a numerical simulation of hydrodynamic and gas mixing processes for UHS in a depleted gas reservoir. Lysyy et al. [46] simulated hydrogen underground storage in a depleted gas field. Lysyy et al. suggested a need for more experimental studies where key parameters were examined. Suggested areas are miscibility with oil, diffusion and dispersion, residual saturations, capillary pressure and relative permeability. Amid et al. [47] modelled hydrogen losses for UHS for a sandstone reservoir at depth 2743m and temperature 365K with hydrogen injection pressure between 5 to 10 MPa during 12 moths. They estimated hydrogen loss

to diffusion from water-filled pores in the caprock ($\phi = 0.05$) and the underlying aquifer($\phi = 0.2$), assuming pure water. Leakage losses were 0.035% of the stored hydrogen after 12 months, where 0.029% was lost to the aquifers and 0.006% to the caprock. The estimates are an upper bound due to the use of pure water, where saline water would have a lower solubility and dissolution. The paper concluded that the reservoir's losses from dissolution and diffusion would be less than 0.1%. They also estimated the biological consumption of hydrogen and found that only 3.7% of the hydrogen would be lost to conversion to methane or biogas over storage lifetime in a worst-case scenario. H_2S can also be produced from microbial reactions in the formation and is not beneficial[47] because H_2S is toxic, corrosive, and can damage fuel cells. Purification of hydrogen can be necessary after extraction due to contaminations in the reservoir. Hydrogen dissolution was also studied by Bo et al [48]. They performed a geochemical modelling to examine hydrogen loss in an UHS with pressure at 0.1 to 101 MPa and temperature in the range of 30 to 200°C. The results of the study showed that an increase in pressure and temperature only increased the hydrogen solubility slightly in brines, and an increased salinity decreased the hydrogen solubility. They also concluded that hydrogen loss caused by geochemical reactions would be minor for UHS [48]. Other studies are more general and presents overview of storage solutions and feasabilities. Amid et.al. [47] has performed a feasibility study of seasonal storage of hydrogen in depleted natural gas reservoir. Papers by Andersson et.al. and Matos et.al. gives overview and criteria for large-scale UHS [49],[26]. Site selection is also a topic in Nemati et al. [50] and Arvantis et al. [51].

Lab scale experiments are also conducted in the study of hydrogen behaviour in underground geological structures. Flesch. et. al. have performed core experiments on reservoir sandstones under simulated reservoir conditions in depleted reservoirs or sedimentary aquifers [31]. Hart [40] and Lysyy et al.[41] studied pore-scale behaviour of hydrogen-water-micromodel system. Hart found that hydrogen saturation increased with capillary number during drainage until a specific water saturation was reached, and that hydrogen dissolution was mainly driven by advection at the water-hydrogen interface. The dissolution was also observed to be correlated with increasing capillary number, where hydrogen solubility was slightly dependent on capillary number and high dependence of micromodel pressure. Lysyy et.al. also observed increased hydrogen saturation after drainage with increasing capillary number. In addition, static and dynamic contact angles were measured in the range from 17 to 56°.

The study of cyclic hydrogen injection and withdrawal is essensial to obtain more realistic conditions for UHS, but are not found in literature. However, literature on cyclic injection of CO_2 exist and can be used as comparison in lack of other studies. Edlemann et.al.(2018) studied cyclic injection of CO_2 and water over 6 cycles at 1ml/min was performed using a high flow rig with in-situ conditions[52] where the experiments were conducted on a core sample of a Fell sandstone with porosity at 20.3%. It was found that fluid mobility was influenced by pore space and geometry, wettability and residual saturation of CO_2 and water. A pressure was also observed for cyclic CO_2 injection where that the differential pressure increased dramatically before it decreased to a lower level, indicating that water was the wetting phase[52]. Cyclic injection of supercritical CO_2 and brine was also studied by Herring et.al.(2016) in Bentheimer sandstone cores. It was observed that the residual CO_2 trapping increased dramatically after the first cycle of injection at same capillary numbers. They also mentions that the magnitude of the residual trapping was hysteretic and would be dependent on the drainage processes. The capillary hysteresis effect was

observed to be limited to the first and second flooding cycle for CO_2-brine flooding during core experiments in studies by Saeedi et al.[36]. Ahn et al. simulated CO_2 injection with experiments using n-hexane and water, where it was observed that the random flow patterns gradually converted to less ramified paths over multiple cycles [8].

Jafari et al. presents a technique for contact angle measurement of CO_2 in a micromodel [39]. Contact angles are often measured on a flat surface, however this is not a suitable approach for fluid flow in porous media. The paper presents a in-situ method at pore-scale to in a micromodel. A wide range of pore-scale contact angles was measured, implying a complexity even on model scale. Wettability is often quantified using contact angles. The paper measured both static and dynamic contact angles, where static angles are measured when the interfaces between water and CO_2 is in no motion and dynamic contact angles are measured in motion. The methods can also be applied for hydrogen. The receding contact angle should be considered when hydrogen is injected. H_2 will push water through the model. Water imbibition will displace H_2 out of the pore channels, but portions of H_2 will be trapped if discontinuity occurs. A wide range of contact angles at pore-scale was observed, despite use of a smooth, homogeneous glass micromodel.

2.3.5 Pore-scale study using micromodels

Micromodel

Lab scale experiments can be useful to study mechanisms and processes occurring on field scale. Microfluidics is the science and technology where small amount of fluids (10^{-9} to 10^{-18} liters) are manipulated using a channeled network [53]. A typical microfluidic system is only a few centimetres and very small quantities of fluids is necessary. Microfluidics is suited for early stage research due to low costs, small experiment footprint and laminar flow. For a multi-phase flow in a microsystem, fluids will flow parallel, and a laminar flow is obtained due to no convectively mixing. Microfluidic systems also offers a small window to observe specific phenomena, investigate mechanisms and behaviour of fluids. A typical microfluidic systems consist of fluids, equipment to move the fluids and devices to collect data for further analysis [53].

A micromodel is an example of a microfluidic system and can be used to study the behaviour of fluids in micro structures such as porous media, where micromodel will be an idealised representation. Micromodels are usually two-dimensional with a constant depth, where the pore network consist of small pores to make sure that the capillary effects will be considerable. They are typically used for displacement of immiscible fluids, and the fluid flow and transport can be studied within the pore space. Examples of processes are drainage, imbibition, viscous or capillary fingering, relative permeability, saturation and snap-off. Fluid interfaces can also be studied using micromodels, but the curvature of the interfaces cannot be determined by video analysis due to the two-dimensional visualisation. In addition, it is not possible to measure the local phase pressure within the network as of today, and micro sensors should be developed [54]. Micromodels can have different geometry and patterns, depending on what structure the micromodel will idealise. Perfect regular patterns, fractal patterns and irregular patterns are examples of patterns and can be generated by computer [54].

Phase distribution and qualitative data can be visualised and extracted using a microscope

and/or digital cameras. Two-phase fluid flow parameters such as interfacial area and saturations can be measured by analysing video material and images. A microscope-camera setup is a simple setup that can monitor in-situ and save video material to the camera and the connected computer. A disadvantage with the setup is that the microscope is focused on a specific area, the Field of View (FoV) of the micromodel, and the processes outside the FoV could not be observed unless the microscope is moved. The system setup has limitations in the study of dynamic effects of the whole system, but an advantage of a narrow FoV is high resolution images.A camera can also be placed at a longer distance from the microscope to observe the entire micromodel, but the images will have a lower resolution which will increase the uncertainty [54].

Porosity and saturation calculations based microscope images

Porosity and gas saturation can be calculated based on the microscope images. A two-dimensional micromodel will be used to study hydrogen fluid behaviour in an aquifer in this thesis. Data were collected from videos and images captured by the camera mounted to the microscope, similar to the described microfluidic system. Porosity is defined as the storage capacity of a porous media and can be calculated based on the microscope images from the FoV of the micromodel. The FoV porosity can be calculated based on thee pixel area of the grains or pore space in the FoV:

$$a)\phi = \frac{1 - A_{grain}}{A_{tot}} \cdot 100\% \tag{2.5}$$

$$\phi = \frac{A_{pores}}{A_{tot}} \cdot 100\% \tag{2.6}$$

where $A_{pores}[px]$ is the the area of the pore space, $A_{grains}[px]$ is the area of the grains, and $A_{tot}[px]$ it the total area of the FoV.

Hydrogen saturation can be calculated by measuring the pixel area of the hydrogen in the microscope images. A water wet micromodel would have thin film of water at the surface, but it is assumed that the pore space is 100% gas saturated. Saturation is defined as the ratio between the volume fluid present V_g and the available pore volume V_p.:

$$S_g = \frac{A_g}{A_t \cdot \phi} \tag{2.7}$$

where $A_g[px]$ area of hydrogen in the FoV, $A_t[px]$ is the total area of the image and ϕ is the FoV porosity.

Chapter 3

Method

This chapter will describe the methods used during the experiments and image processing. The chapter is divided in two sections: experimental setup and image analysis. Direct observations of hydrogen flow behaviours in porous media were enabled by a high-pressure microfluidic setup. During experiments, videos were taken to capture the fluid flow in the micromodel and the raw data was analysed using MATLAB and ImageJ.

3.1 Experimental setup and equipment

Experiments were performed in the hydrate laboratory at the Department of Physics and Technology at the University of Bergen (UiB). Figure 3.2 shows the experimental setup for the hydrogen injection experiments, with the main elements described in detail in sub-chapters below. A total of 15 experiments were performed in this setup with objectives to investigate hydrogen saturation, contact angles and residual gas. Drainage and imbibition processes were investigated in a high pressure micromodel, which offered a small window to study fluid behaviour in the pore structure. The experiments were divided in two parts: Part A and part B. Primary drainage and imbibition were performed in Part A, with objective to continue and complete the previous work performed by a previous Msc. Student and a Phd student with the identical experimental setup [40],[41]. For the cyclic hydrogen injection in part B experiments, a bypass channel was added to the initial setup to perform 4 to 5 cycles of drainage and imbibition. All the experiments were performed at 40 bar and room temperature with different injection rates to investigate the sensitivity to capillary number.

The system contains equipment to inject hydrogen or water into the microsystem for pore-scale investigations of hydrogen flow in porous media at elevated reservoir pressure. A high precision plunger pump (Quizix Q5200 pump) was operated in independent mode and used for H2 injection and withdrawal. The Quizix QX pump was connected to the micromodel by a combination of 1/16" PEEK and 1/8" steel tubing and used for distilled water injection. The system was pressurised by two injection pumps, which one was operated at constant mode to keep the pressure in the system, and the other pump was operated at constant flow rate mode for gas/liquid injection. A camera (Nikon D7100) was mounted to a microscope (Nikon SMZ1500) to observe and record the experimental processes in the micromodel. A concentrated light source was attached to the microscope to illuminate the FoV. The experiments were recorded continuously either with interval

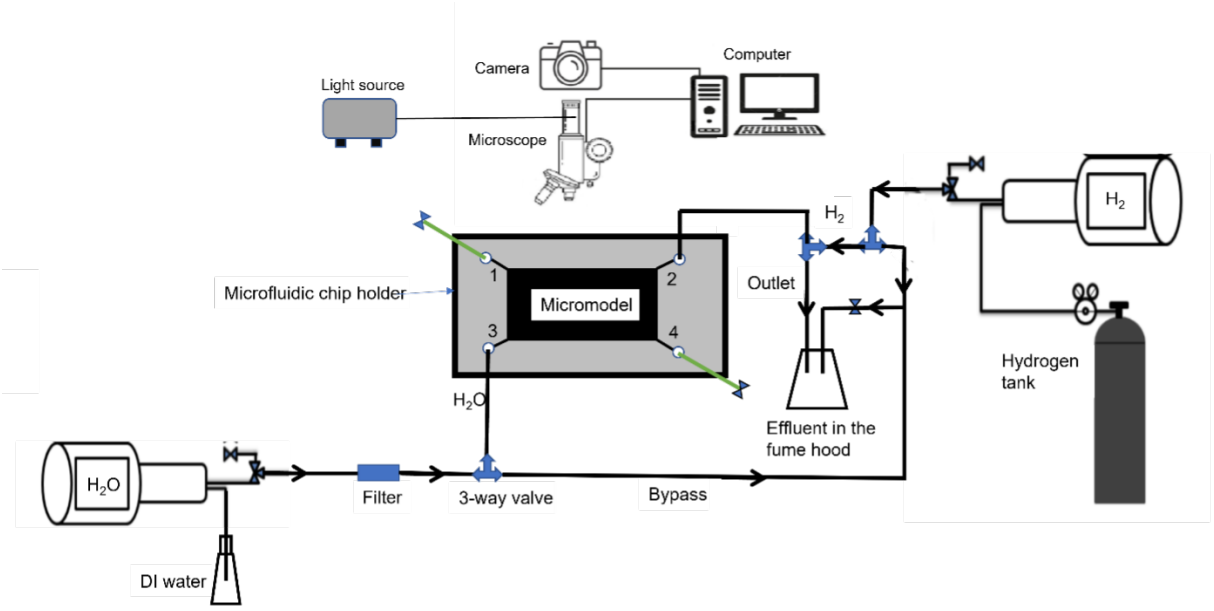

Figure 3.1: Illustration of the experimental setup of this thesis. By post-doc Na Liu, adapted from [55]

.

images or videos, depending on the duration of the experiments. All fluids were filtered through a 0.5µm inline filter assembly (Idex, A-431) prior to entering the micromodel. Prior to every run in cyclic experiments, the water channel and the hydrogen channel were cleaned through the bypass line to remove trapped hydrogen/water from previous runs. Port 1 and port 4 were unused and plugged during experiments.

The equipment and experimental fluids used during experiments:

- High-pressure micromodel
- Quizix Q 5200 pump system for hydrogen gas injection
- Quizix QX pump for water injection
- Stainless-steel casing
- 1/16" PEEK (Polyether Ether Ketone) and 1/8" steel tubing
- Nikon SMZ1500 microscope Nikon D7100 camera
- Photonic LED F1 Cold Light 5500K light source
- Computer
- Hydrogen gas from Nippon gases
- Distilled water (DI water)

3.1.1 Micromodel

The pore network of micromodel used in this thesis is designed based on a natural sandstone with a large variation in grain and pore sizes and shapes, which is shown in Figure 3.2 with the properties given in Table 3.1. A pattern (6.74 x 2.50 mm) was extracted

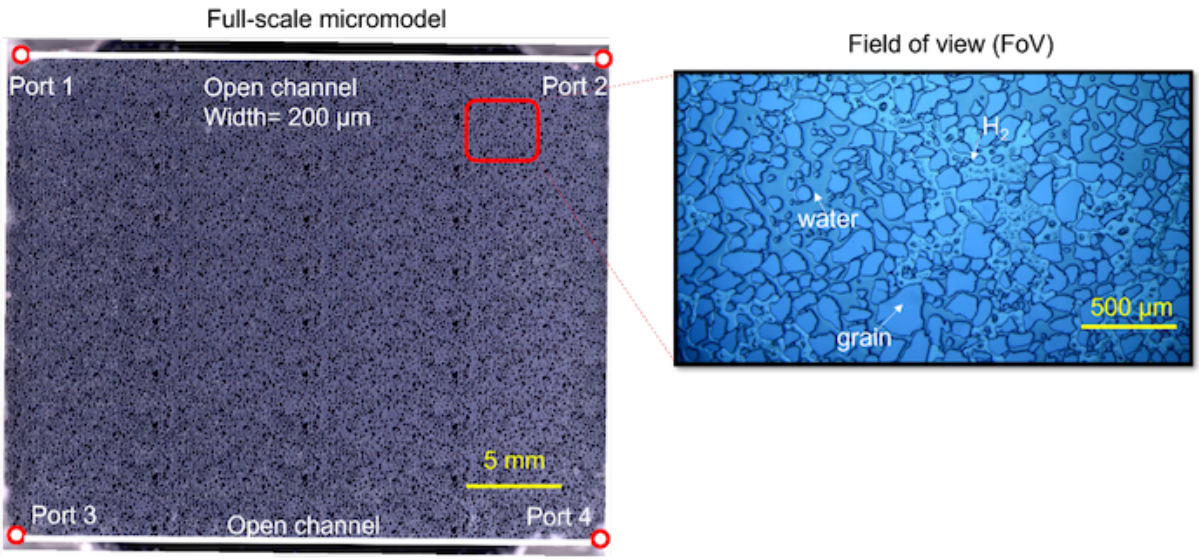

Figure 3.2: Full-scale image of micromodel including dimensions, highlights of four flow-ports and the two open-channel fractures between two pairs of ports. The FoV is highlighted in red.By post-doc Na Liu, adapted from [55]

from thin sections of the natural sandstone, which was repeated 36 times to create the micromodel porous network. The full-scale pore network has the dimensions of 2.7 cm x 2.2 cm x 30 µm in length x width x depth, respectively. The average porosity is 0.61 for the entire micromodel. There are 4 ports in 4 corners to connect the micromodel with external fluid flow tubes, and two open channels between ports to allow evenly distribution the injected fluids.

The FoV of the microscope only displayed approximately 1% of the micromodel[41], which has the dimensions of 3.5 mm x 1.8 mm in length x width, respectively. The porosity of FoV was quantified to 0.44 at average based on the available pore space relative to the total area, and the pore volume of FoV was 0.088 µL. Average grain size of FoV is calculated to 3374 μm^2 and average pore throat length is 41 µm, with the shortest pore throat being 0.7 µm with square or rectangular cross-section.

Table 3.1: Properties of the micromodel used in the experiments.

Parameters	**Full-scale micromodel**	**FoV**
Effective Porosity	$\sim$ 0.61	$\sim$ 0.44%
Absolute permeability	2.97D	
Dimensions (Width/Length/Depth)	2.2 cm/ 2.8 cm /30μm	3.5mm/1.8mm/30µm
Pore volume	0.011 mL	0.088µL
Wettability	strongly water wet	strongly water wet
Repetition of pattern	36	1
Grain size	0.5-78366µm	0.5-78366µm
Pressure range	0-150 bar	0-150 bar

3.2 Experimental procedures

3.2.1 Part A - primary drainage and imbibition

A total of four experiments of primary drainage and imbibition were performed at different capillary numbers at 40 bar and room temperature, where pressure and injected volumes were recorded during experiments. The experimental conditions are shown in Table 3.2. The following procedure was performed for four experiments:

1. The micromodel was cleaned by water from port 3 to 4 to remove the residual hydrogen from previous experiments. The outlet valve in port 4 was open with tubing exiting in a sink inside a fume hood.

2. After cleaning, the micromodel was pressurised by the water pump by injection of water from port 3 to 2. The Quizix QX pump was operated at the constant flow rate mode to increase the system pressure step by step until reaching to 40 bar.

3. The Quizix Q5200 pump was refilled with hydrogen gas at 40 bar. The pressure in both pumps should be equal to ensure that there was no pressure gradient between port 2 and port 3 when the hydrogen valve was opened.

4. The desired FoV was adjusted at the microscope. It was attempted to use the same FoV was used for all experiments.

5. Primary drainage - injection of H_2: The water pump was set to retract mode at constant rate to draw hydrogen out of the gas cylinder[1]. The hydrogen pump was set to constant pressure to maintain the pressure. 100 pore volumes (PV) were injected after hydrogen was observed in the FoV.

6. Imbibition - injection of water: After drainage, water was injected at constant rate into the micromodel until the hydrogen was swept out or dissolved from the FoV. The hydrogen pump was at constant pressure.

7. After the experiment, hydrogen was injected to the model to ensure that there was no water left in the hydrogen tubing. The hydrogen valve was then closed and step 1 was repeated.

Table 3.2: Experimental conditions in Part A.

Experimental conditions	**Flowrate,** Q [mL/h] ±0.2%	**Flow velocity,** $U[m/s] \pm 0.2\%$	**Capillary number,** N_c ±0.2%
P = 40 bar	0.1	$5.51 \cdot 10^{-5}$	$7.59 \cdot 10^{-7}$
T = 22°C	1	$5.51 \cdot 10^{-4}$	$7.59 \cdot 10^{-6}$
	10	$5.51 \cdot 10^{-3}$	$7.59 \cdot 10^{-4}$
	50	$2.76 \cdot 10^{-2}$	$3.80 \cdot 10^{-4}$

[1]Based on experience from PhD student and former master student. Due to the compressibility of hydrogen, previous work stated that it was challenging to inject hydrogen into the model at a suitable time period. In order to perform the hydrogen drainage, water was retracted at the same time that the hydrogen injection occurred.

3.2.2 Part B - cyclic injection

Four different flow rates were applied for cyclic injection: 1, 2.5, 5 and 10 mL/h, with corresponding flow velocity (U) and capillary numbers (N_c) shown in Table 3.3.

Three experiments were performed at 10 ml/h (40 bar) to standardise the procedure for cyclic injection. A test experiment C1 was performed by following the procedure from Part A, where step 5 and 6 was repeated for a total of 5 cycles. Filtered distilled water was used instead of distilled water. The analysis showed that 100PV injected was not necessary to reach the end-point saturation. 100PV would also probability lead to water in the gas pump and vica verca. A second test experiment C2 was performed with small changes from the the first experiment. A filter was installed at the water inlet to ensure that no dust or particles entered the micromodel and disturbed the mechanisms and processes in the model. The outlet in port 4 was moved to a dual valve in port 2, were the diagonally flow from port 3 to 2 would increase flushing performance after the experiments. At drainage in step 5, the hydrogen pump was set to constant rate and the water pump was at constant pressure mode. 20 PV was injected after hydrogen was observed in the FoV. Otherwise, the procedure was the same.

The test experiments C1 and C2 showed that the constant pressure mode at the pump was insensitive to the given pressure value. Previous work recommended not to use constant rate for gas injection [40]. To obtain a more realistic procedure, a constant rate was attempted during drainage in a test experiment C3 without problems. The disadvantage with constant pressure mode is that the actual hydrogen injected rate would be alternating to regulate the pressure. The use of constant pressure could cause a wrong impression of injection rate and capillary number, given that the rate is fluctuating. Figure 5.3 shows a typical behaviour of primary drainage at constant rate for the water pump and constant pressure mode for the hydrogen pump.

A by-pass line was added to the setup after the test experiments. Gas was retracted into the water tubing during drainage, and water was retracted into the gas tubing during imbibition for C1-C3. As a consequence, a two-phase displacement would occur in the first time period of drainage and imbibition because both fluids was present in the tubing. This could affect the gas distribution and made it difficult to determine the entry of the water and hydrogen fronts and not just redistributions of fluids. Water and gas could be injected into the by-pass to ensure a uniform flow of water and gas in the tubing, respectively.

Table 3.3: Experimental conditions in Part B.

Experimental conditions	**Flowrate**, Q [mL/h] ±0.2%	**Flow velocity**, $U[m/s] \pm 0.2\%$	**Capillary number**, N_c ±0.2%
T = 22°C	1	$5.51 \cdot 10^{-4}$	$7.59 \cdot 10^{-6}$
	2.5	$1.38 \cdot 10^{-3}$	$1.90 \cdot 10^{-5}$
	5	$2.76 \cdot 10^{-3}$	$3.80 \cdot 10^{-5}$
	10	$5.51 \cdot 10^{-3}$	$7.59 \cdot 10^{-4}$

The procedure for cyclic injection during experiments in Part B:

1. Water was flushed through the system to ensure that no residual hydrogen was in the system. The outlet valve in port 4 was open with tubing exiting in a sink inside a fume hood. The water was pumped from the Quizix QX pump through port 3 to the micromodel. The micromodel was pressurised to 40 bar by closing port 2, and the micromodel was fully saturated with water. Two pumps were connected to balance the pressure in both sides of micromodel before primary drainage.

2. Drainage - Injection of H_2: The water pump was set to constant pressure mode while hydrogen was injected at constant rate. 20-30PV of hydrogen was injected into the micromodel after hydrogen was observed in the FoV, expect for the first cycle where gas was injected until it was certain that the maximum saturation was reached ($\sim$50 PV). Before imbibition, water was injected to the by-pass to displace the gas phase in the tubing.

   2b. Subsequently, water pump was pressurised to the desired pressure through bypass line.

3. Imbibition - injection of water: Both pumps were operated on constant rate mode[2]. The imbibition was stopped when gas was disconnected. The Quizix QX pump was operated at extend mode with constant flow rate to inject water to the micromodel, while the Quizix Q5200 pump worked at retract mode with the same flow rate as the water pump to maintain the system pressure.

   3b. Prior to the next cycle, gas was injected into the bypass to flush the residual water in the gas tubing. The valve was closed and the bypass outlet was opened exiting in the fume hood. The procedure was repeated twice to avoid too high pressure in the bypass.

   3c. The bypass outlet was closed and the pressure was adjusted to the desired pressure.

4. For each cycle, step 6 and 7 was repeated. A total of 4-5 cycles were performed.

5. After the experiment, the micromodel was depressurised and step 1 was repeated.

Cleaning of micromodel

Black spots and small movements were observed in the micromodel during water injection during the first experiments. To reduce the potential influence on mechanisms and processes, the micromodel was cleaned after the experiments in Part A. A syringe was used to inject the fluids diagonally from port 1 to outlet in port 4. The micromodel was cleaned in cooperation with post-doc Na Liu. Procedure for cleaning:

1. Injection of filtered DI water.

2. Injection of isopropanol.

3. Injection of filtered DI water.

4. Injection of H_2O_2 to make sure the conditions of the surface did not change.

[2]The imbibitions in experiment B5-1 and B8-1 followed the same procedure as in Part A, with constant rate for water pump and constant pressure for the hydrogen pump.

5. Injection of filtered DI water.
6. The micromodel was then flushed with DI water to make sure that the micromodel was 100% water saturated.

3.3 Image analysis

This part describes the essential image analysis tools created during this master thesis and the scripts can be found in Appendix A.

3.3.1 Data collection

Data were collected from videos and images captured by the camera mounted to the microscope. The right image in Figure 3.2 shows a typical microscopic view of the pore network saturated with hydrogen and distilled water. An image extracted from a video had a display resolution of 1920 x 1080 pixels, resulting in a total area of 2073600 pixels. The snapshot photos had a resolution of 4096 x 2296 pixels, a total of 9404416 pixels. The object detection in the images was determined by image processing tools from ImageJ and MATLAB based on colour differences.

3.3.2 Image analysis by ImageJ

The open-source software ImageJ was used for image analysis in previous work [40]. The ImageJ tool "colour threshold" was used to identify and distinguish hydrogen from water and grains. A point light source was used during experiments with highest concentration in the centre of the FoV, resulting in an uneven illumination causing difficulties in the image processing. Figure 3.3 shows a typical background image with enhanced contrast to the maximum to better observe the light distribution in the FoV. All elements in the micromodel was in the same colour region, and ImageJ struggled to distinguish the difference between the elements present. Previous work emphasised the challenge and uncertainties using ImageJ caused by the similarity in colour and the uneven light distribution. The problem was addressed by manually colouring the hydrogen in a new colour using Paint-3D, and ImageJ could measure the area of the coloured pixels. With a high number of videos and images, the image processing was time-consuming. Another disadvantage with ImageJ is that every image had to be selected manually regardless of the luminosity of the image and colour differences.

ImageJ was used in combination with manual colouring for local porosity calculation and uncertainty measurements. The iPad iOS application ibisPaint (Version.9.3.0) with an Apple pencil was used for colouring the hydrogen to increase porosity precision. The original background was overlapped by a segmented image of the background. A copy of the background image was processed in ImageJ to increase colouring precision where the efficiency of the bucket tool function increased by using a segmented image processed in ImageJ. The segmented image was created by using the "find maxima" function under the process tab with prominence >20.00 and selecting "segmented particles" as the output type. The segmented image with black background and white lines was inverted by Image>Adjust threshold. The segmentation was not accurate for all grains, and some grains had to be coloured manually using the original image. An example of the different layers is shown in Figure 3.4.

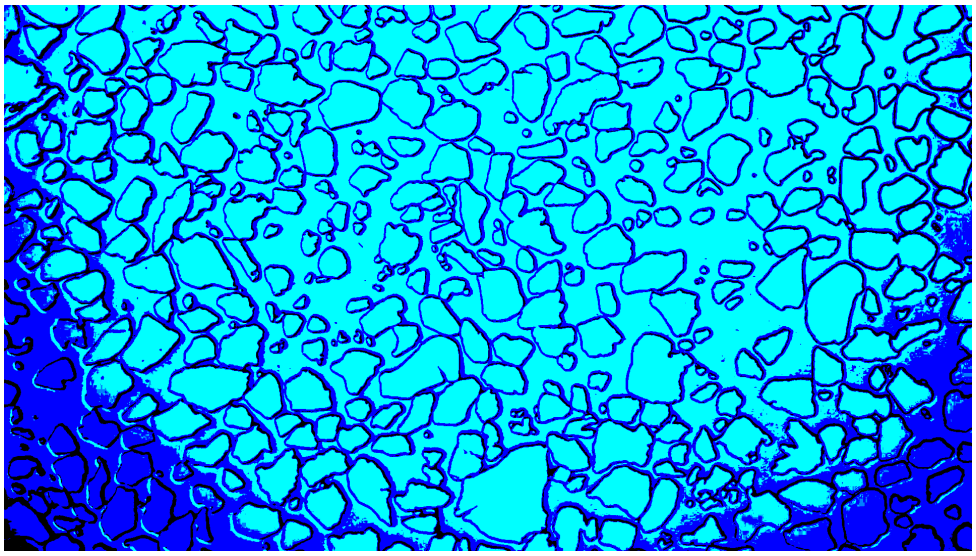

Figure 3.3: FoV colour contrast. Example of background image in the FoV with enhanced contrast to the maximum.

Procedure:

1. Original image was added in the first layer.
2. The original image was processed using ImageJ and the segmented image was added as a new layer.
3. Bucket tool was adjusted to 15% strength with an expansion of 1.0 and used to colour the grains, including the segmented image lines.
4. Background colour was added in a separate layer and placed under the coloured layer.

3.3.3 Image analysis by MATLAB

A new method for gas detection was developed in MATLAB to optimise the image processing, increase the quality of the obtained data. The video material was converted to image sequences with intervals of 1 frame per second, and the first image with 100% water saturation was chosen as a background image. The background image was subtracted from the original microscope images in the image segmentation algorithm, producing a filtered binary image (filtered image). The image segmentation algorithm was developed in cooperation with Post-doc Na Liu. The algorithm calculated the hydrogen saturations of the filtered images, and the saturation data was saved to an excel file enabling further analysis. The MATLAB scripts are attached in Appendix A.

The overall procedure for image analysis: /vurder om det evt skal vÃ¦re i appendix.

1. A video-to-image script saved the images in a designated folder, and the images were sorted with the same name as the second it was extracted. For instance, image 0001.jpg was captured in the first second of the video. The images were extracted at a frequency of 1 image per second.
2. Choosing best-suited background image. It was important to have the same position for the background and the image sequences to remove the grains and pores with

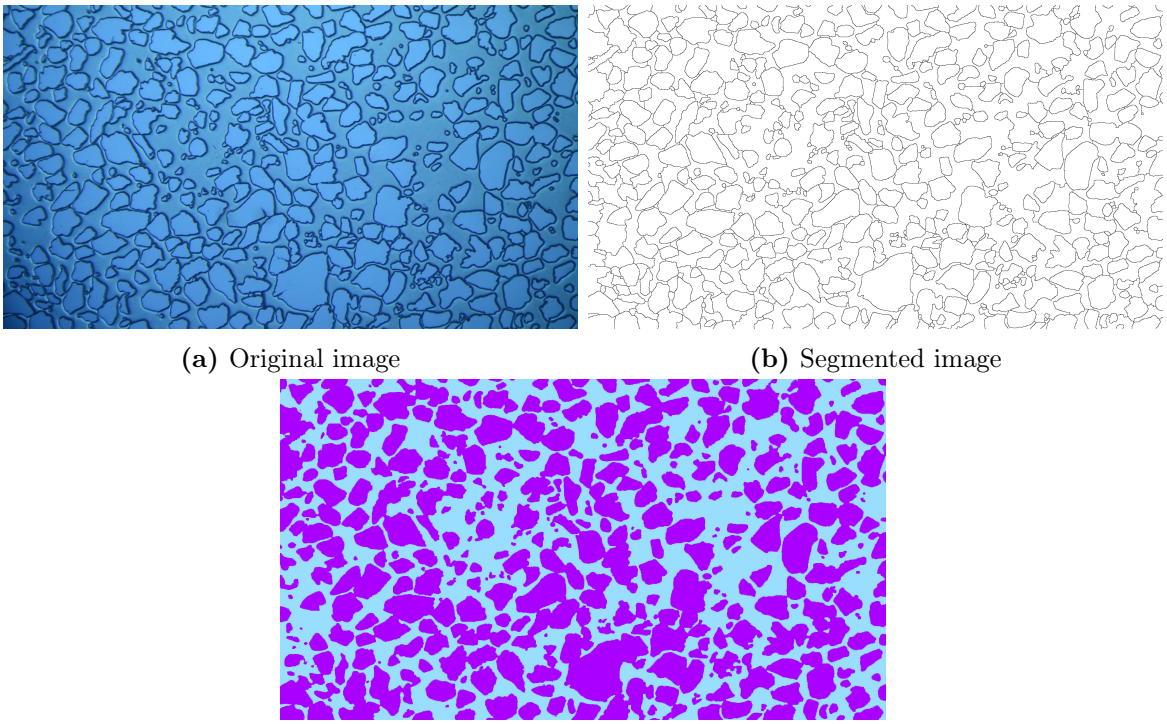

(a) Original image **(b)** Segmented image

(c) Coloured image

Figure 3.4: The image processing method by colouring the grain area with different layers for local porosity measurments($\sim 44\%$). a) Original image b) Segmented image c) Colouring of grains in a separate layer.

water from the image. Ideally, the the first image from the first video could be used as the background image.

3. The background image was converted to grayscale.

4. A for-loop went through the folder with the original images and ran the function for image segmentation.

   4b. The original image was converted to a grayscale.

   4c. The background was subtracted from the original image. The noise was removed using the function bwareopen, and the water holes were closed using imclose, and smaller holes were filled using imfill.

   4d. The function also calculated the saturation by counting the number of white pixels in the binary image. The pixels were used in saturation calculations by Formula 2.7.

   4e. The saturation and the filtered image were returned to the main script.

5. The filtered images were saved in a separate folder.

6. The saturations were saved in a list and saved to an excel file that enabled further analysis.

Small vibrations and movements of the micromodel could affect the image segmentation results. If the FoV position was not identical during the experiments, the segmentation function would return images with too much noise and error to rely on the results. In

some cases, a background image was manually manipulated due to movements of the microscope during the experiment. A background image was created by combining a saturated image with the desired FoV and the background image of the first video (100% water-saturated). The images were imported into different layers in ibisPaint. The background image's position was adjusted to match the grains in the saturated image. If gas was observed in the new background image, the hydrogen was manipulated using a colour eyedropper, pencil, smudge and blur to match the original background of that image. An additional version of the segmentation function was created for experiments with more vibrations and movements in the videos during the experiments to reduce noise in the filtered images.

3.3.4 Contact angle measurements

Static contact angles were measured for the different experiments using the angle tool in ImageJ. Each angle and corresponding pore channel diameter were measured 5 times and the average was calculated. A total of 5 measuring points were chosen for drainage and imbibition. Not all angles were possible to measure due to high uncertainties caused by pore structure, grain roughness and image resolution. The contact point of the interfaces could also be challenging to determine due to thickness of the grain lines and grain-gas interfaces. The uncertainties were calculated using standard deviation. The formulas for uncertainties is in Appendix B. Lysyy et al. [41] measured static contact angles while gas was flowing. They indicated that their similarities between receding contact angles and static contact angles for drainage could be linked to the experimental procedure. The procedure was updated, and the static contact angles were measured when no fluids were injected.

Chapter 4

Method sensitivity

A sensitivity analysis was performed to investigate the uncertainties in the image segmentation algorithm presented in chapter 3 Method. Systematic uncertainties was calculated to increase reliability in the results, and a selection of images was analysed to examine the sensitivity for different hydrogen saturations and independent experiments. The sensitivity analysis showed that the image segmentation algorithm had on average a relative uncertainty at 12%.

4.1 Uncertainty from water accumulation and grains

The filtered images were compared with original microscope images to study the accuracy of the image segmentation algorithm. Figure 4.1 shows an example of a filtered image combined with the original image during drainage and imbibition to illustrate the accuracy of the image segmentation algorithm. Both Figure 4.1(a) and 4.1(b) shows that the most of the hydrogen present in the original image is also present in the filtered image. However, some grains is ignored and hydrogen is missed in some locations. A close-up of the figure is presented in Figure 4.2. The image segmentation algorithm may be tuned to separate grains from gas, or water accumulations (in form of droplets) and gas. It was not possible to separate grains, gas and water accumulations using a single set of parameters. Hence, the chosen parameters reflect a compromise between including a majority of grains and water accumulations. If more of the grains would be removed, most of the water accumulations would be removed as well. Uncertainties of saturation measurements came from the noise threshold during image segmentation to close the water accumulations and exclude some small grains in the gas area, as observed in Figure 4.2. The water accumulation volume was difficult to quantify and were assumed to be gas during image analysis. Hence, the water accumulation was not removed by the segmentation algorithm. Removal of water accumulation could be observed even though the algorithm should not removed the water accumulation from the filtered image. Figure 4.2 shows that the segmentation occasionally ignored grains surrounded by gas, but at the same time hydrogen was missed in another location. Area of ignored gas and covered grains were assumed to be the same, supported by the qualitative sensitivity analysis performed later in this chapter.

The dimensional aspects of a multiphase flow was not accounted for during the image analysis. Hydrogen saturation was calculated by pixel area of the gas by Formula 2.7

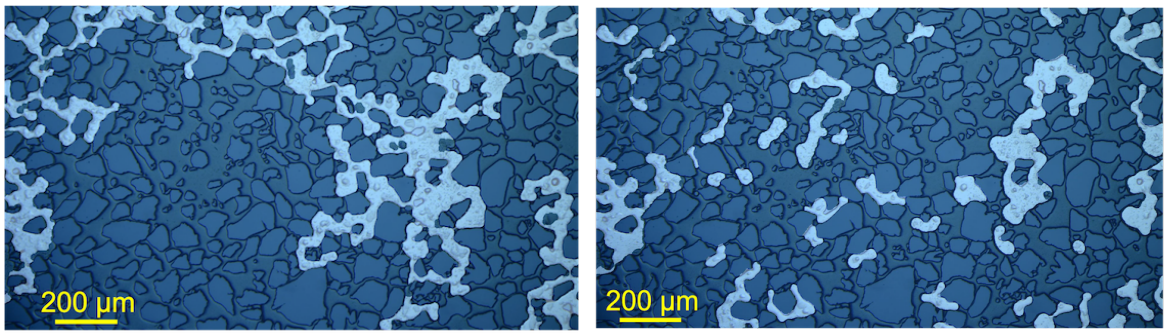

(a) Primary drainage, $S_g = 0.42 \pm 0.05$ **(b)** Primary imbibition, $S_g = 0.31 \pm 0.04$

Figure 4.1: Image segmentation. Example of an original image overlaid by the transparent filtered image for different saturations. a) Primary drainage, b) Primary imbibition

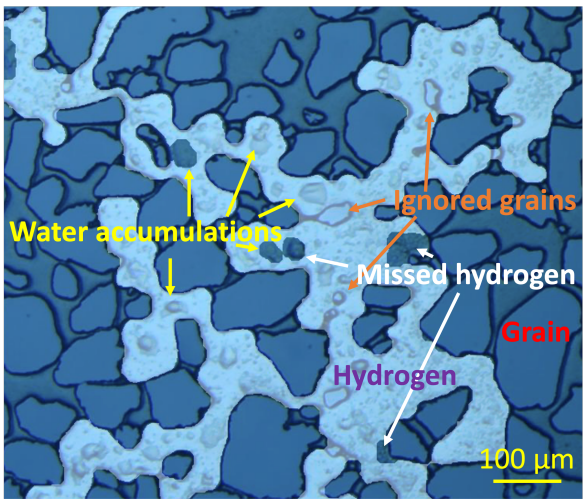

Figure 4.2: Image segmentation close-up. Overview of typical observations in the FoV when the filtered image and the original image are combined. Examples of water accumulation, hydrogen, grains and ignored areas are labelled.

under the assumption that the micromodel was two-dimensional and 100% gas saturated in the gas filled pores. A thin water film would also be present at the surface due to the water-wet behaviour of the micromodel, and the assumption of 100% gas saturation in the gas filled pores resulted in an overestimate of gas saturation. Figure 4.3(a) illustrates the assumed fluid distribution when gas is present in the pores, while Figure 4.3(b) is schematic illustration of the hypothesis of water accumulations and thin water films in hydrogen filled pores. The water accumulation was caused by both surface roughness and the depth of the micromodel and presents a systematic uncertainty of the method. The micromodel bottom and edges were not smooth because of the microfabrication.

Water accumulation is present during both drainage and imbibition. Water accumulation decrease with increased PV hydrogen injected for steady- state flow during drainage, where a higher amount of water accumulation was observed if gas was displacement several times in the FoV during drainage period. The water accumulation was present during imbibition and was mostly constant when gas was disconnected in smaller hydrogen bubbles, but an increase was occasionally observed in larger gas clusters. Only small changes in water accumulation were observed for hydrogen injection below 50PV, but a larger decrease was observed when 100PV hydrogen was injected after gas entry in the FoV. Figure 4.4 shows

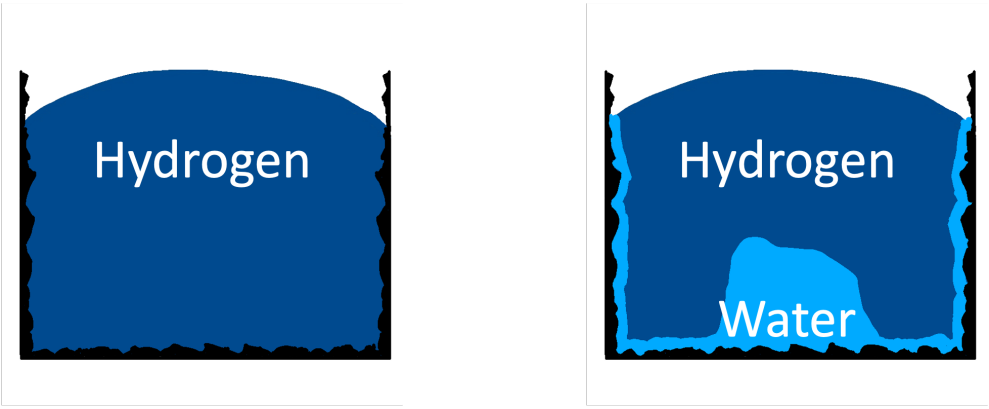

(a) Assumed fluid distribution **(b)** Fluid distribution with water accumulation

Figure 4.3: Fluid assumption in pores. Illustration of assumed and actual fluid distribution where water accumulation is present.

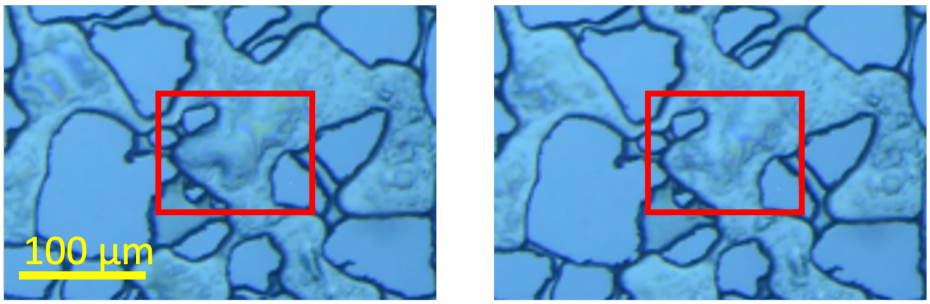

Figure 4.4: Reduction in water accumulation with increasing PV. Water accumulation was decreased in size during 13 PV gas injection at $N_c = 3.80 \cdot 10^{-4}$.

the reduction in water accumulation at high capillary number when 13 PV was injected. Nevertheless, water accumulation was still observed after 100 PV of gas injection.

The hydrogen saturation was observed to increase slightly between drainage and imbibition for some of the experiments. A small gas expansion was observed for some experiments when both water and gas pressure stabilised to equilibrium in the micromodel after the gas injection was stopped during drainage. The water accumulation was also observed to decrease after drainage when no gas was injected, which would result in a higher imbibition H_2 saturation at the start of imbibition due to less water accumulation. The assumption of no water accumulation in the gas flow was a better match for drainage processes when 50 PV to 100 PV was injected, and occasionally at the beginning of imbibition before gas is displaced in the FoV. No clear relationship between water accumulation and capillary number was observed.

Relative uncertainties were calculated based on a selection of filtered images from different experiments. The uncertainties will be descried as the uncertainty u(x) and relative uncertainty $u_R(x)$ for the parameter x. The formulas for uncertainty calculations is given in Appendix B. The relative uncertainty $u_R(S_g(filter))$ of the saturation based on image segmentation algorithm, $S_g(filter)$, was calculated to $u_R(S_g(filter)) = 0.4\%$ for $S_g(filter) > 0.3$ and $u_R(S_g(filter) = 0.3\%$ for $S_g(filter) <= 0.3$ by standard deviation of sequential images after drainage or imbibition was stopped. A filtered image was manually adjusted 3 times to evaluate the systematic uncertainty of the manually mapping

of hydrogen, resulting in a colouring relative uncertainty at $S_g(colouring) = 0.2\%$. An overview of the uncertainties is found in Table 4.1.Figure 4.5 shows the relative uncertainties in relation to hydrogen saturation (Figure 4.5(a)) and capillary number (Figure 4.5(b)). 76 % of the data had relative uncertainties between 2 to 12%, while the remaining percentage included 3 outliers with relative uncertainty of 31, 31 and 32%. One measurement was slightly higher than the majority of measurements, at 17 %rel. No clear trend was observed for neither saturation or capillary number, but it was observed that most of the measurements was concentrated below 12 % relative uncertainty. For simplicity, the total relative uncertainty was assumed to be $u_R(total) = 12\%$ for all experiments, except for experiment (exp.) A3, A4 and B8-2 where the specified uncertainties will be used.

Table 4.1: Uncertainties of the image segmentation algorithm for different saturations and capillary numbers. $u_R(filter)$: relative filter uncertainty.$u_R(total)$: The assumed total relative uncertainty for each measurement(assumed for most experiments).

Uncertainties					
		$u_R(S_g filter) > 0.3$	$u_R(S_g filter) <= 0.3$	$u_R(colouring)$	Assumed $u_R(total)$
Uncertainty(%rel)		0.010%	0.08 %	0.04 %	12 %
Drainage					
Exp.#	$N_c \pm 0.02\%$	S_g filter	S_g colouring	S_g colouring - S_g filter	$u_R(S_g$ filter)
A2	7.59E-06	0.13	0.13	0.002	2 %
B5-1	7.59E-06	0.20	0.197	-0.006	2 %
B5-2	7.59E-06	0.15	0.1581	0.009	6 %
B6-1	3.80E-05	0.562	0.589	0.027	5 %
B6-2	3.80E-05	0.443	0.444	0.001	9 %
B7-1	1.90E-05	0.453	0.470	0.017	4 %
B8-1	7.59E-05	0.424	0.442	0.019	4 %
B8-2	7.59E-05	0.500	0.567	0.096	12 %
A4	3.80E-04	0.492	0.596	0.0104	17 %
Imbibition					
B5-1	7.59E-06	0.023	0.02300	-0.006	2 %
B5-2	7.59E-06	0.024	0.0358	0.029	31 %
B6-1	3.80E-05	0.22	0.02486	0.029	11 %
B6-2	3.80E-05	0.298	0.0307	0.009	3 %
B6-2	3.80E-05	0.358	0.0395	0.037	9 %
B7-1	1.90E-05	0.28	0.0316	0.037	12 %
B8-1	7.59E-05	0.316	0.0337	0.021	6 %
B8-2	7.59E-05	0.21	0.0304	0.096	31 %
A2 A4	3.80E-04	0.199	0.0295	0.096	32 %

4.2 Uncertainty of colour changes

The image analysis utilise the colour difference between hydrogen and a background image with 100% water saturation. Generally, the image segmentation algorithm subtracts the background image from the original microscopic image that is analysed. Hydrogen, water and grains reflect different colour due to different refraction indices, and if the pixels value were equal, the numeric value would return 0 and a black pixel would be displayed in the filtered image. The colour dependency was a limitation of the image segmentation algorithm where concavities in the gas-water interfaces and small water accumulations would be missed due to the colour similarity with the background image. Figure 4.6 shows an example of unsatisfying filtering caused by darker areas in the gas flow. The large area with darker colour was caused by smaller but dense water accumulations in the hydrogen flow. Generally, by Table 8.5, the relative uncertainty was lower than 12%

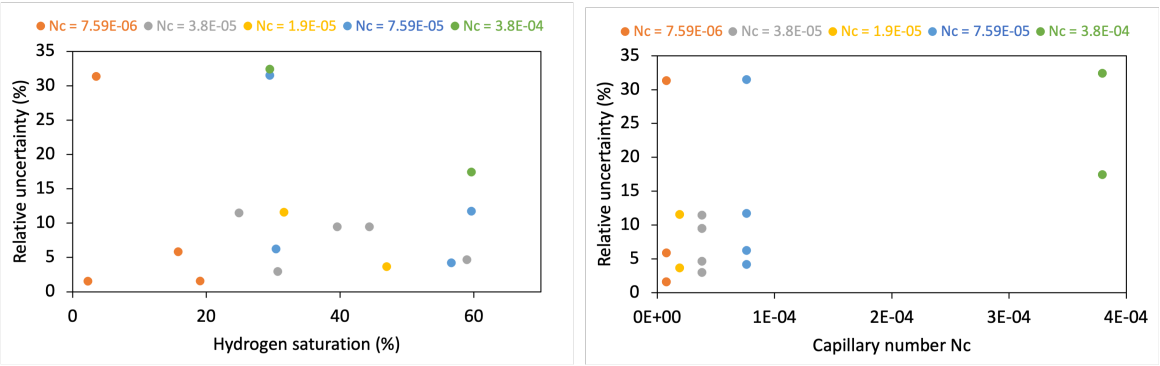

(a) Relative uncertainty vs saturation **(b)** Relative uncertainty vs N_c

Figure 4.5: Uncertainty analysis. a) Relationship between relative uncertainty(%) and hydrogen saturation(%). Most data points are below 12%. b) Relationship between relative uncertainty(%) and N_c. No clear trend was observed.

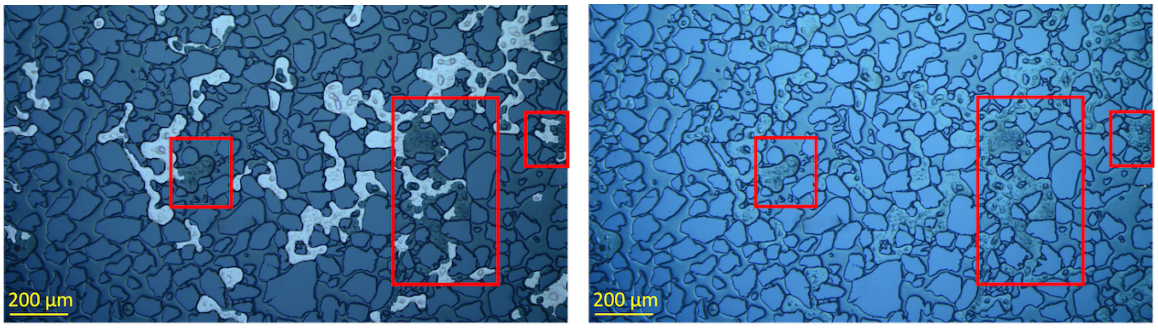

(a) Filtered image, $S_g filter \approx 0.25$ **(b)** Original image, $S_g colouring \approx 0.4$

Figure 4.6: Colour dependency. Darker areas in the gas results in high uncertainty saturation using the image segmentation algorithm for experiment B6-2, resulting in a relative uncertainty of 38%.

for most experiments, however relative uncertainties up to 32% was observed in specific experiments. The wide range of uncertainties for capillary numbers $7.59 \cdot 10^{-6}, 7.59 \cdot 10^{-5}$ and $3.8 \cdot 10^{-4}$ in Figure 4.5(b) was caused by a larger share of darker gas colour during the experiments.

Experiments have shown that the luminosity affected the colours in the original images and can also explain the differences between sequential videos or images. It has been observed that typical deviations occur in the same locations for different experiments. Small pore throats and pore space near the edges were excluded in the filtered images, a result of the light distribution with highest intensity in the centre, Figure 3.3 showed an example of the FoV with maximum contrast, emphasising the luminosity difference in the FoV. The left and right edges was considerably darker than the centre of the FoV, with the darkest locations at the bottom of each side. The darker areas in Figure 3.3 were also the areas where difficulties occurred using ImageJ in previous work [40].An uniform light distribution is expected to increase the accuracy of the segmentation function. Unintended movements of the microscope have also affected the processing accuracy. A tiny change, as small as 50µm, in FoV caused noise in the segmentation due to a difference between the background image and the current FoV. If the change was only temporary (vibrations or returned to the original position), the data point could be ignored. If the movements

were permanent, a new background image had to be used and/or a new noise threshold had to be used to adjusted for noise. The choice of method depended on the amount of noise in the image.

It was also observed that sequential hydrogen saturations fluctuated even though the saturation was observed to be constant in the microscope videos. Light source flicker or other parameters that could not be distinguished visually could have caused the saturation fluctuation between sequential images. The image segmentation algorithm was used to an image sequence of 100 duplicates to excluded the filtering process itself as a source of uncertainty. Zero uncertainty was observed, as expected. The uncertainty of a constant saturation for an image sequence will be referred to as "filter uncertainty" and was generally low compared to the relative uncertainty calculated from a manually coloured image.

4.3 Saturation fluctuations caused by change in FoV

The sensitivity of the image segmentation algorithm caused change in saturation for exp. A1-A3 during the experimental period. Figure 4.7 shows the saturation development for exp. A2. The fluctuations observed was not caused by gas displacements through the FoV. The spikes observed at $\sim$ 7 PV was caused by temporary movements of the microscope where noise was produced in the filtered images. The saturation was observed to be zero until local gas displacement was observed at 16PV. The stepwise change in saturation the saturation was caused by the effect of saturation change for sequential videos, in combination with microscope movements, where the amount of noise varied both within a video and between videos. A new background image had to be produced during drainage at t = 50 PV due to a change in the FoV at 100µm. More gas was observed at the left edge in the initial FoV compared to the new position where the FoV was moved to the right. The shift in position resulted in an overall increase in saturation. Note that the gas distribution did not change, the FoV did, and illustrates the sensitivity of small movements of the microscope. Change in FoV was also observed during A2 imbibition at the time t = 140 PV which caused the sudden saturation increase where new background images had to be produced for the rest of the video material due to a slightly changed FoV. A constant saturation between t = 140 PV and 280 PV was supported by video material. These effects are largest for low capillary numbers due to the long injection periods with several videos during both drainage and imbibition where the microscope are moved during the experiments. Small changes in the FoV changed the saturation or increased noise if a new background images had to be produced. A similar behaviour due to movement of the microscope during the experiments was observed for exp.A1 and A4. Less noise was observed during exp.A3, but an underestimate of gas was observed, caused by unfocused images and water accumulations in the gas flow. The end-point gas saturations for exp. A1-A4 was mapped manually by colouring due to high uncertainties caused by movements of the microscope during the experiments. The uncertainty varied between videos and the hydrogen saturation uncertainty did not vary systematically.

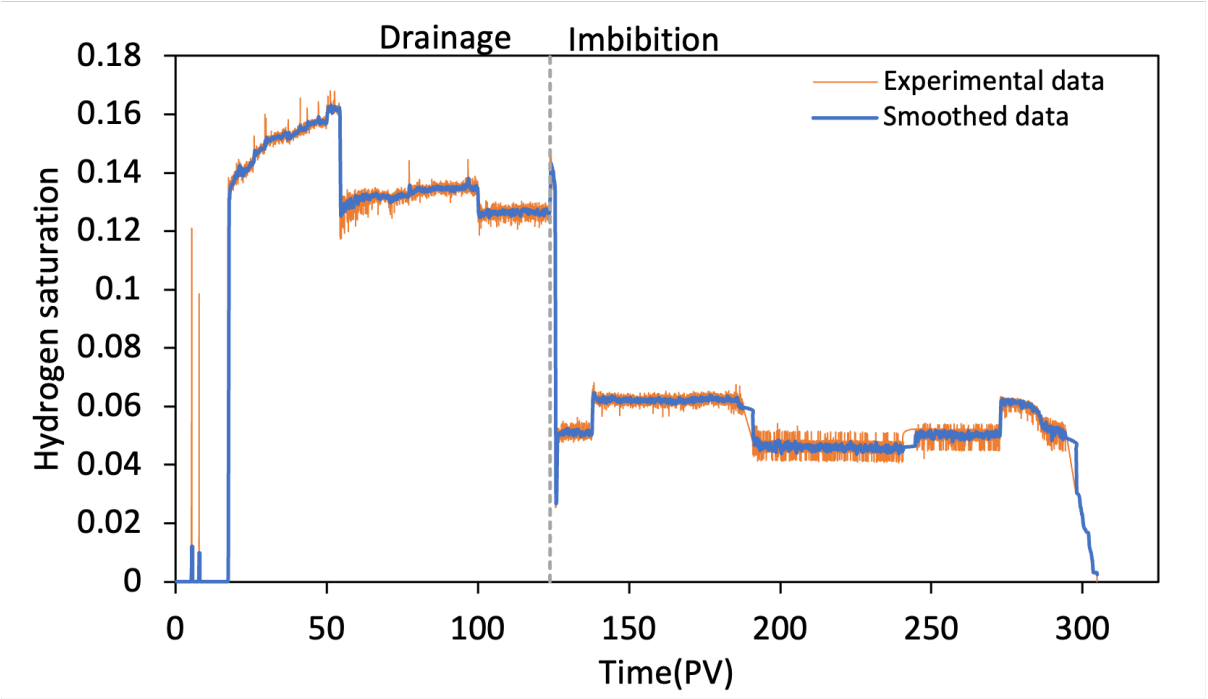

Figure 4.7: Saturation development for exp. A2. Changes in FoV caused changes in the gas saturation curve, even though the saturation was observed to be constant.

4.4 Comparison to previous work

Previous work was also analysed to study the uncertainty of the image analysis method. Hart [40] wrote his thesis as a part of a research group at the Department of Physics and Technology at UiB, and the raw data has been accessed to study the sensitivity of the image segmentation algorithm. Hart used a mean local porosity at 0.36 ± 0.01. Raw images from Hart has been filtered using the image segmentation algorithm with local porosity at 0.36 $\pm$0.01, and the gas saturations were compared to the original values presented in his thesis. The results can be found in Table 4.2. Figure 4.8 shows an example of filtered images for high and low saturation. The relative uncertainties was in the range 3 % to 27 %, but the relative uncertainties was the range from 3 to 14% if the maximum is excluded. The raw data and published data were not presented in the same order, and an estimate based on calculated injection rate from Hart's experimental data log (pressure and volume) has been used to identify the capillary number corresponding to each experiment. Hence, it may not be the exact numbered experiment located and could explain the deviations for some of the experiments (e.g. exp. H4). The range was corresponding with previous uncertainty measurements in Table 4.1, and supports the assumption of 12 % relative uncertainty for most experiments.

P

Table 4.2: Comparison end-point saturations. Raw images from Hart (2021) [40] was analysed using the image segmentation algorithm. S_{g1} is the experimental data from [40] and S_{g2} is the experimental data using the image segmentation algorithm on the raw data.

	Parameters			**Previous work**		**Comparison**		
Exp.#	Q [ml/h]] ±0.02%	P[bar] ±1.5*bar*	N_c ±0.02%	S_{g1}	$u(S_{g1})$	S_{g2}	$S_{g1} - S_{g2}$	$u_R(S_{g2})$
H1	10	1	7.70E-05	0.65	0.02	0.742	0.092	14.2 %
H2	25	1	1.90E-04	0.67	0.02	0.726	0.056	8.3 %
H3	50	1	3.80E-04	0.67	0.02	0.732	0.062	9.2%
H4	1	30	7.87E-06	0.09	0.01	0.115	0.025	27.4 %
H5	10	30	7.70E-05	0.53	0.02	0.531	0.001	0.1%
H6	50	30	3.90E-04	0.61	0.02	0.639	0.029	4.8 %
H7	0.1	1	7.70E-07	0.05	0.02	0.49	-0.001	2.6 %
H8	1	30	7.80E-06	0.09	0.02	0.100	0.010	10.6 %

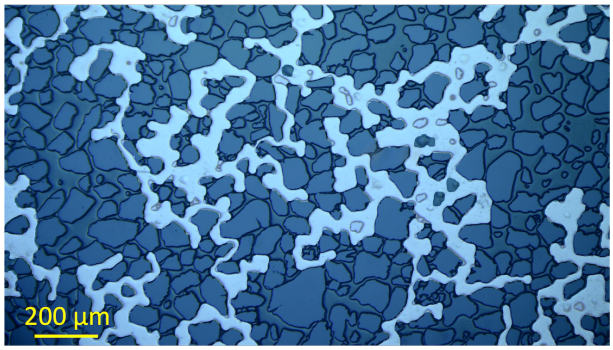

(a) 10 ml/h at 1 bar (100PV)

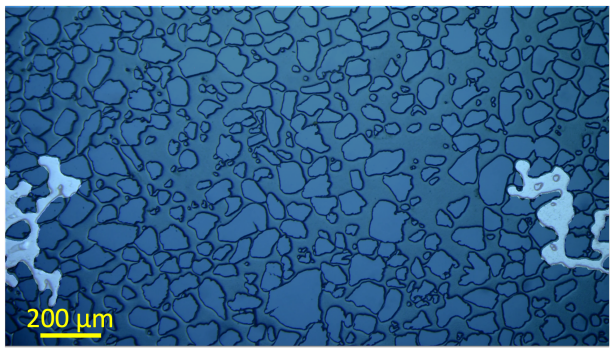

(b) 1 ml/h at 30 bar (100PV)

Figure 4.8: Filter accuracy compared to previous work. a) Primary drainage at 10 ml/h and 1 bar injected for 100PV. b) Primary drainage at 1 ml/h and 30 bar injected for 100 PV.

Chapter 5

Results and Discussion

A total of 15 experiments were performed at 40 bar and room temperature using different capillary numbers with the objective to investigate hydrogen displacement, hydrogen saturation, residual trapping and contact angles.This chapter will present the experimental results for primary drainage, imbibition and cyclic injection. The local porosity of the FoV was calculated for each experiment due to the porosity dependence of hydrogen saturation.

5.1 Local porosity

The FoV porosity was calculated for each experiment because the FoV was only covering a small percentage of the micromodel. Approximately the same location was used for the experiments, but deviations could occur due to the manual adjustment of the FoV The porosity was calculated by two methods, grain method (Formula (2.5)), where the grain area was measured, and pore method (Formula (2.6)), where the pore space area was measured. The FoV porosity for the different experiments are presented in Table 5.1, where the grain and pore space methods are labelled "grains" and "pores", respectively. The mean porosity was estimated to 0.44 ± 0.01, where the uncertainty was the combined uncertainty based on standard deviation and the relative colouring uncertainty.

The porosity uncertainty was generally low for all experiments. The uncertainty for each experiment was the standard deviation based on the porosity from grains and pore space pixels. Note that even though two porosity values are presented, the image was only coloured once by colouring of the grains. The uncertainty could be different if the pore space was coloured manually as well. The presented uncertainty represents the precision of including all pixels in the coloured image. The method by adding layers was expected to have higher precision compared to colouring the grains by free hand and bucket tool. The porosity of B5-1 was calculated 3 times in total to determine the colouring uncertainty, resulting in a relative uncertainty at 0.2% and is used as the colouring uncertainty. The result indicates that a high precision was obtained for local porosity, however, uncertainties in accuracy and systematic error might occur but were harder to calculate. Other systematic uncertainties are the restrictions of the FoV. The FoV was covering about $\sim 1\%$ of the micromodel and grains were cut at the edges of the FoV. It was not possible to observe or determine fluid behaviour or grain structure beyond the edges of the FoV. Pore space could be enclosed by grains just outside the edges. The

Table 5.1: Local porosity for the experiments. The local porosity was calculated based on measurments of both grain and pore space area. *:The colouring of grains were performed 3 times and mean values are presented.

	Exp.#	Method	Area[px]	ϕ	Mean	$u(\phi)$
Part A	A1	grains	1187336	0.427403549	0.427403549	0
		pores	886264	0.427403549		
	A2	grains	1164181	0.43857012	0.438571	2-06
		pores	909424	0.438572531		
	A3	grains	1206646	0.418091242	0.4180915	3E-07
		pores	866955	0.418091725		
	A4	grains	1186371	0.427868924	0.427871	3E-06
		pores	887238	0.427873264		
Part B	B5-1*	grains	1216038	0.413561921	0.4136	9E-4
		pores	857548	0.41355517		
	B5-2	grains	1139783	0.45033613	0.45033	2E-05
		pores	933773	0.450314911		
	B6-1	grains	1133361	0.45343316	0.45342	2E-05
		pores	940183	0.453406154		
	B6-2	grains	1143720	0.4484375	0.4484375	6E-17
		pores	929880	0.4484375		
	B7-1	grains	1140880	0.449807099	0.44976	6E-05
		pores	932537	0.449718846		
	B7-2	pores	1147721	0.446508005	0.44648	3E-05
		grains	925778	0.446459298		
	B8-1	grains	1130886	0.454626736	0.45462	1E-05
		pores	942681	0.454610822		
	B8-2	grains	1158857	0.441137635	0.441137635	6E-17
		pores	914743	0.441137635		
$u_R(Colouring)$			-	-		0.2%
Mean porosity			-	-	0.44	0.01

pore space at the edges was assumed to be in a connected network for simplicity. The grain colouring uncertainty was the dominant factor for porosity. However, the assumed relative uncertainty at 12% for the image segmentation algorithm would be dominating in the saturation calculations, and the porosity uncertainty could be neglected.

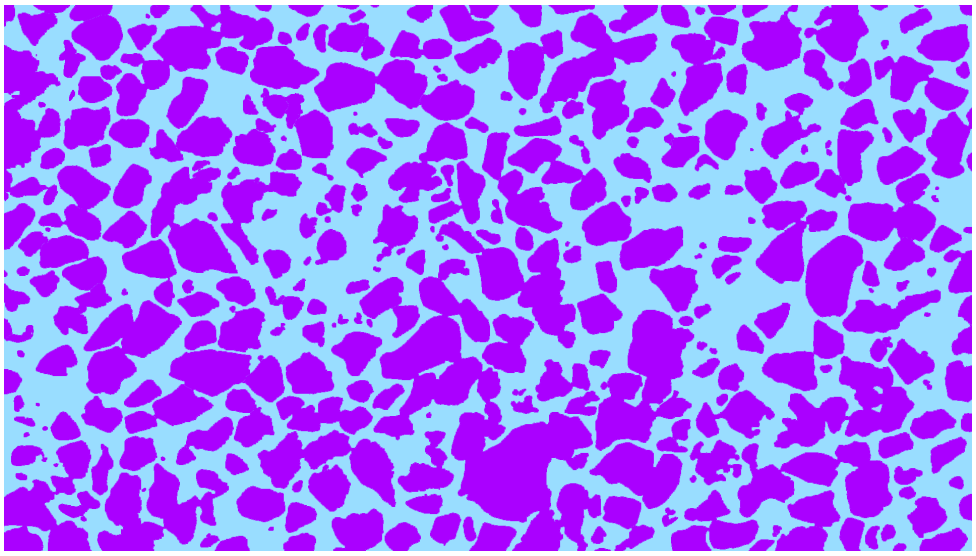

Figure 5.1: Local porosity. Manually grain colouring of the FoV of exp. B8-2 with local porosity ~ 0.44. The porosity was calculated based on pixel measurements using ImageJ.

5.2 Primary drainage and imbibition

Knowledge of primary drainage and imbibition processes is essential to understand hydrogen displacement and residual trapping in porous media. End-point drainage saturations, $S_{g,dr}$, describes the storage capacity of a formation, while end-point imbibition saturations, $S_{g,imb}$, gives an indication of the potential gas loss to the formation. The effect of capillary number, pressure and recovery on primary drainage and imbibition will be studied in this chapter, where the capillary numbers and experimental conditions for the experiments are found in Table 5.2. The capillary numbers was calculated by Formula 2.4[1].

Table 5.2: The capillary number N_c used for the different experiment.

Exp#	N_c
A1	7.59E-07
A2	7.59E-06
A3	7.59E-05
A4	3.80E-04

5.2.1 Methodical limitations

The study of fluid behaviour in a micromodel gives valuable insight in displacement mechanisms and residual trapping. However, the microscope used in the experimental setup has a limited FoV where only approximately 1% of the micromodel was observed. In addition, the choice of operational mode of the pumps resulted in fluctuation hydrogen injection to maintain the micromodel pressure. This section will describe the limitations of the method used for primary drainage and imbibition.

[1]The experiments was performed at room temperature, and the water viscosity was set to $\sigma = 0.001002 N/m$. The hydrogen IFT was calculated to $\mu = 0.072733 Pas$ based on extrapolation of the presented hydrogen-water IFT to 40bar at $25°C$ in Chom et. al's paper [56].

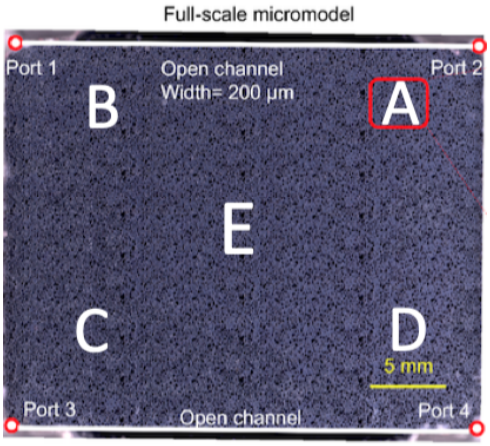

Figure 5.2: The positions used in the study of location dependency for hydrogen saturation in the micromodel. Position A is used for the experiment conducted in the thesis.

Gas displacement in and out of the FoV caused is a limitation of the experimental setup. A FoV of the entire micromodel would enable a deeper study of fluid distribution and flow patterns. It could also be valuable to observe the water distribution in the understanding of relative permeability, residual trapping and displacement of hydrogen in the micromodel. The local displacement in the FoV could give a false impression of the hydrogen saturation and distribution during both drainage and imbibition. By theory, hydrogen saturation will increase when gas is injected into the micromodel. However, it could appear that the hydrogen saturation decreases when the observations was limited to the FoV, even though the overall hydrogen saturation of the micromodel increased.

Still images was captured in different locations at the end of drainage and during imbibition to study the representation of the experimental data for the entire micromodel. The micromodel consisted of a repeated network of grains, and approximately identical grain structures to the FoV were chosen to investigate if the location would affect end-point hydrogen saturations. The positions in the micromodel is illustrated in Figure 5.2, and the corresponding saturations is found in Table 5.3. $u(S_{g,dr})$ and $u(S_{g,imb})$ are the uncertainty for drainage and imbibition gas saturation, respectively.

Table 5.3: Saturation by manually colouring of gas in different position A-E in the micromodel for exp. A4.

Exp.#	Position	$S_{g,dr}$	$u(S_{g,dr})$	$S_{g,imb}$	$u(S_{g,imb})$
	A	0.596	0.002	0.295	0.001
	B	0.437	0.002	0.315	0.001
A4	C	0.322	0.001	0.1199	0.0005
	D	0.509	0.002	0.2293	0.0009
	E	0.409	0.002	-	-
	Mean	0.5	0.1	0.24	0.9
	u_R		0.2		0.4

The end-point values for different position indicates a location dependency. The end-point drainage saturation was in the range from 0.32 to 0.60 with a mean saturation at 0.5 ± 0.1, while the saturations during imbibition was between 0.12 to 0.32 with mean 0.2 ± 0.9. The relative uncertainty of the mean for drainage was 20%, while the relative uncertainty

for imbibition was the doubled at 40%. The drainage hydrogen saturations could indicate a correspondence between saturation and choice of FoV. The lowest drainage hydrogen saturation (0.322 ± 0.001) was observed near the water inlet in port 3 where the distance from hydrogen outlet in port 2 was largest, where the second lowest was observed in position E in the centre of the micromodel with the largest distance from the distribution channels. For imbibition, the lowest hydrogen saturation was observed in position C, closest to the water outlet, and the highest saturation was observed in position B. The second highest saturation was in position A, and a similar trend to drainage saturation could be observed.

The choice of operation mode for the hydrogen pump due to the compressability of hydrogen would affect the actual injection rate and hence capillary number for the experiments. The fluctuating hydrogen injection rate for a primary drainage at 10ml/h is shown in Figure 5.3, where the hydrogen pump was at operating at constant pressure mode, while the water pump was retracting fluids at constant rate at 10 ml/h. Consequently, the hydrogen rate was not constant spanning a large set of values, and the mean injection rate could be different than the stated experimental rate. Hence, the capillary number should be different. The injection rate was not recorded during this part of the experiments, and a record would give a more detailed description of the actual hydrogen injection rate used for the experiments and potential effects of the fluctuation hydrogen rate. The constant pressure mode was used to maintain the pressure in the micromodel, and the pressure development during drainage is observed in Figure 5.3. The jump in water pressure was observed a few seconds before the gas entered the FoV. The curve shows that the pressure difference between the pumps was maintained, but the overall pressure fluctuated during the drainage. As shown in Figure 5.3(b), the pressure change of the hydrogen pump and water pump is consistent, even though the hydrogen pump was working as constant pressure mode during injection. This might be related to the sensitivity of the Quizix pumps which need more time to respond to the pressure changes. Therefore, the current method was not able to obtain the pressure drop data during drainage.

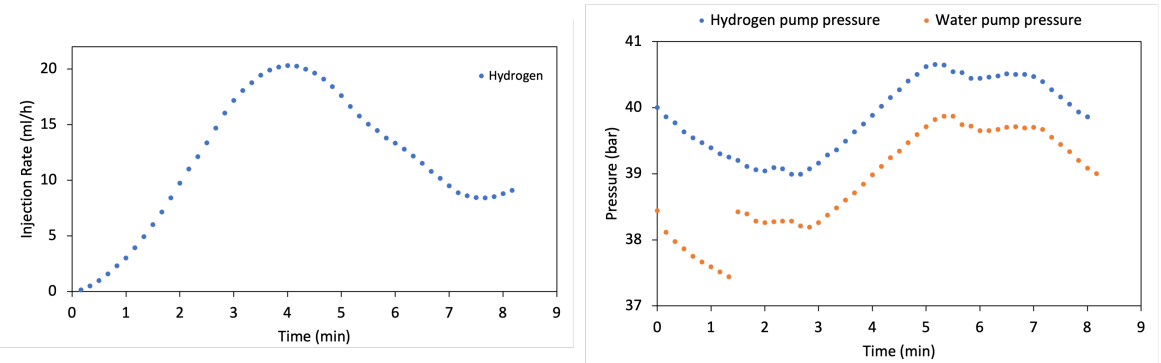

Figure 5.3: Pump behaviour using constant pressure at the gas pump. Left figure: Injection rate primary drainage at 10ml/h. The water pump was set to constant rate, while the hydrogen pump was set to constant pressure mode resulting in alternating injection rate. Right figure: Pressure development for hydrogen and water pump when water is retracted at 10ml/h and the hydrogen pump is operating on constant pressure mode.

5.2.2 Hydrogen displacement during drainage and imbibition

In order to understand the displacement mechanisms and storage potential in an UHS system, it is important to study the saturation development during drainage and imbibition processes. Primary drainage and imbibition were performed at different capillary numbers to study end-point hydrogen saturation, residual gas and gas recovery. Figure 5.4 shows the saturation development during primary drainage and imbibition for exp. A4. Fluctuations in the experimental data can be observed and was caused by the filter uncertainty addressed in Chapter 4 Method sensitivity. Unintended movements of the microscope caused noise in the filtered images and an change in hydrogen saturation in the experimental data, as observed after t = 450 PV. The experimental data from the image segmentation algorithm was smoothed with a moving average over 10 points. Note that the figure presents the experimental data based on the image segmentation algorithm, but the end-point saturations in Table 5.4 was calculated based on manually mapping of hydrogen.

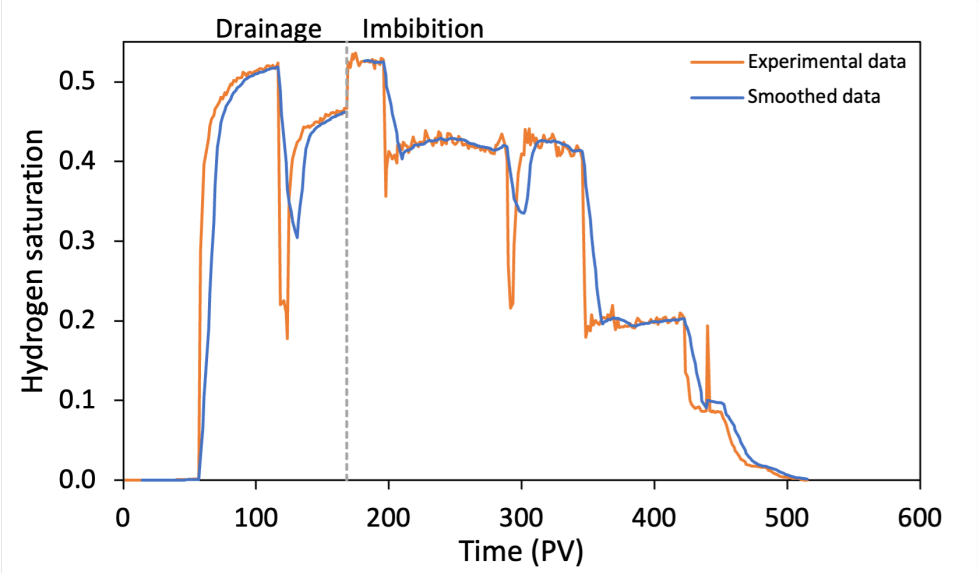

Figure 5.4: Saturation development for exp.A4 at Nc = $3.8 \cdot 10^{-4}$. Primary drainage were performed for 100PV after hydrogen was observed in the FoV.

Fluctuations in the saturation development was observed during both drainage and imbibition. However, an increase in gas saturation would be expected based on primary drainage theory. No gas was observed in the FoV until 50 PV of hydrogen was injected into the micromodel. The delayed increase in hydrogen saturation was partly caused by the threshold pressure of the pore structure, but was also an effect of the limited FoV. Gas increase in the micromodel would be expected at the beginning of drainage when the threshold pressure was reached. However, in micromodel experiments with a limited FoV, the gas displacement outside the FoV is unknown. Even though the hydrogen saturation was expected to increase towards a maximum end-point saturation during drainage, a saturation decrease was observed when 50 PV was injected after gas entry in the FoV at t = 120 PV.

The terms *local* and *global* displacement was defined to describe the hydrogen behaviour in the micromodel for gas displacement to distinguish between gas displacement in the FoV and outside the FoV. Global gas displacement was defined as gas displacement out-

side the FoV. The gas in the FoV was mobilised by global displacement events outside the FoV and could not be controlled nor observed. A local gas displacement was defined as the gas displacement observed in the FoV. The analysis performed in this thesis will be on local displacements in the FoV, but the local displacement will be dependent on global displacements. After the local gas displacement at t = 120 PV, the gas saturation increased to $S_g = 0.47$ when a total of 100 PV was injected. Similar local FoV effects was observed during imbibition. By definition, the gas saturation should have decreased when water was injected. A decrease in hydrogen saturation was observed after approximately t = 120 PV. The waterfront displaced gas locally, and snap-off and bypass caused residual trapping of hydrogen. The fluctuations during imbibition was caused by local gas displacement induced by globally displaced gas bubbles, and the fluctuating behaviour could shows that hydrogen was relatively easy to mobilise by water. A stepwise decrease in saturation was observed during imbibition until t = 400 PV where the hydrogen saturation had stabilised, indicating that the water flow paths was established. The remaining gas in the pore structure was immobilised, and a residual gas saturation was reached. The residual gas saturation was $S_g \approx 0.2$ and represents the amount of gas that cannot be extracted from a formation at the given conditions. The residual gas saturation will be referred to as end-point imbibition in this chapter. A minimum of residual trapping is preferred for UHS in order to have the highest round-trip energy efficiency. The further saturation reduction was caused by dissolution and does not represent an additional gas recovery because the dissolved gas will be lost to the formation water.

The observed increase between end-point drainage and start-point imbibition saturation in the experimental data in Figure 5.4 could be caused by several factors. The difference was partially be caused by the sensitivity of the image segmentation algorithm to water accumulation, as discussed in Chapter 4.1 Uncertainty from water accumulation and grains. Less water accumulations was observed in the gas at the maximum point and at the beginning of imbibition compared to the end of the drainage. The amount of water accumulations was reduced with increasing PV hydrogen injected during drainage, and the observation is supported by previous work [40],[41]. Hence, it could indicate that end-point drainage saturation could reach a saturation at ~ 0.52, similar to the first maximum point, if more PV was injected. A small gas expansion was also observed for some experiments when the pressure stabilised to equilibrium in the micromodel when the hydrogen injection was stopped after drainage. In addition, drainage and imbibition was recorded in different videos, and the observed increase of a few percentages between end-point drainage and start-point of imbibition could be caused by the effect of sequential videos and images discussed in Chapter 3.3 Image analysis. Lastly, the microscope was moved between drainage and imbibition, and the FoV was changed slightly. Different FoV could results in different saturations, even though the hydrogen in the FoV was observed to be static.

5.2.3 Effects of capillary number and pore pressure

It is important to know the effects of capillary number during drainage and imbibition to find the best suited flow conditions for UHS. Primary drainage at different capillary numbers showed a positive correlation between saturation and capillary numbers. An overview of the end-point hydrogen saturations and recovery is found in Table 5.4. The highest end-point drainage hydrogen saturation observed was at 0.596 ± 0.002 for the highest capillary number, while the lowest saturation was observed for the lowest capillary

number at 0.0365 ± 0.0001. Figure 5.5 shows the local end-point hydrogen distribution for drainage at different capillary numbers. The gas distribution was affected by the local pore structure, grain distribution and pore radius. The capillary pressure is defined as the pressure difference between hydrogen and water pressure, but is also inverted proportional with the pore radius. For low capillary numbers, the gas flow was blocked by the high capillary pressure in narrow pore throats and was unable to enter the pores connected to the larger networks in the centre of the FoV, resulting in a lower hydrogen saturation. The gas distribution for different capillary numbers is shown in Figure 5.5, where 5.5(a) and (b) shows that the gas was located at the edges of the FoV for the lowest capillary numbers. Narrow pore throats was also observed in the same area, blocking the gas flow. A correlation between residual trapping and capillary number was also observed. The end-point hydrogen saturations for imbibition presented in Table 5.4 represent the residual gas that was immobilised and trapped by the pore structure, and were measured when disconnected bubbles were observed and no further local gas displacements were expected.

Table 5.4: End-point saturation for drainage and imbibition for the different experiments.$S_{g,dr}$: end-point drainage saturation, $S_{g,imb}$: end-point imbibition saturation.

Exp.#	N_c (±0.2%)	$S_{g,dr}$ (± 0.3%)	$S_{g,imb}$ (±0.3%)	$S_{g,dr} - S_{g,imb}$
A1	$7.59 \cdot 10^{-07}$	0.0365	0.00648	0.0301 ± 0.0001
A2	$7.59 \cdot 10^{-06}$	0.1308	0.0556	0.0752 ± 0.0005
A3	$7.59 \cdot 10^{-05}$	0.570	0.1928	0.377 ± 0.002
A4	$3.80 \cdot 10^{E-04}$	0.596	0.0295	0.301 ± 0.003

Similar gas behaviour is observed during primary drainage and imbibition in the literature. A relationship between increasing capillary number and increasing end-point hydrogen saturation was observed at 1 bar and 40 bar with hydrogen injection rates at 0.1, 1, 10, 25 and 50 mL/h . The results showed a pressure dependency at higher capillary numbers. Experiments by Lysyy et al.[41] at 5 bar with injection rates at 0.1, 1, 10 and 50 mL/h did also show increase in gas saturation with increasing capillary numbers.

A CDC curve was modified to UHS to describe the relationship between pressure, capillary number N_c and the lowest possible water saturation (irreducible water saturation) during drainage [40]. The relationship between the irreducible water saturation and capillary number is shown in Figure 5.6, where experimental data from Hart [40] at 1 and 30 bar was included. The figure shows that irreducible water saturation decreased with increasing capillary number. Hence, an increased hydrogen saturation and storage capacity is expected with increasing capillary number. The water saturation for 1 bar approached a lower irreducible water saturation limit, indicating the maximum hydrogen capacity for the formation. The water saturation at 40 bar approach similar saturations to 30 bar, indicating that the pressure difference at 10 bar did not affect the irreducible water saturation. However, a pressure dependency was observed between 1 bar and 30/40 bar where pore pressure had higher effect at high capillary number, but the dependency might be reduced with system pressures above 30 bar. Studies by Lysyy et al. present a hydrogen saturation as high as $S_g = 0.8$, lower than corresponding saturation for 1 bar, which contradict with a pressure dependency for increasing gas saturation [41]. At the same time, a gas saturation at $S_g = 0.41$ was observed for $N_c = 7.68 \cdot^{-5}$, lower than gas saturation with pore pressure at 1 bar, 30 bar and 40 bar. Experiments by Lysyy et al. and Hart

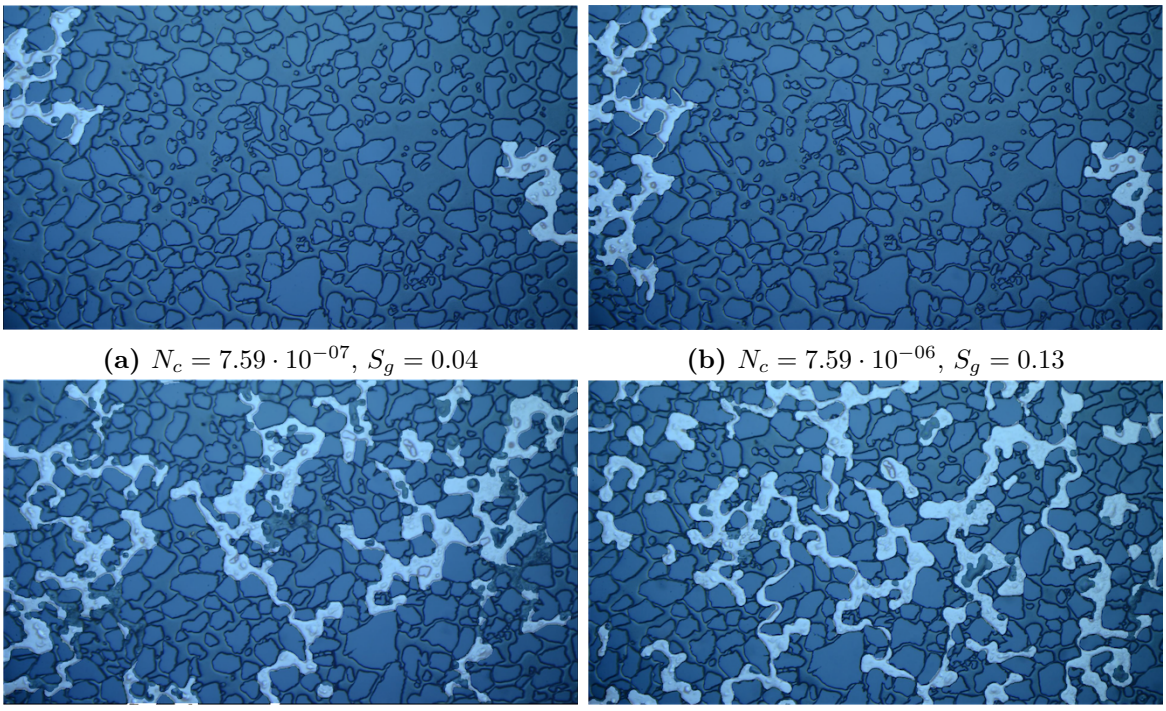

(a) $N_c = 7.59 \cdot 10^{-07}$, $S_g = 0.04$ **(b)** $N_c = 7.59 \cdot 10^{-06}$, $S_g = 0.13$

(c) $N_c = 7.59 \cdot 10^{-05}$, $S_g = 0.57$ **(d)** $N_c = 3.80 \cdot 10^{-04}$, $S_g = 0.60$

Figure 5.5: End point saturations. End-point saturations for primary drainage the experiments after 100PV. a)$N_c = 7.59 \cdot 10^{-7}$ b) $N_c = 7.59 \cdot 10^{-6}$ c)$N_c = 7.59 \cdot 10^{-7}$ d) $N_c = 3.80 \cdot 10^{-4}$.

was performed independently with a micromodel with limited FoV. The choice of FoV and FoV position could therefore have affected the gas saturations due to different local porosity and pore structure. Only a small change in FoV would change the gas saturation, as observed in Chapter 4 Method sensitivity and Chapter 5.2.1 Method limitations. Future work should study pore pressure dependency where the entire micromodel would be analysed to avoid FoV effects.

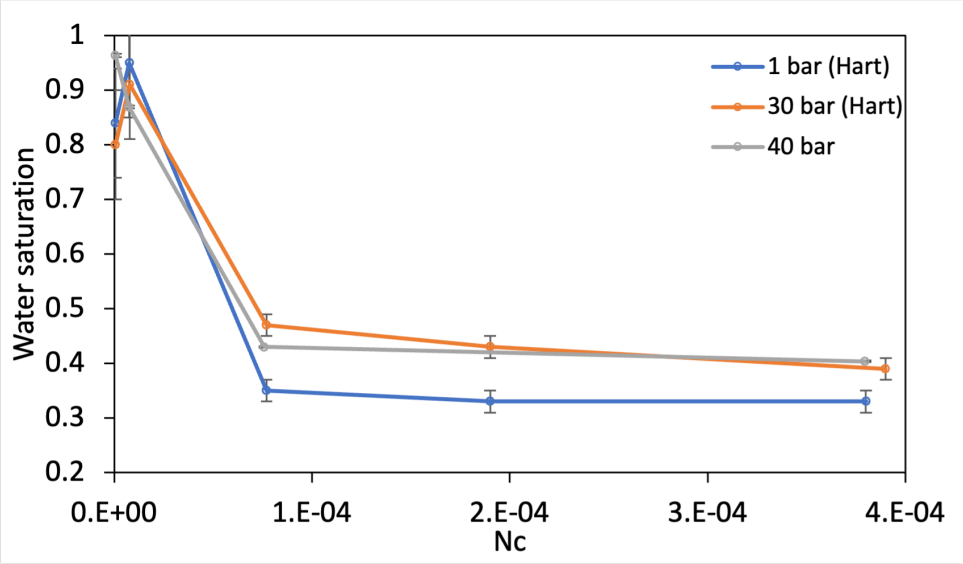

Figure 5.6: Modified Capillary Desaturation Curve at 1 bar, 30 bar and 40 bar. 1 bar and 30 bar saturation data by Hart[40].

5.2.4 Hydrogen recovery

The objective of underground hydrogen storage is to temporarily store gas with withdrawal after demand. Ideally, all stored gas would be recovered, where residual trapping would reduce the efficiency of the storage facility. The recovery for the experiments is presented in Table 5.4. The recovery for different capillary numbers was within the same range with overlapping uncertainties. A relationship between increased recovery by capillary was observed for $N_c >= 7.59 \cdot 10^{-6}$, but the highest recovery was observed for the lowest capillary number at $\sim$ 82%. The hydrogen recovery R_f was calculated based on the saturation difference between end-point drainage and imbibition relative to the end-point drainage saturation:

$$R_f = \frac{S_{g,dr} - S_{g,imb}}{S_{g,dr}}$$

Table 5.5: End-point saturation for drainage and imbibition and hydrogen recovery for the different experiments.

Exp.#	N_c (±0.2%)	$S_{g,dr}$ (± 0.3%)	$S_{g,imb}$ (±0.3%)	$S_{g,dr} - S_{g,imb}$	R_f[%]
A1	7.59E-07	0.0365	0.00648	0.0301	82.3 ± 0.05
A2	7.59E-06	0.1308	0.0556	0.0752	57.5 ± 0.05
A3	7.59E-05	0.570	0.1928	0.377	66.2 ± 0.05
A4	3.80E-04	0.596	0.0295	0.301	50.5 ± 0.05

The gas distribution and residual trapping was affected by the local pore structure. Residual trapping occurs when gas enters pores followed by a snap-off from the main flow when hydrogen is displaced by water and was observed for all experiments. However, the gas distribution during drainage would affect the potential of residual trapping during imbibition. For the lowest capillary number, the gas flow was blocked by the high capillary pressure in small pore throats and was unable to enter the pores connected to the larger networks during drainage. If hydrogen did not pass through a narrow pore throats during drainage, less residual trapping was observed and hence a higher recovery was achieved. The residual trapping was lower for the lowest capillary number because most of the gas was connected in the largest pores at the edges of the FoV. The highest gas recovery was observed for the lowest capillary number, but the recovery could be misleading due to the low injection rate where only small volumes were recovered. For higher capillary numbers, local displacement was initiated by global displacement events and could have effected the end-point drainage saturations and the actual recovery. Hence, the recovery should be used with precaution in micromodel studies where a limited FoV is used.

5.3 Cyclic injection

The effect of cyclic injection of hydrogen and water on gas displacement and residual trapping will be studied in this chapter to get valuable insight into hydrogen behaviour in UHS. Hydrogen will be injected over several cycles during UHS, depending on the hydrogen production and demand. The experimental setup was developed to study cyclic injection, where drainage and imbibition were performed in 4 to 5 cycles for different

capillary numbers. The cycles will be referred to as cycle 1 (C1), cycle 2(C2) etc. The experimental time period at 800PV is not realistic for cyclic injection on a field scale, but the PVs per cycle were necessary in the experiments due low flow rates and small volumes.

5.3.1 Hydrogen displacement during cyclic injection

The gas saturation during cyclic injection was studied to examine displacement mechanisms and potential gas trapping by the pore structure. Figure 5.7 shows the hydrogen saturation development for exp. B8-2 at $N_c = 7.59 \cdot 10^{-5}$. Hydrogen saturation development for other capillary numbers can be found in Appendix C.

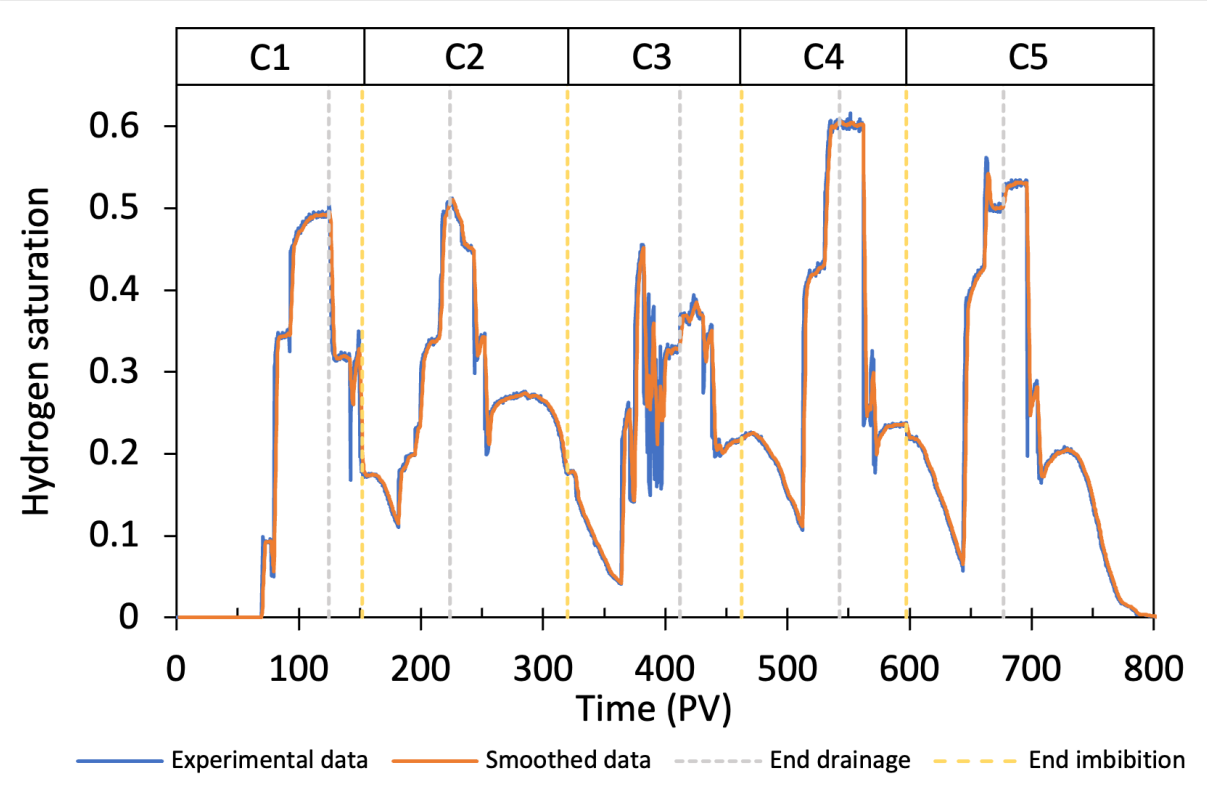

Figure 5.7: Saturation development for exp. B8-2 for 5 cycles where the cycle number is at the top of the figure. Grey lines indicate the end of drainage and the start of imbibition and yellow lines indicate the end of imbibition and the start of drainage in the sequential cycle.

Generally, the hydrogen saturation increased during C1 drainage and decreased during C1 imbibition, similar to the observations for primary drainage and imbibition for exp.A1-A4. The gas saturation was constant during the first 70 PV injected while the gas pressure increased for C1 drainage. A stepwise increase in gas saturation was observed while the gas pressure increased. However, the fluctuations in the the plateaus during C1 drainage was not caused by local displacement through the FoV. A small gas retraction occurred at the first plateau before an additional gas increase was observed, while one spike was observed in the second plateau, caused by a rapid gas displacement in the FoV. The increased gas pressure allowed the gas to penetrate narrow pore throats, and a large pore area was filled with gas. The gas displacement was so quick that the hydrogen-water interface was not defined in the raw images. In addition, the gas had a temporary darker

colour that was not detected during the displacement. The gas saturation stabilised after injection of 50 PV after gas entry in the FoV indicating a steady-state flow where further gas displacements were not expected. 50 PV was injected for C1 drainage to ensure that the hydrogen saturation was stabilised and that the maximum gas saturation was reached. A smaller amount of PV was injected after gas entry for the other cycles, with 40 PV for C2, 40PV for C3, 30PV for C4 and 30 PV for C5.

The saturation development behaved differently when the micromodel was gas saturated for drainage in C2 to C5. A decrease in gas saturation due to hydrogen dissolution in water was observed at the beginning of the drainages caused by a delay in the FoV. The global drainage began when hydrogen penetrated the pore network in the micromodel. However, the C2 drainage was delayed locally because the gas front did not reach the FoV until 50 PV was injected into the micromodel. Hydrogen dissolution was also observed during primary imbibition for exp. A1-A4, and the gas present in the FoV experienced a local imbibition when water was displaced by gas globally. The residual gas was dissolved while the gas pressure increased caused by the hydrogen injection into the micromodel. A similar development in gas saturation was observed for C2, C4 and C5 for the local drainage, but the end-point gas saturations could vary, which is an hysteresis hysteresis effect where path dependency and saturation history will affect the gas saturation for identical processes. Fluctuations in gas saturation were observed over 30 PV (from t = 380 PV to t = 410 PV) for C3 drainage where several local gas displacements were observed after a maximum gas saturation was reached. The local gas distribution resulted in a lower end-point saturation than the maximum gas saturation in the cycle.

The end-point gas saturation for drainage per cycle increased in all cycles except for C3 drainage. However, hydrogen was missed during image segmentation for C3 end-point hydrogen saturation. A comparison of the original image and filtered image for C3 maximum hydrogen saturation after 30 PV, C3 end-point hydrogen saturation after 40 PV and C1 end-point hydrogen saturation after 50 PV is shown in Figure 5.8. The PVs are the PV injected after gas entered the FoV. Hydrogen was missed in the locations where small water accumulations caused a darker colour, as discussed in chapter 4 Method sensitivity. The C3 maximum gas saturation (Figure 5.8(c)) missed gas to the left and in the centre of the FoV. The overall error in the image segmentation was higher for C3 compared to C1 because less PV was injected at a stable gas distribution, and more water accumulations were observed in both Figure 5.8(c) and (d). C3 maximum hydrogen saturation was calculated to $S_g = 0.45 \pm 0.05$, with an upper bound at $S_g = 0.50$. The value is within the uncertainty range of C1 end-point drainage hydrogen saturation at $S_g = 0.49 \pm 0.06$, which is reasonable based on the gas distribution in Figure 5.8(c) and (d). The gas distribution shows that the maximum hydrogen saturation for C3 should be similar to C1 end-point hydrogen saturation, but local displacements caused a saturation decrease during the C3 drainage. C3 illustrates the limitations of a limited FoV. Gas was displaced in and out of the FoV several times before the hydrogen saturation stabilised.

The hydrogen saturation development during imbibition was similar for all cycles in Figure 5.7. Generally, the hydrogen saturation was decreased stepwise for each cycle. However, a small difference between end-point drainage and start-point imbibition hydrogen saturation was observed for C3 and C5. As discussed in the previous chapter, experiments showed a decrease water accumulations after the hydrogen injection was ended, increasing the hydrogen saturation in the experimental data. The amount of water accumulations were expected to be higher at the end of the drainages for the cycles due to local displace-

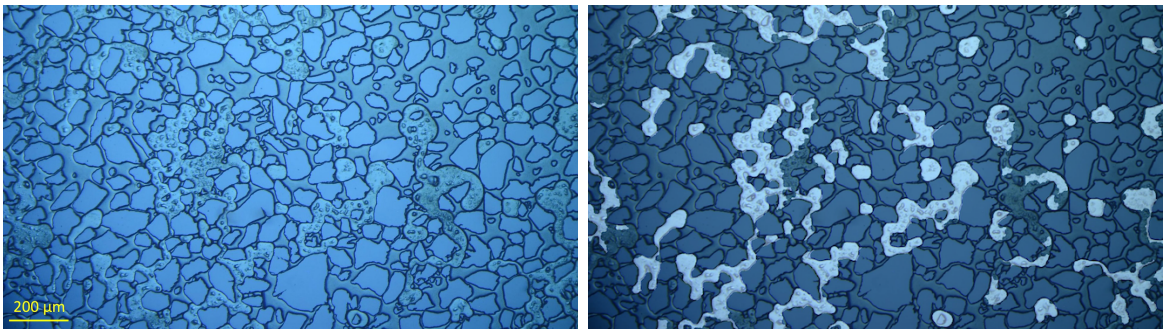

(a) C3 end-point saturation original image

(b) C3 end-point saturation, $S_g = 0.34 \pm 0.04$

(c) C3 maximum saturation, $S_g = 0.45 \pm 0.05$

(d) C1 end-point saturation $S_g = 0.49 \pm 0.06$

Figure 5.8: Third cycle comparison for $N_c = 7.6 \cdot 10^{-5}$(Exp.B8-2). Comparison of image filtering for different PV injected after gas entry in the FoV. (a) Original image of C3 maximum saturation, (b) the maximum saturation in C3 at 27PV, (c) and end-point saturation in C3 at 40PV, (d) and end-point saturation in C1 after 50PV.

ment at the end of the injection period. However, C3 had a fluctuating increase compared to C4.The end-point imbibition hydrogen saturation was affected by the amount of local gas displacement during imbibition. The hydrogen saturation decrease stepwise during C1 imbibition, while the fluctuations in hydrogen saturation were caused by local gas displacement by the water front, similar to what was observed for C1 drainage. A similar trend was observed for imbibition in all cycles but with variations in end-point imbibition saturation. The fluctuations with largest span in the experimental data during imbibition had the lowest hydrogen end-point hydrogen saturation. For instance, a rapid saturation change was observed in C1, resulting in the lowest imbibition hydrogen saturation for all cycles. Less fluctuations was observed for C2 imbibition, which also had the highest end-point imbibition saturation, even though it was observed that the imbibition was stopped after dissolution had begun. The imbibitions was stopped manually when disconnected gas was observed, preferably before dissolution had started, to study the drainage behaviour and residual trapping in the sequential cycle when the pore network was hydrogen saturated. The end-point imbibition hydrogen saturation was highest for C2 even though the imbibition was stopped after dissolution had started. The fact that the dissolution had started during imbibition resulted in a larger decrease during the local imbibition at the beginning of C3 drainage.

5.3.2 Effects of cyclic injection on hydrogen saturation

It is important to understand the effects of cyclic injection on hydrogen saturation when geological formations are used as storage media. Table 5.6 gives an overview of the

end-point hydrogen saturation for drainage and imbibition for the cyclic experiments. Experiments on each capillary number was performed twice to study the reproducibility and potential hysteresis effects. The negative difference between $S_{g,dr}$ and $S_{g,imb}$ for C1 in exp. B5-2 was caused by local displacement through the FoV, resulting in a higher gas saturation at the end of imbibition compared to drainage gas saturation. Exp.6-2 and exp. B7-2 was performed by post-doc Na Liu.

The relationship between end-point gas saturation during drainage for each cycle is shown in Figure 5.9. The end-point saturation per cycle showed a stable or increased end-point saturation compared to the first cycle for most experiments and capillary numbers. Hysteretic dependency was also uncovered where a difference in gas saturation was observed for experiments with identical capillary numbers caused by different flow distribution per cycle and and experiments. Similar effects has also been observed for cyclic CO_2 experiments [52], [36]. The hydrogen gas distribution for each cycle and experiment was dependent on path and saturation history. The gas distribution was also affected by the pore network and would preferably enter the largest pores where the capillary pressure was lowest. If the established paths did not include the entry to the larger pore areas, a lower gas saturation would be expected for the cycle. There was a relationship between gas saturation with increasing capillary numbers on average for C1, as previously observed in Chapter 5.2 Primary drainage and imbibition. Figure 5.9 indicates that the correlation between capillary number and gas saturation was stronger for C1 drainage, where gas saturation at $N_c >= 3.8 \cdot 10^{-5}$ would approach similar gas saturations. The result is supported by cyclic CO_2-brine flooding during core experiments, where the capillary hysteresis effect was limited to the first and second flooding cycle [36]. The overall range of hydrogen saturations was narrower for C4 and C5, where the increase was largest for the lowest capillary numbers. End-point saturations for both experiments at $N_c = 7.59 \cdot 10^{-6}$ increased from $S_{g,dr} = 0.2$ to $S_{g,dr} = 0.4$ for exp. B5-1 and from $S_{g,dr} = 0.15$ to $S_{g,dr} = 0.35$ B5-2, respectively, resulting in an increase by ~ 100 and $\sim 172\%$. Gas saturation for other capillary numbers did not increase by the same factor. Only two experiments observed a small decrease during the cycles, exp. B6-1 and B7-1, but a overlap in uncertainties was observed between C1 and C5 gas saturations for both experiments. Hence, it could indicate that the gas saturation remained stable or increase during cyclic injection. The presence of residual gas in the pore network before drainage could have enabled connections between channels that would not be possible to enter if the path were not already established, where the effect was highest at lower capillary numbers.

Table 5.6: End-point hydrogen saturation for drainage and imbibition during cycling injection.

Exp.	Nc ±0.2%	Cycle	$S_{g,dr}$ ±12%	$S_{g,img}$ ±12%	$S_{g,dr} - S_{g,imb}$	u($S_{g,dr} - S_{g,imb}$)	R_f	u(R_f)
B5-1	7.59279E-07	1	0.20	0.024	0.17	0.02	88	16
		2	0.053	0.023	0.03	0.007	57	15
		3	0.22	0.039	0.18	0.027	82	16
		4	0.40	0.25	0.14	0.06	36	15
B5-2	7.59279E-07	1	0.15	0.024	0.12	0.02	84	16
		2	0.083	0.058	0.02	0.01	30	15
		3	0.14	0.037	0.10	0.02	74	15
		4	0.04	0.077	-0.03	0.01	-80	26
		5	0.34	0.033	0.31	0.04	90	16
B6-1	1.8982E-05	1	0.45	0.28	0.17	0.06	38	15
		2	0.45	0.44	0.00	0.08	1	17
		3	0.26	0.22	0.04	0.04	14	16
		4	0.41	0.33	0.08	0.06	20	16
		5	0.43	0.30	0.13	0.06	31	15
B6-2	1.8982E-05	1	0.40	0.38	0.02	0.05	5	11
		2	0.49	0.46	0.03	0.06	7	11
		3	0.44	0.42	0.03	0.05	6	11
		4	0.59	0.28	0.30	0.03	52	6
		5	0.63	0.38	0.25	0.05	40	7
B7-1	3.79639E-05	1	0.56	0.22	0.35	0.07	62	15
		2	0.64	0.22	0.42	0.08	66	15
		3	0.50	0.26	0.24	0.07	47	15
		4	0.51	0.23	0.28	0.07	56	15
		5	0.55	0.32	0.23	0.08	42	15
B7-2	3.79639E-05	1	0.44	0.31	0.14	0.06	31	15
		2	0.69	0.32	0.36	0.09	53	15
		3	0.73	0.28	0.45	0.09	62	15
		4	0.57	0.31	0.26	0.08	45	15
		5	0.60	0.31	0.29	0.08	49	15
B8-1	7.59279E-05	1	0.43	0.32	0.11	0.06	26	15
		2	0.53	0.28	0.25	0.07	48	15
		3	0.46	0.29	0.17	0.07	37	15
		4	0.56	0.29	0.28	0.08	49	15
B8-2	7.59279E-05	1	0.50	0.20	0.29	0.06	59	15
		2	0.50	0.17	0.33	0.06	66	15
		3	0.36	0.22	0.14	0.05	39	15
		4	0.60	0.23	0.37	0.08	61	15
		5	0.52	0.20	0.31	0.07	61	15

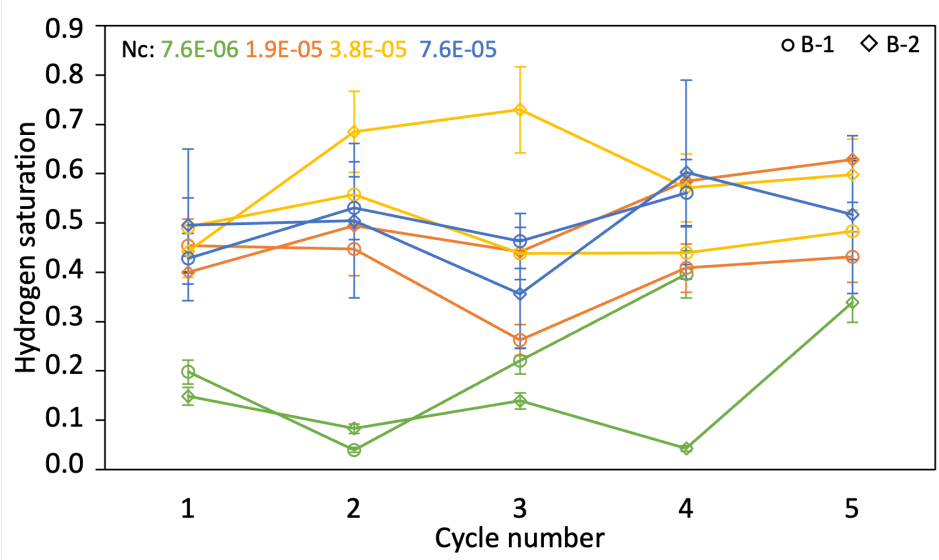

(a) All experiments

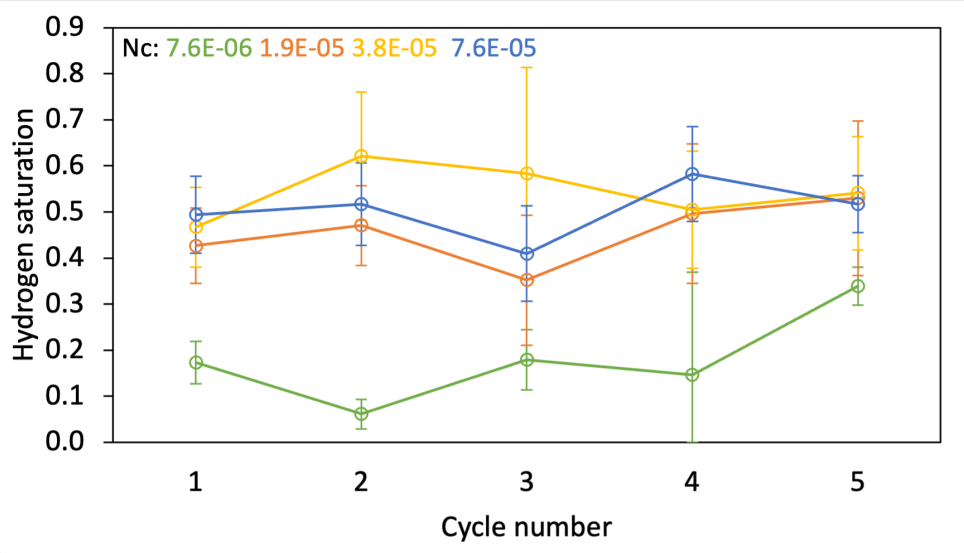

(b) Mean per capillary number

Figure 5.9: End-point gas saturation for each cycle for different capillary number. The indicator represents the experiment number while the colour represent the capillary number. (a) all experiments (b) Mean gas saturation for each each capillary number.

Even though the gas saturation was different for different experiments, a general trend could be observed for the mean of each capillary number. The mean gas saturation during the cycles for each capillary number is presented in Figure 5.9(b). Generally, there was a relationship between increased gas saturation for increasing capillary number. An expectation was $N_c = 3.80 \cdot 10^{-5}$, where the gas saturation was higher than the saturation for $N_c = 7.59 \cdot 10^{-5}$ during C2, C3 and C4. In addition, the highest capillary number had lower gas saturation than both $N_c = 3.80 \cdot 10^{-5}$ and $N_c = 1.90 \cdot 10^{-5}$ for C5. Note that the highest and lowest capillary number had only one measurements for C5 and were not averages. Based on the relationship between $N_c = 1.90 \cdot 10^{-5}$ and $N_c = 3.80 \cdot 10^{-5}$, an increase in gas saturation for C5 could be expected for the highest capillary number. The results shows a clear relationship between gas saturation and capillary number for capillary numbers lower than $N_c = 3.80 \cdot 10^{-5}$. For higher capillary

numbers, no clear relationship between gas saturation and capillary numbers was observed and could indicate that an increase in capillary numbers over the $N_c = 3.80 \cdot 10^{-5}$ does not necessarily increase the storage capacity of the medium. The results shows that the storage capacity is approximately stable or slightly increased for each cycle, where the largest increase in storage capacity was observed at low capillary numbers. The observation is also supported by the CDC presented in Figure 2.3.

The effect of capillary number and cyclic injection on storage capacity are also described by the modified CDCs for each cycle in Figure 5.10. The CDCs are the average gas saturation for each capillary number. The relationship between the irreducible water saturation and increased capillary was similar to the behaviour discussed during primary drainage in Figure 5.6 in Chapter 5.2 Primary drainage and imbibition. An increase in irreducible water saturation was only observed between $N_c = 3.80 \cdot 10^{-5}$ and $N_c = 7.59 \cdot 10^{-5}$ in C2 and C3. As previously discussed in Figure 5.7, local displacement through the FoV was observed during C3 for $N_C = 7.59 \cdot 10^{-}5$ and caused a gas saturation decrease during C3 drainage. Hypothetically, if the local displacements during C3 drainage had not happened, the end-point saturation would be close to the C3 maximum-saturation resulting in an irreducible water saturation to $S_w = 0.53$ for the cycle. An overlap in uncertainties was observed, and it could indicate that the irreducible water saturation increase with increasing cycles, as previously observed for primary drainage. Figure 5.10 shows that the water saturation was dependent on cycle number, but the relationship was not as clear as for capillary number. The water saturation approached a approximately constant water saturation during C5 indicating that a the maximum gas saturation will be reached independent on capillary number during injection of five cycles or more for $N_c >= 1.9 \cdot 10^{-6}$ and hysteresis effects was reduced for increasing cycles. Figure 5.5 and 5.10 shows the gas saturation relationship to capillary number was not that strong when gas was injected for more than five cycles. For future work, cyclic behaviour over more cycles could be valuable for UHS, preferably in a system not restricted by a limited FoV.

Pressure drop during cyclic injection

A pressure drop was observed at maximum hydrogen saturation during drainage for cyclic injection. The relationship between gas saturation and gas pressure is found in Figure 5.11. The gas pressure increased gradually while the gas saturation increased stepwise, and the gas pressure development was reproducible for each cycle in many of the experiments with different pressure drops. The maximum hydrogen saturation was reached for the drainage when the pressure dropped, indicating a steady-state hydrogen flow in established paths. Hysteresis was observed for experiment at the same capillary numbers where the pressure drop could vary. The end-point saturation for drainage was observed to increase slightly compared to the first cycle, with exceptions, and was observed for all capillary numbers. Figure 5.11 shows the largest pressure drops for the highest gas saturations and with increasing pressure drops with increasing cycle from C2 to C5, with a pressure drop at more than 2 bar for C4 and C5 for exp.B8-2. The pressure drops for the same capillary number in exp. B8-1 followed a similar trend with increasing pressure drops for each cycle. The largest pressure drop was observed in the last cycle (C4) at ∼2.5 bar. A pressure drop at $\sim$ 2 bar was also observed for $N_c = 3.80 \cdot 10^{-5}$. The pressure drop was dependent on capillary number and it was observed that the pressure drop was smaller for $N_c < 3.80 \cdot 10^{-5}$. However, the pressure drop for capillary number $N_c < 7.59 \cdot 10^{-5}$ was

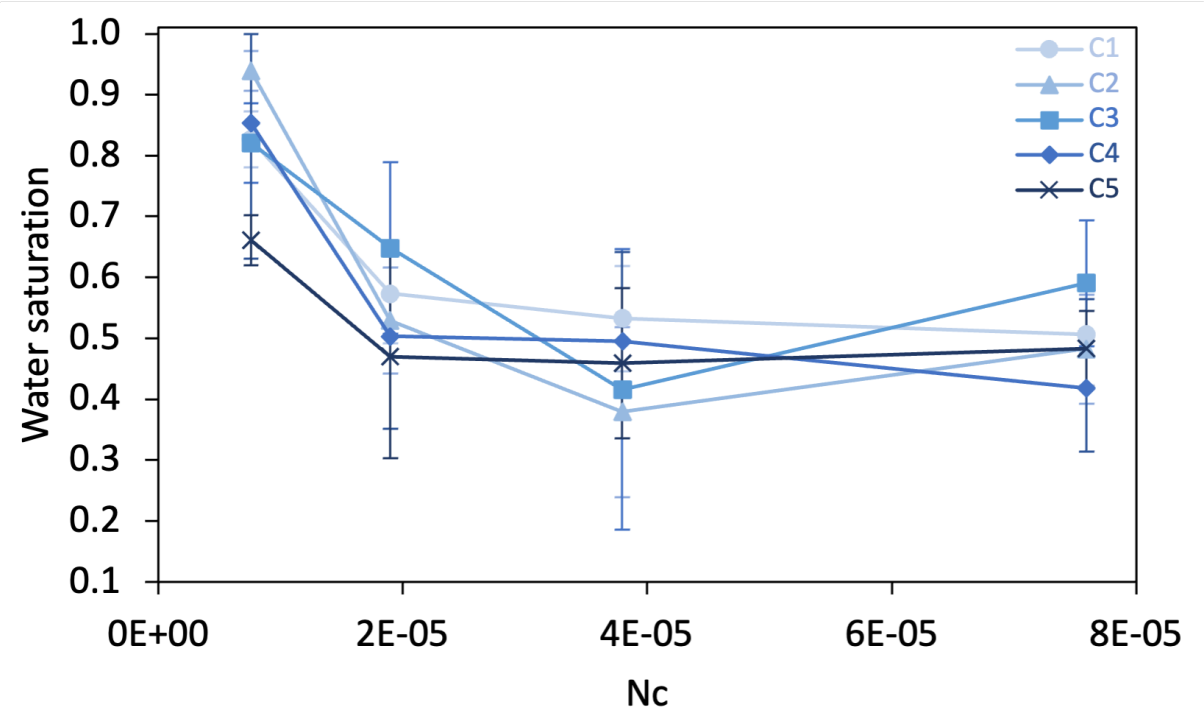

Figure 5.10: CDC for each cycle

relative constant for each drainage cycle, with only one exception in C4 for $N_c = 3.80 \cdot 10^{-5}$ (exp. B7-1). Hydrogen saturation decreased before gas entry in the FoV for C2 drainage after C1 imbibition due to a delay in drainage start caused by the FoV, as previously discussed. Hydrogen dissolution was observed at the beginning of drainage for from C2 to C5 and decreased with increasing gas pressure. Hydrogen dissolution relative to end-point imbibition in the previous cycle was observed to increase with increasing capillary number, and will be discussed in chapter 5.4.2 Hydrogen dissolution. The relationship between end-point gas saturation and pressure drop was also described for cyclic CO_2 injection [52].

The third cycle in Figure 5.11 in the figure had a fluctuating hydrogen saturation caused by local displacement through the FoV and lower end-point hydrogen saturation was achieved. The gas pressure peak was wider over more PV injected for C3 compared to the other cycles, indicating that the flow paths were not established, supported by observation of local gas displacement during C3 drainage. More PV injected could have increased the pressure drop and increased hydrogen saturation. The end-point gas pressure could indicate that the drainage was stopped before all gas flows were established.

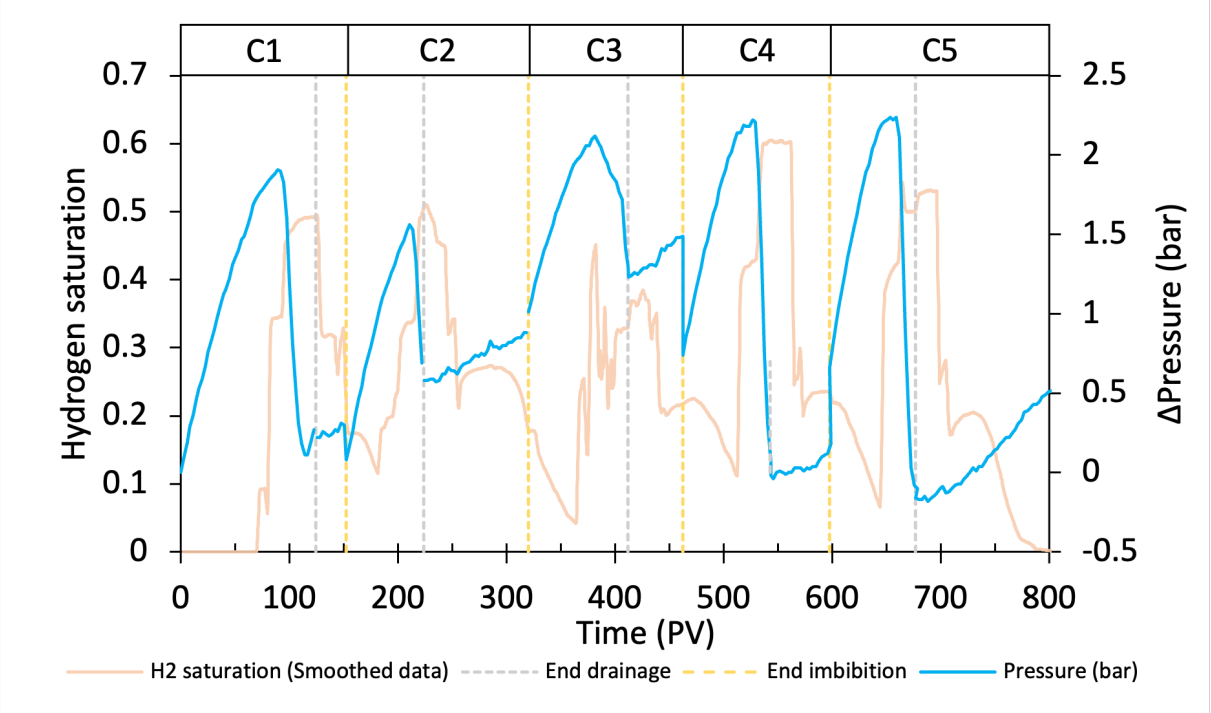

Figure 5.11: Pressure development during cyclic hydrogen injection in relation to hydrogen saturation for $N_c = 7.6 \cdot 10^{-5}$(exp. B8-2). The pressure is given in pressure difference (Δ Pressure) compared to the initial gas pressure at P = 41 bar.

5.4 Hydrogen loss

One of the main objectives for underground storage is to exploit variable renewable energy sources by converting excess energy to hydrogen when the demand is low. Similarly, the hydrogen could be extracted when the demand is high, and the gas recovery is an essential factor for an energy system's round-trip efficiency and profitability. Hydrogen loss to the to the formation will reduce the efficiency and should be kept at a minimum. This chapter will focus on hydrogen loss due to residual trapping and hydrogen dissolution in water, where the observations will be similar to the expected behaviour in an aquifer.

Similar recovery trends could be observed for cyclic injection (Table 5.6) and primary drainage and imbibition for exp. A1-A4. The highest recovery was observe for the lowest capillary number, with a recovery at ∼68% on average, when the negative recovery was excluded. Local gas displacement through the FoV during imbibition resulted in a higher end-point H_2 saturation during imbibition compared to the end-point during drainage. The lowest recovery was observed for $N_c = 3.80 \cdot 10^{-5}$ with an average at ∼ 19%. Both $N_c = 3.80 \cdot 10^{-5}$ and $N_c = 7.59 \cdot 10^{-5}$ had an average recovery at about 50%, and the similar recovery for the two capillary numbers indicated similar end-point H_2 saturations despite a lower capillary number. The pressure drop was also observed to be similar, indicating that $N_c > 3.80 \cdot 10^{-5}$ will have similar hydrogen displacement and trapping behaviour. An average gas recovery for all measurements per capillary number was about ∼50% for all capillary numbers expect $N_c = 3.80 \cdot 10^{-5}$. $N_c = 3.80 \cdot 10^{-5}$ had an average gas recovery at ∼ 20% caused by the high imbibition H_2 saturation. The recovery seemed to be independent on cycle, where small changes was observed from cycle to cycle. $N_c = 1.89 \cdot 10^{-5}$ was the only capillary number with increasing recovery with increasing cycles.

5.4.1 Residual trapping

The study of end-point imbibition saturations during cyclic injection gives insight in the residual trapping in the FoV where the imbibition gas saturations indicates the amount of immobile hydrogen and residual trapping in the pore structure. Figure 5.9 shows the end-point saturations for each cycle for different capillary numbers. The imbibition was stopped manually when disconnected gas was observed and preferably before dissolution had started. The experiments showed hysteresis in imbibition hydrogen saturation for each capillary number, but the difference could parlty be caused by visual determination of the imbibition end.As discussed in Chapter 5.3.1 Hydrogen displacement during cyclic injection, local displacement was observed in the FoV during imbibition and could also have affected the end-point gas saturations. The amount of local displacement during the cycles indicates that the gas would relatively easy be mobilised by global water and gas displacements.

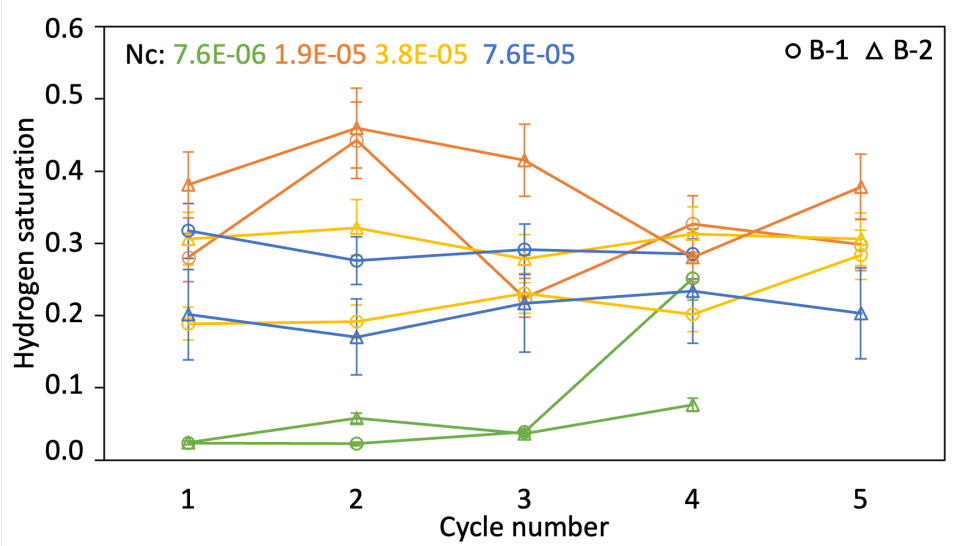

Figure 5.12: End-point imbibition gas saturation during cyclic injection at different capillary numbers. End-point gas saturation for each cycle for different capillary number. The indicator represents the experiment number while the colour represent the capillary number.

Disconnected hydrogen clusters and bubbles were analysed using the filtered microscope images produced from the image segmentation algorithm to study residual trapping during cycle injection. Because a limited FoV was used as study area, the imbibition gas saturation includes two parts, local residual gas and new gas from global events. The change in local residual gas with cycles was studied in this thesis. The end-point gas saturations used in this chapter correspond to the last image of the process and could therefore be slightly different to the mean gas saturations presented in Table 5.6. End-point filtered images were compared to quantify residual trapping by measuring the common area between drainage and imbibition for each cycle. End-point hydrogen saturation for drainage, imbibition and the residual gas present for each cycle are found in Table 5.7. Figure 5.13 shows the stepwise procedure for determining the common area for C1 for exp. B7-2. The filtered images of C1 drainage in Figure 5.13(a) and C1 imbibition in Figure 5.13(b) were combined in one image to find the common gas area over the cycle(Figure 5.13(c)). The common areas were calculated and a new layer of the intersection area was added to emphasise common areas of residual trapping, as shown in (Figure 5.13(d). The residual

gas algorithm is appended in Appendix B. The comparison for all cycles are presented in Figure 5.14.

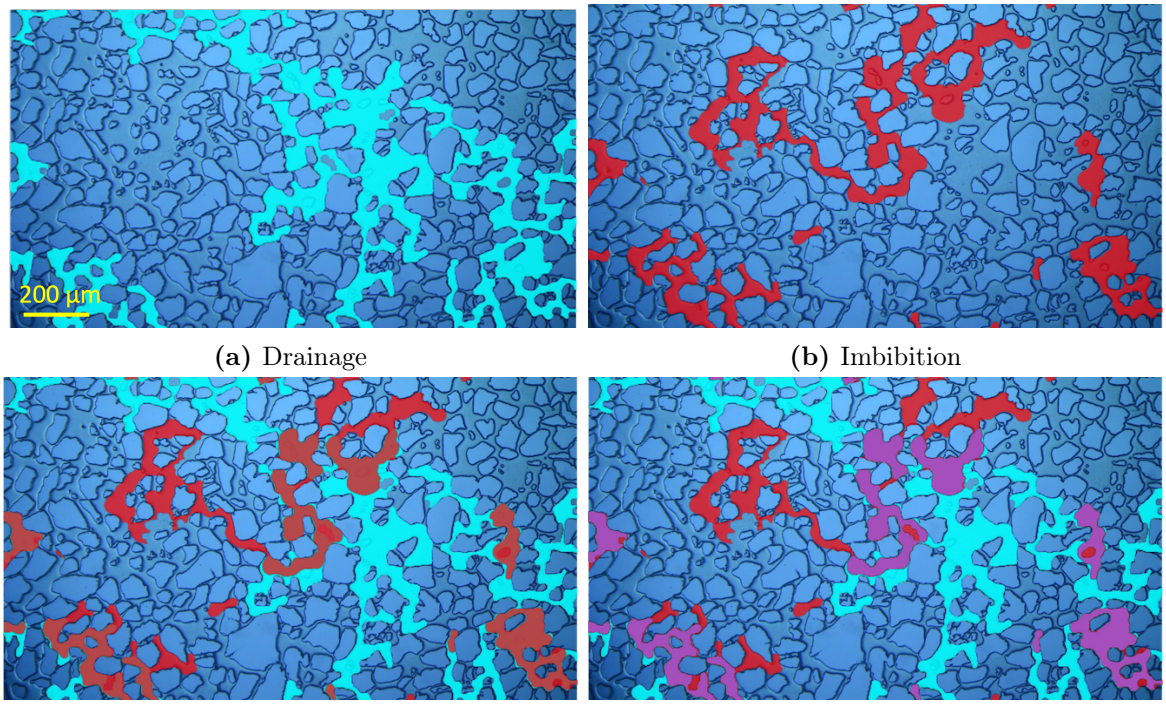

(a) Drainage **(b)** Imbibition

(c) Drainage + imbibition **(d)** Common area emphasised

Figure 5.13: Residual gas for C1 B7-2. The different steps to obtained the common area of drainage and imbibition for the are presented. The end-point hydrogen saturation during drainage (blue) (a) and imbibition (red) (b) are combined in (c). The intersection area, and trapped gas, are emphasised in purple in (d).

Table 5.7: End-point saturation, residual gas saturations and relationships between them. S_{gr}: residual gas(common area between drainage and imbibition). $S_{gr,all}$: residual gas present in all cycles (green area).

Exp.#	N_c ±0.02%	Cycle	S_{gdr0} ±12%	$S_{g,dr}$ ±12%	$S_{g,imb}$ ±12%	S_{gr}	$u(S_{gr})$	$S_{gr,all}$	$u(S_{gr,all})$	$\frac{S_{gr}}{S_{gr}}$	$u(\frac{S_{gr}}{S_{gr}})$	$\frac{S_{gr}}{S_{g,imb}}$	u($\frac{S_{gr}}{S_{g,imb}}$)	$\frac{S_{gr,all}}{S_{gr}}$	$u(\frac{S_{gr,all}}{S_{gr}})$	R_f[%]	$u(R_f)$[%]
B5-1	7.59279E-06	1	-	0.197	0.02264	0.020254	0.000005	-	-	0.103	0.002	0.9	0.1	-	-	89.46	10.74
		2	0.021	0.05641	0.02252	0.022142	0.000002	0.019945	0.000001	0.393	0.003	1.0	0.1	0.90	0.01	98.33	11.80
		3	0.021	0.218	0.03921	0.03661	0.00001	0.019267	0.000002	0.168	0.004	0.9	0.1	0.53	0.01	93.38	11.21
		4	0.040	0.395	0.25299	0.2168	0.0001	0.019246	0.00002	0.55	0.03	0.9	0.1	0.09	0.01	85.68	10.28
B5-2	7.59E-06	1	-	0.14881	0.02436	0.022027	0.000004	-	-	0.148	0.003	0.9	0.1	-	-	90.42	10.85
		2	0.014	0.08361	0.03617	0.035472	0.000004	0.013127	0.000001	0.424	0.005	1.0	0.1	0.370	0.004	98.08	11.77
		3	0.053	0.13921	0.05777	0.048526	0.000009	0.01268	0.00001	0.35	0.01	0.8	0.1	0.261	0.005	83.99	10.08
		4	0.040	0.04313	0.07645	0.035908	0.000004	0.009802	0.000001	0.83	0.01	0.47	0.06	0.273	0.003	46.97	5.64
		5	0.012	0.34017	-	-	-	-	-	-	-	-	-	-	-	0.00	0.00
B6-1	1.90E-05	1	-	0.45251	0.2793	0.1816	0.0001	-	-	0.40	0.03	0.65	0.08	-	-	65.02	7.80
		2	0.280	0.44746	0.49797	0.2568	0.0002	0.1256	0.0003	0.57	0.05	0.52	0.06	0.49	0.04	51.57	6.19
		3	0.029	0.2629	0.22022	0.1542	0.0001	0.0556	0.0001	0.59	0.02	0.70	0.08	0.36	0.01	70.04	8.40
		4	0.000	0.40679	0.32239	0.1149	0.0001	0.0489	0.0001	0.28	0.02	0.36	0.04	0.43	0.03	35.65	4.28
		5	0.046	0.42813	0.33957	0.1606	0.0001	0.0294	0.0003	0.38	0.02	0.47	0.06	0.18	0.01	47.28	5.67
B6-2	1.90E-05	1	-	0.40642	0.38725	0.1838	0.0001	-	-	0.45	0.03	0.47	0.06	-	-	47.47	5.70
		2	-	0.50259	0.46751	0.3011	0.0002	0.1175	0.0003	0.60	0.05	0.64	0.08	0.39	0.03	64.41	7.73
		3	-	0.44902	0.4219	0.2668	0.0002	0.0526	0.0004	0.59	0.04	0.63	0.08	0.20	0.01	63.24	7.59
		4	-	0.59474	0.28539	0.2718	0.0002	0.0338	0.0001	0.46	0.04	1.0	0.1	0.12	0.01	95.23	11.43
		5	-	0.63958	0.38418	0.2805	0.0003	0.0194	0.0001	0.44	0.04	0.73	0.09	0.07	0.01	73.02	8.76
B7-1	3.80E-05	1	-	0.56203	0.22012	0.1204	0.0001	-	-	0.21	0.02	0.55	0.07	-	-	54.70	6.56
		2	0.10	0.65222	0.22299	0.1787	0.0001	0.0622	0.0001	0.27	0.02	0.8	0.1	0.35	0.03	80.14	9.62
		3	0.0078	0.4899	0.26598	0.1294	0.0001	0.02422	0.00005	0.26	0.02	0.49	0.06	0.19	0.01	48.66	5.84
		4	0.015	0.49054	0.22845	0.1326	0.0001	0.0137	0.0002	0.27	0.02	0.58	0.07	0.10	0.01	58.03	6.96
		5	0.031	0.55713	0.32588	0.1978	0.0002	0.00721	0.00001	0.36	0.03	0.61	0.07	0.04	0.00	60.69	7.28
B7-2	3.80E-05	1	-	0.44361	0.29789	0.1731	0.0001	-	-	0.39	0.03	0.58	0.07	-	-	58.10	6.97
		2	0.17	0.64173	0.32877	0.2403	0.0002	0.0942	0.0002	0.37	0.03	0.73	0.09	0.39	0.03	73.10	8.77
		3	0.18	0.73407	0.28564	0.2269	0.0002	0.0384	0.0001	0.31	0.03	0.8	0.1	0.17	0.02	79.45	9.53
		4	0.21	0.56309	0.31889	0.2544	0.0002	0.0269	0.0001	0.45	0.04	0.8	0.1	0.11	0.01	79.76	9.57
		5	0.22	0.60059	0.28308	0.2245	0.0002	0.0206	0.0004	0.37	0.03	0.8	0.1	0.09	0.01	79.30	9.52
B8-1	7.59279E-05	1	-	0.42643	0.332	0.1872	0.0001	-	-	0.44	0.03	0.56	0.07	-	-	56.39	6.77
		2	0.0072	0.52671	0.27476	0.1830	0.0001	0.0809	0.0001	0.35	0.02	0.67	0.08	0.44	0.03	66.59	7.99
		3	0.0000	0.4641	0.28903	0.1795	0.0001	0.0625	0.0001	0.39	0.03	0.62	0.07	0.35	0.02	62.12	7.45
		4	0.0015	0.55381	0.28822	0.1657	0.0001	0.0425	0.0001	0.30	0.02	0.57	0.07	0.26	0.02	57.48	6.90
B8-2	7.59E-05	1	.	0.4917	0.18356	0.07819	0.00006	-	-	0.16	0.01	0.4	0.1	-	-	42.60	13.21
		2	0.11	0.50966	0.17524	0.08761	0.00007	0.027887	0.00003	0.17	0.01	0.5	0.2	0.32	0.03	49.99	15.50
		3	0.044	0.33534	0.21771	0.10119	0.00008	0.012313	0.00002	0.30	0.02	0.5	0.1	0.12	0.01	46.48	14.41
		4	0.11	0.60364	0.23846	0.1602	0.0002	0.007639	0.00002	0.27	0.03	0.7	0.2	0.05	0.00	67.19	20.83
		5	0.057	0.50793	0.20106	0.10034	0.00009	0.006418	0.00023	0.20	0.02	0.5	0.2	0.06	0.01	49.91	15.47

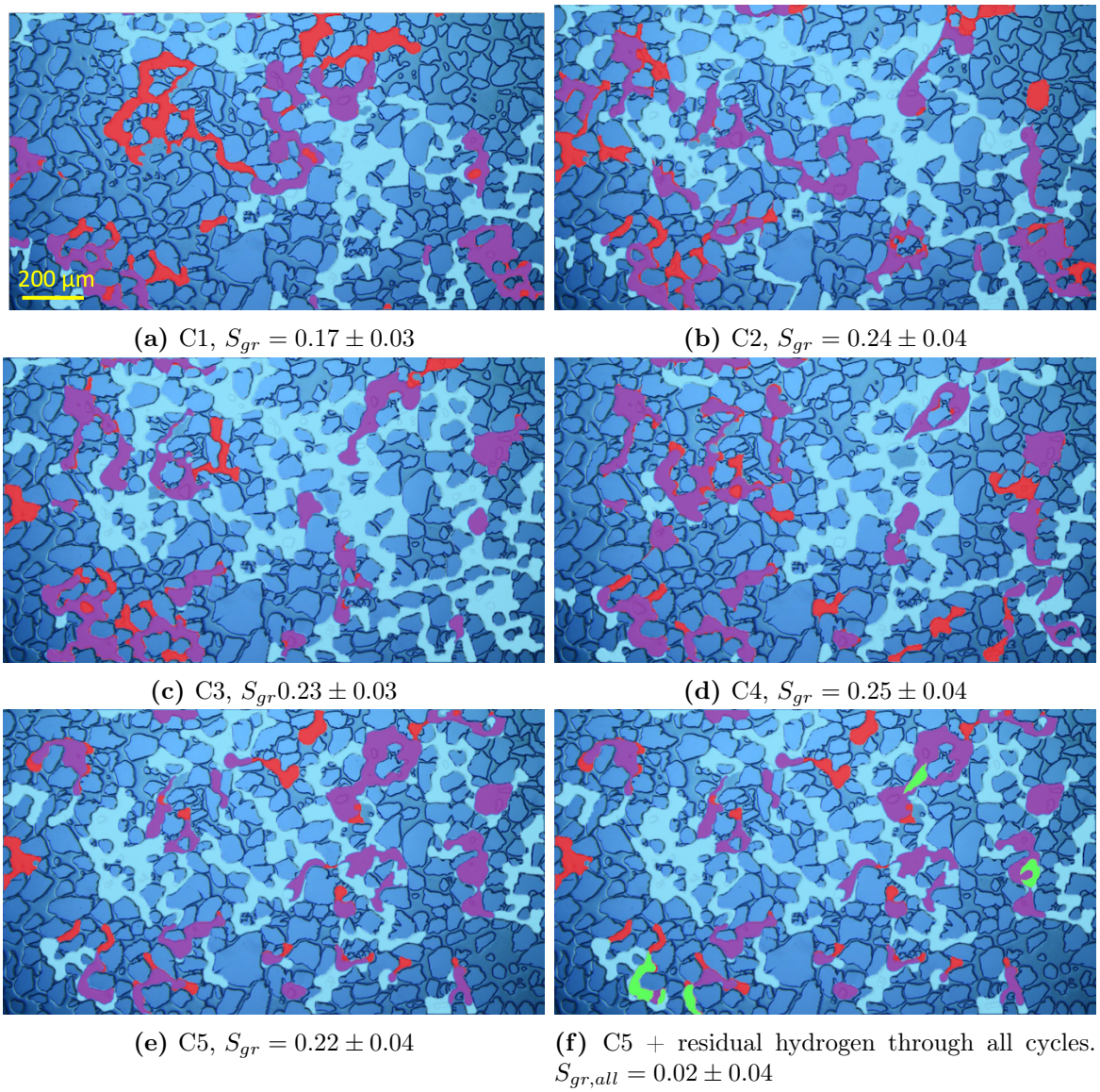

(a) C1, $S_{gr} = 0.17 \pm 0.03$

(b) C2, $S_{gr} = 0.24 \pm 0.04$

(c) C3, $S_{gr}0.23 \pm 0.03$

(d) C4, $S_{gr} = 0.25 \pm 0.04$

(e) C5, $S_{gr} = 0.22 \pm 0.04$

(f) C5 + residual hydrogen through all cycles. $S_{gr,all} = 0.02 \pm 0.04$

Figure 5.14: Residual hydrogen for cyclic injection C1-C5 for $N_c = 3.8{\cdot}10^{-5}$ (Exp. B7-2). Blue: drainage, red: imbibition, residual gas(intersection area): purple, green: residual gas through all cycles

The residual gas is disconnected hydrogen bubbles and clusters at end-point imbibition and are considered lost to the formation. Figure 5.14 shows the residual gas in C1 to C5 for $N_c = 3.8 \cdot 10^{-5}$(exp. B7-2). Local displacement was observed during the cycles, and 31 to 45% of the drainage gas saturation was residual trapped. 58 to 80% of the imbibition hydrogen saturation was also present during drainage, where the remaining percentage consisted of gas displaced to new locations due to local displacement. Note that residual gas coloured in purple was not necessarily immobile during the cycle, but gas is present in the pore space at end-point drainage and end-point imbibition. The green area in Figure 5.14(f) marks residual gas present in all cycles. The size of the green area was controlled by the smallest common areas for the cycles. The residual gas was compared to the residual gas in the previous cycle. It was observed that the residual gas saturation (S_gr) was reduced from C2 to C3 in the areas marked in red squares, resulting in a decrease in the residual gas present in all cycles, S_gr, all. S_gr, all was expected to be higher if C3 was e excluded. Residual hydrogen relative to end-point imbibition saturation

was highest for $N_c = 7.59 \cdot 10^{-6}$ with relative residual hydrogen between 47 and 98% of the end-point imbibition saturation. In contrary to higher capillary number, gas was not locally displaced through the FoV, and the same areas were saturated during the cycles, with few exception. It was observed that the gas flow could not penetrate the smallest pores to enter the largest pore space in the centre of the FoV for the lowest capillary number due to the low injection rate and pore pressure.

The amount of immobilised hydrogen during cyclic injection will affect the gas recovery for the storage facility and must be accounted for in the study of energy efficiency and hydrogen loss. The relationship between residual gas saturation and end-point imbibition and drainage hydrogen saturation is presented in Figure 5.15. The coefficient of determination R-squared assesses how strong the linear relationship is between the two variables, where a value of 1.0 is a perfect fit. $R^2 = 0.70$ indicated a strong, positive correlation of the residual gas and imbibition saturation (5.15(a)), which means that an increase in residual gas is expected with increased end-point gas saturation during imbibition. The relative trapping was between 34 to 98% of the end-point imbibition saturation for all experiments, where the average relative trapping was lowest for the highest capillary number. The lower relative trapping compared to imbibition saturation was supported by the observation of a higher frequency of local displacement in the FoV for higher capillary numbers. The hydrogen loss relative to the stored gas is of highest importance for a storage unit. The relationship between residual gas and end-point drainage hydrogen saturation had a moderate, positive correlation at $R^2 = 0.57$ in Figure 5.15(b), which could indicate that an increase storage volume will have a larger hydrogen loss to the formation when capillary number is not considered. The moderate correlation also indicates that more of the small pores were gas filled during drainage increasing hydrogen saturations before the gas was snapped off or by-passed by the waterfront during imbibition.

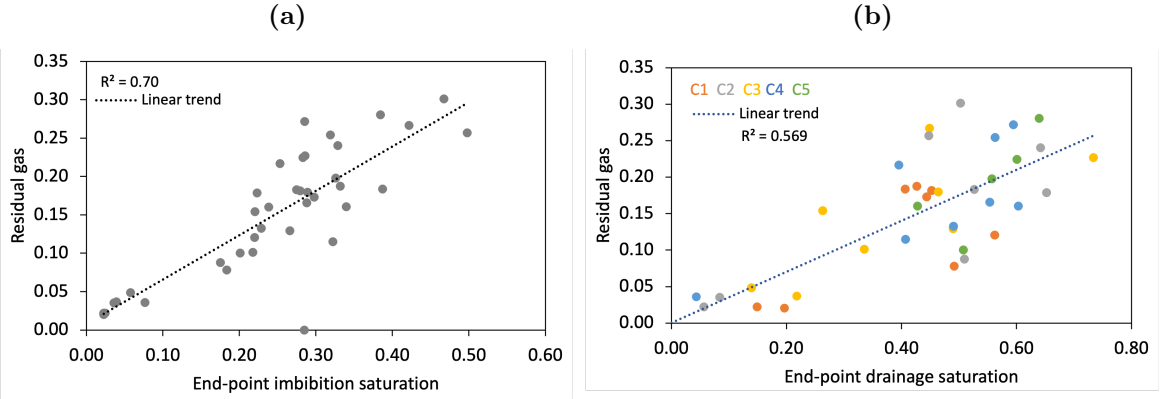

Figure 5.15: Residual gas relationship. (a) A strong, positive correlation was observed between residual gas and end-point imbibition saturation at $R^2 = 0.7962$. (b) A moderate, positive correlation was observed between residual gas and end-point drainage saturation at $R^2 = 0.5501$.

The relative residual trapping to drainage gas saturation tended to decrease with increasing capillary number by Figure 5.16. The residual gas was observed to be moderate, positive correlated to end-point drainage hydrogen saturation. The highest percent of residual gas relative to end-point drainage saturation was observed for low capillary numbers, but the highest mean residual gas saturation was observed for $N_c = 3.80 \cdot 10^{-5}$. A high saturation was reached for the capillary number during drainage despite being a low capillary number with lower gas pressure. The high share of residual trapping could be

caused by the gas displacement mechanisms during imbibition. Local gas displacement through the FoV was observed at B6-1 during C2 imbibition where the start-point imbibition saturation was almost identical to the end-point drainage saturation but with different gas distribution in than the previous cycle. The capillary trapping when gas was displaced during imbibition could also have caused the high residual gas saturation. The high drainage hydrogen saturation for several cycles at $N_c = 3.80 \cdot 10^{-5}$ showed that the gas was able to enter the pore network during drainage, but the residual trapping could indicate the gas was restricted by narrow pore throats to be displaced during imbibition. Snap-off and disconnection occurred at a higher gas saturation during local gas displacement compared to higher capillary numbers at similar gas saturations. It could also seem from Figure 5.16) that the residual gas relative to drainage saturation could increased by increasing cycles.

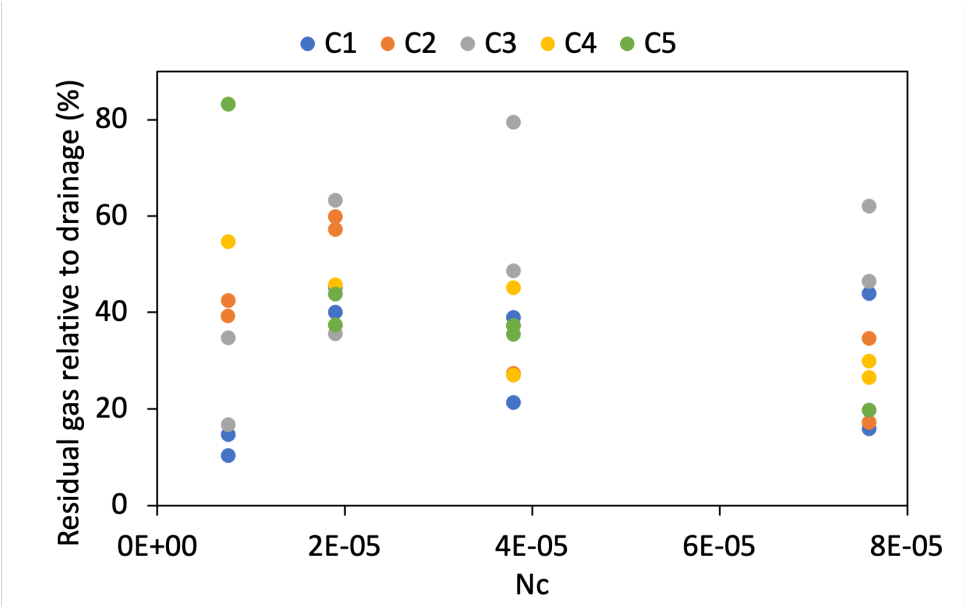

Figure 5.16: Residual gas relative to drainage(%) compared to capillary number.

The effect of cyclic injection and capillary number on relative trapping could be difficult to identify by one factor. Multi phase processes are dependent on several factors where trends and relationships could not be identified by a single parameter. Hysteresis caused by path dependency and saturation history resulted in different values for for at similar conditions. However, Figure 5.15(b) indicates that it is a relationship between increased residual trapping and increased drainage gas saturation for C5, while a decrease in residual gas was observed by increasing capillary number for C5 in Figure 5.16. Relative residual trapping was also observed to decrease with increasing capillary number on average, but no clear effect of cyclic injection and capillary number could be concluded. The relationship between residual trapping and initial saturation has also been studied for cyclic injection of supercritical CO_2 ($scCO_2$) and water over three cycles by Herring et.al.[7]. The experiments showed that increased trapping of $scCO_2$ with increasing cycle, but the magnitudes in increase was exhibited a hysteresis dependency. The corresponding relationship in Figure 5.15(b) does not show a similar clear trend for residual trapping over several cycles independent on capillary number.

5.4.2 Hydrogen dissolution

Gas dissolution in water is one of the trapping mechanisms occurring in a geological formation, and will decrease the recovery for UHS. The amount of hydrogen dissolved during pressure build up during drainage is quantified in this section. A gas dissolution occurred during the pressure build-up before local gas displacement was observed and the amount of dissolved gas is the difference between end-point imbibition saturation and the saturation when local gas displacement was observed. A minimum hydrogen saturation point was observed, $S_{g,d0}$, and was the initial drainage saturation locally. The minimum point was observed in Figure 5.7 and can be found in Table 5.7. If the imbibition was stopped after dissolution (as observed in C2 for Figure 5.7), a lower minimum point would be expected. Figure 5.17 present the dissolution of hydrogen during drainage relative to end-point imbibition saturation by capillary number, where the curve shows an increase in dissolution on average for increasing capillary numbers. The increase in dissolution might be related to the pressure increase with increasing capillary numbers. The range of values was narrower for higher capillary numbers. Note that the dissolution for $N_c = 1.9 \cdot 10^{-5}$ was only calculated based on one experiment and more measurements could have affected the mean value. Both discussion of Figure 5.11 and dissolution of hydrogen support previous work where a hydrogen cluster dissolved at a faster rate for high capillary numbers [40].

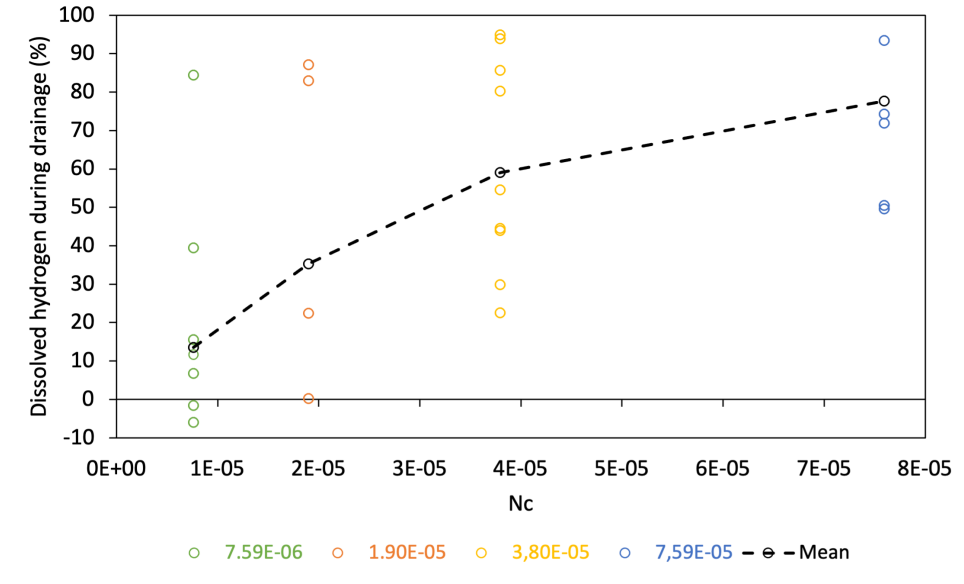

Figure 5.17: Hydrogen dissolution relative to imbibition saturation for different capillary numbers before gas breakthrough during drainage. "Mean" is the mean of all values for each capillary number. The increase might be related to the high pressure increase at high capillary numbers. Only one experiment were included for $N_c = 1.9 \cdot 10^{-5}$.

Experiments have shown that residual trapping occurs over several cycles and that dissolution also reduce the hydrogen recovery. Hydrogen dissolution was observed when the pressure increased, but are also closely connected to both hydrogen solubility in water and salinity. For future work, the water could be pre-saturated with hydrogen to reduce hydrogen dissolution when pressure increases during drainage. Less hydrogen dissolution could be valuable to study the reconnection of larger hydrogen clusters and smaller bubbles. The larger cluster decreased to a smaller size in the present setup, while smaller

bubbles could fully dissolved. Saline water should be used to study more realistic reservoir behaviour in future experiments to study the effect of salinity in a hydrogen-brine system. The cushion gas used under UHS should have lower solubility in water to make sure that the cushion gas does not dissolve in water.

5.5 Contact angles

Wettability will affect fluid flow and is important for hydrogen distribution and displacement. Static contact angles was measured during primary drainage and imbibition for all experiment.

Contact angles were measured in pore channels with pore diameter from 27 to 150µm, where the highest frequency of measurements was observed between 20 to 50 µm. A large span of contact angles per N_c are observed by Figure 5.18. The top figure present the mean contact angles for each capillary number, where the uncertainty is the combined uncertainty based on standard deviation from the mean of contact angles per experiment and standard deviation per contact angle measurement. The uncertainty bars in the top figure span over a range cover all data points in the bottom figure. Mean static contact angles between drainage and imbibition was observed in the same range. The measured contact angles varied from 19 to 72°, with the highest data point density between 19 to 60°. The measured angles was similar to contact angles 17-56° in an identical hydrogen-water-micromodel system, as well as contact angles at 22-45° in hydrogen-water-sandstone systems [57],[58].

Contact angles at low capillary numbers was measured at pore diameters between 30 and 90 µm, with only one exception. The angle distribution by pore size was a direct result of hydrogen saturation and distribution. Figure 5.5 showed that the hydrogen was distributed at the edges of the FoV low capillary numbers. It was observed that the gas front was blocked by small pore channels that could lead to the centre of the FoV where more space was available.

$N_c = 1.9 \cdot 10^{-5}$ have a deviation from the mean at ± 26° and 25° for drainage and imbibition, respectively. The higher uncertainty could be correlated with saturation distribution and capillary pressure. Contact angles for $N_c = 1.9 \cdot 10^{-5}$ were measured in pores with diameter from 30 to 90 µm by Figure 5.19, indicating that the gas fronts were stopped by capillary pressure in narrow pore throats. The large variation is also caused by the difference between minimum and maximum angles for the experiment: a total angle difference at 35° was observed during Exp.B5-1 imbibition. The mean standard deviation for each measurement at 6° was also above the calculated average of all measurements at 4°, and could be a result of image resolution. Uncertainty measurements were also dependent on image resolution, and not all angles were possible to measure due to thick lines at the interfaces. As previously discussed, the image quality and brightness was lower at the bottom edge for each side of the FoV, and could have affected the measuring precision. The raw images from the experiment had a bad focus and a low saturation distribution near the edges, where both elements could have caused an increased uncertainty compared to other measurements.

The systematic uncertainty in the manually measurement of angle was addressed by repeating each measuring point 5 times. However, the systematic uncertainty of the method is subjective due to measurement based on visual observation. Grain structure could cause

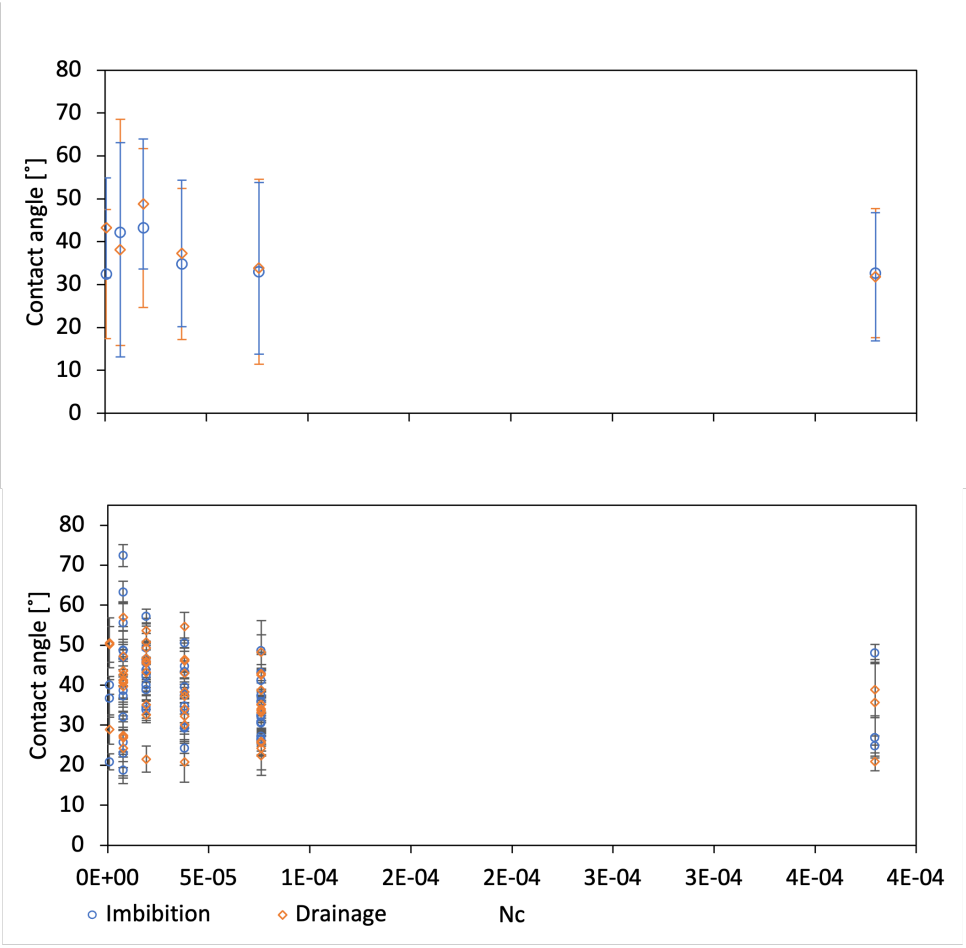

Figure 5.18: Static contact angles by capillary number. The top figure shows the mean contact angles with uncertainties for each Nc.

uncertainty where the contact point between grain and hydrogen interface could be hard to identify due to grain surface, grain shadows and hydrogen-water concavities. Another source of uncertainty is the random hydrogen distribution which hindered measurements of angles in the same pores. These uncertainties are also addressed by Lysyy et al. [41]. In addition, contact angles could not be measured in the smallest pores due to the thickness of the grain-hydrogen-water interfaces. Despite uncertainties with the method, the results gives valuable data for wettability and relative permeability estimations. The method also enable the study of static and dynamic contact angles in the pore structure and not only indirect measurements.[41]. Cyclic injection of CO_2 have showed that wettability could be alternated when CO_2 was injected over several cycles. For future work, contact angles could be measured over cycles to study the effect on cyclic hydrogen injection [52].

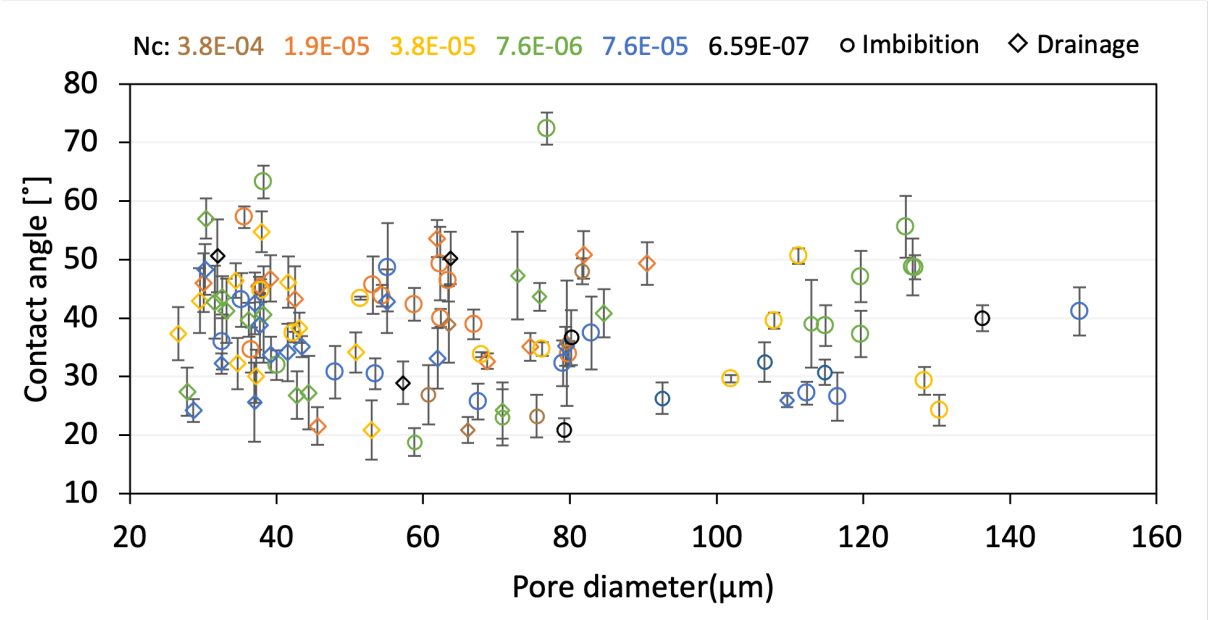

Figure 5.19: Measured contact angles by pore diameter(µ) for different capillary numbers.

Chapter 6

Conclusion

Micromodel experiments have been performed to study pore-scale mechanisms of hydrogen flow during primary drainage, imbibition and cyclic injection, where an image segmentation algorithm was developed to study gas displacement and gas saturations for different capillary numbers. The relationship between H2 saturation, capillary number and residual trapping have been analysed. Static contact angles were also measured to study potential wettability changes for capillary numbers. Key results based on the work in this thesis are presented in the list below:

Image segmentation algorithm

- water accumulation in the hydrogen flow affected the uncertainty of the algorithm where hydrogen with water accumulation had darker colour and was ignored. The amount of water accumulation was highest at low PV injected and if rapid changes in gas distribution occurred, increasing the uncertainty of the image segmentation algorithm.
- The image segmentation algorithm was precise when the microscope was stable without movements of the FoV. Based on the sensitivity analysis of a selection of filtered images from different experiments, the relative uncertainty of H2 saturation was on average 12
- No trend between relative uncertainty and H2 saturation or capillary number was observed. The main factors affecting the relative uncertainty was water accumulation and light source distribution.

Primary drainage and imbibition

- The hydrogen saturation increased for increasing capillary numbers during drainage in the water-saturated micromodel.
- The hydrogen saturation decreased until it stabilised at the residual gas saturation. The residual gas was present as immobile, discontinuous bubbles and clusters, representing the amount of gas that cannot be recovered. The residual gas was dissolved when bypassed of water.
- Local displacement caused by global events resulted in fluctuating hydrogen saturation during both drainage and imbibition.

- The relative recovery seems to increase with capillary number, with the exception of $N_c = 7.59 \cdot 10^{-7}$, which was the highest recovery. However, the recovery was connected to less residual trapping due to gas distribution at the edges of the FoV and did not penetrate narrow pore throats.
- The image segmentation algorithm was not suited for experiments where the microscope was moved during the experimental period. Changes in FoV caused change in H2 saturation in the experimental data and increased noise, with higher probability of FoV change when several videos were used during the experiment.
- An analysis indicated a dependency between H2 saturation and FoV position, where the distance from the water and hydrogen inlets likely affected the H2 saturation in the FoV.

Cyclic injection of hydrogen

- A decrease in hydrogen saturation was observed during drainage when the micromodel was gas saturated caused by FoV effects: the hydrogen in the FoV experienced a prolonged imbibition before the gas front entered the FoV.
- A stable or increased end-point drainage H2 saturation with increasing cycles was observed for most experiments and capillary number.
- The gas saturation dependency on capillary number is weaker when gas is injected over five or more cycles. A stronger correlation between capillary number and increased gas saturation was observed for primary drainage compared to the drainage in the forth cycle. Results indicate that $N_c >= 3.80 \cdot 10^{-5}$ would approach a stable end-point H2 saturation during drainage. Hence, the storage capacity of cyclic injection could be identified.
- The gas pressure increased before gas entry in the FoV, increasing the gas saturation stepwise. A pressure decrease was observed at the maximum hydrogen saturation, indicating that the gas front had passed and flow paths were established.
- A strong, positive correlation was observed between residual gas and end-point imbibition gas saturation.
- A moderate, positive correlation between residual gas saturation and end-point drainage gas saturation was observed, indicating that more gas will be residual trapped for higher storage volumes.
- The relative residual trapping (normalised to drainage H_2 saturations) tends to decrease with increasing capillary number.
- Results could indicate a relationship between increased residual gas relative to drainage gas saturation with increasing cycles, but no clear trend was observed.
- Hydrogen dissolution was observed as a consequence of local imbibition events during drainage when the micromodel was gas saturated, similar to what was observed during experiments for imbibition. Hydrogen was dissolved when the gas pressure increased. An increase in dissolution was observed for increasing capillary numbers caused by the increased pore pressure.

Static contact angles

- The measured contact angles varied from 19 to 71° during primary drainage and imbibition for all experiments measured in pores with pore diameter $30 - 150\mu m$, confirming the water-wet wettability of the micromodel.

Chapter 7

Future work

The experiments is a part of the UHS project HyPE, a collaboration between NORCE and UiB. The result leads to the identification of reservoir storage capacity, potential losses and wettability changes during hydrogen storage in aquifers, but further experiments must be performed to understand the hydrogen behaviour in UHS. The list below gives suggestions for future work:

- use saline water instead of distilled water to have a more realistic behaviour.
- Investigation of the effect of saline water on H_2 dissolution.
- Pre-saturated water with hydrogen for better study of the reconnection of larger hydrogen bubbles.
- Cyclic injection over more than five cycles.
- Hydrogen mixed CH_4 and other gases typically used as cushion gas.
- Use of microbial organisms to study microbial effects and get closer to a reservoir environment.
- Measurement of advancing and receding contact angles to investigate wettability alternation for cyclic injection.
- Use experimental data from micromodel and core experiments for detailed UHS modelling.
- The use of fluorescent tracers for water and/or hydrogen to study flow patterns and relative permeabilities.

Suggestions for future work based on the method:

- A FoV of the entire micromodel will give a better understanding of the mechanisms and gas displacement. Different gas saturations was observed in different FoV positions.
- Adjust experimental setup for better image processing conditions by using a uniform light source and increase stability of the setup to reduce unwanted movements of the microscope.

- Further development of image segmentation algorithm. The algorithm is sensitive to light distribution, colour change and small movements of the FoV.
- Connect a pressure transducer to the micromodel for continuously observation of the pressure in the micromodel, not only in the pumps.
- The use of more sensitive pumps will reduce uncertainties and increase sensitivity to rapid change in the system, increasing the efficiency of the experiments.
- Accumulator to measure the retracted gas from the micromodel.
- Improved procedure for contact angles in pore channels with lower uncertainties.

Bibliography

[1] DNV, "ENERGY TRANSITION NORWAY 2021 A national forecast to 2050," tech. rep.

[2] D. Zivar, S. Kumar, and J. Foroozesh, "Underground hydrogen storage: A comprehensive review," *International Journal of Hydrogen Energy*, vol. 46, pp. 23436–23462, 7 2021.

[3] J. G. Speight, "5 - Recovery, storage, and transportation," in *Natural Gas (Second Edition)* (J. G. Speight, ed.), pp. 149–186, Boston: Gulf Professional Publishing, second edition ed., 2019.

[4] J. G. Speight, "CHAPTER 4 - Recovery, Storage, and Transportation," in *Natural Gas* (J. G. Speight, ed.), pp. 87–111, Gulf Publishing Company, 2007.

[5] R. Tarkowski, "Underground hydrogen storage: Characteristics and prospects," *Renewable and Sustainable Energy Reviews*, vol. 105, no. February 2017, pp. 86–94, 2019.

[6] Norwegian Petroleum Directorate, "4.2.2 Abandoned hydrocarbon fields." (Accessed 30/05/22) https://www.npd.no/en/facts/publications/co2-atlases/co2-atlas-for-the-norwegian-continental-shelf/4-the-norwegian-north-sea/4.2-storage-options-in-the-north-sea/4.2.2-abandoned-hydrocarbon-fields/

[7] A. L. Herring, L. Andersson, and D. Wildenschild, "Enhancing residual trapping of supercritical CO2 via cyclic injections," *Geophysical Research Letters*, vol. 43, pp. 9677–9685, 9 2016.

[8] H. Ahn, S. O. Kim, M. Lee, and S. Wang, "Migration and Residual Trapping of Immiscible Fluids during Cyclic Injection: Pore-Scale Observation and Quantitative Analysis," *Geofluids*, vol. 2020, 2020.

[9] S. H. Barghi, T. T. Tsotsis, and M. Sahimi, "Chemisorption, physisorption and hysteresis during hydrogen storage in carbon nanotubes," *International Journal of Hydrogen Energy*, vol. 39, pp. 1390–1397, 1 2014.

[10] IEA, "Net Zero by 2050 - A Roadmap for the Global Energy Sector," tech. rep., International Energy Agency, 5 2021.

[11] NVE, "Kapasiteten på solkraftproduksjonen økte jevnt i 2021," 4 2022. (Accessed 21/05/2022) https://www.nve.no/nytt-fra-nve/nyheter-energi/kapasiteten-paa-solkraftproduksjonen-oekte-jevnt-i-2021/

[12] . IEA, Offshore Wind Outlook, "Offshore Wind Outlook 2019: World Energy Outlook Special Report," *International Energy Association*, 2019.

[13] DNV GL, "Energy Transition Outlook 2020 - A global and regional forecast to 2050," *Dnv Gl Energy Transition Outlook*, p. 306, 2020.

[14] Hydrogen Europe, "Hydrogen 2030 : The Blueprint," tech. rep., Hydrogen Europe, Brussel, 2020.

[15] SINTEF, "Hva er egentlig grått, grønt, blått og turkis hydrogen?." (Accecced 21/05/2022) https://www.sintef.no/siste-nytt/2020/hva-er-egentlig-gra-gronn-bla-og-turkis-hydrogen/

[16] BP, "Energy Outlook 2020 edition," *BP Energy Outlook 2030, Statistical Review. London: British Petroleum.*, p. 81, 2020.

[17] Bp, "bp Energy Outlook 2022," tech. rep., 2022.

[18] Lloyds Register, "Hydrogen and Ammonia Infrastructure," tech. rep., 5 2020.

[19] D. Li, Q. Zhang, Q. Ma, and S. Shen, "Comparison of explosion characteristics between hydrogen/air and methane/air at the stoichiometric concentrations," *International Journal of Hydrogen Energy*, vol. 40, pp. 8761–8768, 7 2015.

[20] DTU, "Global Wind Atlas.", https://globalwindatlas.info/ (Accessed: 22/05/2022)

[21] IEA, "The Future of Hydrogen," tech. rep., 2019.

[22] A. Boretti, S. Castelletto, W. Al-Kouz, and J. Nayfeh, "Capacity factors of solar photovoltaic energy facilities in California, annual mean and variability," in *E3S Web of Conferences*, vol. 181, EDP Sciences, 7 2020.

[23] P. Bajpai and D. V. Tekumalla, "Chapter 12 - Techno-economic performance evaluation among different solar photovoltaic system configurations," in *Design, Analysis, and Applications of Renewable Energy Systems* (A. T. Azar and N. A. Kamal, eds.), Advances in Nonlinear Dynamics and Chaos (ANDC), pp. 301–319, Academic Press, 2021.

[24] Greenstat, Æge Energy/aabø Powerconsulting, H. p. Vestlandet, and Universitetet i Bergen, "Optimal utnyttelse av energi fra havvind i Sørlige Nordsjø II Offshore H2-produksjon og kabel til land," tech. rep., Greenstat, Aabø Power Consulting, Høgskulen på Vestlandet, Universitetet i Bergen, Bergen, 2021.

[25] M. Kayfeci and A. Keçebaş, "Hydrogen storage," in *Solar Hydrogen Production: Processes, Systems and Technologies*, p. 26, Elsevier Science & Technology, 2019.

[26] C. R. Matos, J. F. Carneiro, and P. P. Silva, "Overview of Large-Scale Underground Energy Storage Technologies for Integration of Renewable Energies and Criteria for Reservoir Identification," *Journal of Energy Storage*, vol. 21, no. November 2018, pp. 241–258, 2019.

[27] F. Crotogino, "Larger Scale Hydrogen Storage," in *Storing Energy: With Special Reference to Renewable Energy Sources* (T. M. Letcher, R. Law, and R. David, eds.), ch. 20, pp. 411–429, 2016.

[28] F. Feldmann, B. Hagemann, L. Ganzer, and M. Panfilov, "Numerical simulation of hydrodynamic and gas mixing processes in underground hydrogen storages," *Environmental Earth Sciences*, 2016.

[29] F. Buzek, V. Onderka, P. Vancurat, and I. Wolf, "Carbon isotope study of methane production in a town gas storage reservoir," tech. rep.

[30] D. R. Simbeck, "CO2 capture and storage-the essential bridge to the hydrogen economy," *Energy*, vol. 29, no. 9-10, pp. 1633–1641, 2004.

[31] S. Flesch, D. Pudlo, D. Albrecht, A. Jacob, and F. Enzmann, "Hydrogen underground storage-Petrographic and petrophysical variations in reservoir sandstones from laboratory experiments under simulated reservoir conditions," *International Journal of Hydrogen Energy*, 2018.

[32] S. v. Gessel, A.-G. Bader, A. Bialkowski, L. Beccaletto, and E. Begemann, "ESTMAP Energy Storage Mapping and Planning ESTMAP Energy Storage Data Collection Report," tech. rep., 2016.

[33] S. H. Barghi, T. T. Tsotsis, and M. Sahimi, "Chemisorption, physisorption and hysteresis during hydrogen storage in carbon nanotubes," *International Journal of Hydrogen Energy*, vol. 39, pp. 1390–1397, 1 2014.

[34] F. F. Craig, "The reservoir engineering aspects of waterflooding," 1971.

[35] W. Anderson, "Wettability literature Survey - Part 6: The effects of wettability on waterflooding," *Society of Petroleum Engineers*, 1986.

[36] A. Saeedi, R. Rezaee, B. Evans, and B. Clennell, "Multiphase flow behaviour during CO2 geo-sequestration: Emphasis on the effect of cyclic CO2-brine flooding," *Journal of Petroleum Science and Engineering*, vol. 79, pp. 65–85, 11 2011.

[37] W. G. Anderson, "Part 4: Effects of Wettability on Capillary Pressure," 1987.

[38] K. Singh, H. Menke, M. Andrew, Q. Lin, C. Rau, M. J. Blunt, and B. Bijeljic, "Dynamics of snap-off and pore-filling events during two-phase fluid flow in permeable media," *Scientific Reports*, vol. 7, no. 1, 2017.

[39] M. Jafari and J. Jung, "Direct measurement of static and dynamic contact angles using a random micromodel considering geological CO2 sequestration," *Sustainability (Switzerland)*, vol. 9, 12 2017.

[40] P.-H. K. V. D. Hart, *A Pore-Scale Study of Underground Hydrogen Storage in Porous Media*. PhD thesis, University of Bergen, 2021.

[41] M. Lysyy, G. Ersland, and M. Fernø, "Pore-scale dynamics for underground porous media hydrogen storage," *Advances in Water Resources*, vol. 163, no. December 2021, p. 104167, 2022.

[42] K. Singh, T. Bultreys, A. Q. Raeini, M. Shams, and M. J. Blunt, "New type of pore-snap-off and displacement correlations in imbibition," *Journal of Colloid and Interface Science*, vol. 609, 2022.

[43] L. W. Lake, *Enhanced Oil Recovery*. 1 ed., 1989.

[44] Equinor, "Northern Lights.", https://www.equinor.com/energy/northern-lights (Accessed 31/05/2022)

[45] F. Feldmann, B. Hagemann, L. Ganzer, and M. Panfilov, "Numerical simulation of hydrodynamic and gas mixing processes in underground hydrogen storages," *Environmental Earth Sciences*, 2016.

[46] M. Lysyy, M. Fernø, and G. Ersland, "Seasonal hydrogen storage in a depleted oil and gas field," *International Journal of Hydrogen Energy*, vol. 46, pp. 25160–25174, 7 2021.

[47] A. Amid, D. Mignard, and M. Wilkinson, "Seasonal storage of hydrogen in a depleted natural gas reservoir," *International Journal of Hydrogen Energy*, 2016.

[48] Z. Bo, L. Zeng, Y. Chen, and Q. Xie, "Geochemical reactions-induced hydrogen loss during underground hydrogen storage in sandstone reservoirs," *International Journal of Hydrogen Energy*, vol. 46, pp. 19998–20009, 6 2021.

[49] J. Andersson and S. Grönkvist, "Large-scale storage of hydrogen," Tech. Rep. 23, 5 2019.

[50] B. Nemati, M. Mapar, P. Davarazar, S. Zandi, M. Davarazar, D. Jahanianfard, and M. Mohammadi, "A sustainable approach for site selection of underground hydrogen storage facilities using fuzzy-delphi methodology," *Journal of Settlements and Spatial Planning*, vol. 2020, no. Special issue 6, 2020.

[51] A. Arvanitis, P. Koutsovitis, N. Koukouzas, P. Tyrologou, D. Karapanos, C. Karkalis, and P. Pomonis, "Potential sites for underground energy and CO2 storage in Greece: A geological and petrological approach," *Energies*, vol. 13, no. 11, 2020.

[52] K. Edlmann, S. Hinchliffe, N. Heinemann, G. Johnson, J. Ennis-King, and C. I. McDermott, "Cyclic CO2 - H2O injection and residual trapping: Implications for CO2 injection efficiency and storage security," *International Journal of Greenhouse Gas Control*, vol. 80, no. March 2018, pp. 1–9, 2019.

[53] G. M. Whitesides, "The origins and the future of microfluidics," 7 2006.

[54] N. K. Karadimitriou and S. M. Hassanizadeh, "A Review of Micromodels and Their Use in Two-Phase Flow Studies," *Vadose Zone Journal*, vol. 11, p. vzj2011.0072, 8 2012.

[55] B. Benali, "Quantitative Pore-Scale Analysis of CO 2 Foam for CCUS Master Thesis in Reservoir Physics," tech. rep., 2019.

[56] Y. T. Chow, G. C. Maitland, and J. P. Trusler, "Interfacial tensions of (H2O + H2) and (H2O + CO2 + H2) systems at temperatures of (298-448) K and pressures up to 45MPa," *Fluid Phase Equilibria*, vol. 475, pp. 37–44, 2018.

[57] A. E. Yekta, J. C. Manceau, S. Gaboreau, M. Pichavant, and P. Audigane, "Determination of Hydrogen-Water Relative Permeability and Capillary Pressure in Sandstone: Application to Underground Hydrogen Injection in Sedimentary Formations," *Transport in Porous Media*, vol. 122, no. 2, 2018.

[58] L. Hashemi, W. Glerum, R. Farajzadeh, and H. Hajibeygi, "Contact angle measurement for hydrogen/brine/sandstone system using captive-bubble method relevant for underground hydrogen storage," *Advances in Water Resources*, vol. 154, 8 2021.

Chapter 8

Appendix

werdtsertd beskrivelse

8.1 Appendix A

Image segmention algorithm
The function was developed in colloboration with Na Liu and is given below.

```
    function [saturation,new] = segmentation(fullfilename_I,
       img_bg_gray)
%SEGMENTATION: The function returns the hydrogen area from
   the subtracted image and the processed image in a logical
   matrix.
%image segmentation
%thresh=10; noise=300;close_holes=10;thresh2=1200;
%thresh=10; noise=2000 for part A;close_holes=10;thresh2
   =1200; %Treshhold if movements of the microscope/much
   noise with the above treshhold.


I = imread(fullfilename_I);
    I_gray = im2gray(I);
    J = I_gray - img_bg_gray;
    J1 = J > 10;
    %remove noise
    J2 = bwareaopen(J1,300);
    %close water holes
    se_disk = strel('disk',10); % radius=10
    J_close = imclose(J2, se_disk);
    new = J_close;
    %close small holes
    filled = imfill(J_close, 'holes');
    holes = filled & ~J_close;
```

```
    bigholes = bwareaopen(holes, 1200); %1000 pixels as
       threshold
    smallholes = holes & ~bigholes;
    new = J_close | smallholes;
    %figure
    %imshow(J1);
    %figure
   % imshow(new);
    %     %calculate #pixels
     totpx_void = numel(new)*0.515904225;%Porosity: update
        for each experiment
     new_H2 = sum(new(:));
     saturation = new_H2/totpx_void*100; %percent
end
```

The main script:

```
clc;
clear;
close all;

imageDir = 'Experiment 15/ex15_4054_image';

%image segmentation
files = dir(fullfile(imageDir,'*.jpg'));
N = length(files);


%%
%%
filename = "";
%collects the file names
for i=1:N
    file_content = string(struct2cell(files(i)));
    filename(i)= file_content(1); %1 for Ã¥ hente ut navnene.
end

%sorts the file names in natural order.
names = sort_nat(filename.'); %transpose. Copyright (c) 2008,
    Douglas M. Schwarz. All rights reserved.
names = names.';

%get the background image
%bg = files(1).name; %if background is the start of video.
bg_folder = 'Experiment 15/ex15_4054_image';
bg = '0001.jpg';
fullFileName_bg = fullfile(bg_folder, bg);
img_bg = imread(fullFileName_bg);
img_bg_gray = rgb2gray(img_bg);
%%initiation
%saturation = [1:N];
image = struct;

%specify the folder of the images
folder = files(1).folder; %all images are in the same folder
%%
 imageDir_filter = 'Experiment 15/ex15_filtered_4054';
 mkdir(imageDir_filter);

%image proceccing
for i=1:N
    fullfilename_I = fullfile(folder,names(i));
    %img_filtered = image.(sprintf('img%d',i));
```

```
    [saturation(i),image.(sprintf('img%d',i))]=segmentation(
       fullfilename_I, img_bg_gray);

    %%Saves filtered images to file
    baseFileName_2 = sprintf('%04d.jpg', i); % e.g. "
       filter_0001.jpg"
    fullFileName_filt = fullfile(imageDir_filter,
       baseFileName_2);
    imwrite(image.(sprintf('img%d',i)),fullFileName_filt,'JPG'
       );
end
%%
%saturation plot
time=1:N;
time_T = time.';%transpose to get them vertically
saturation_T = saturation.';%transpose

fig = figure;
plot(saturation);
xlabel('Time'), ylabel('H2 saturation(%)');
title('H2 saturation over time');
saveas(fig,imageDir_filter,'fig');
%%
%save saturation into a xlsx file
%Creates table
T = table(time_T,saturation_T);
%set properties
T.Properties.VariableNames{'time_T'}='Time';
T.Properties.VariableNames{'saturation_T'}='H2 saturation';
T.Properties.Description = 'Table that saves experimental
   data as a time series';
T.Properties.VariableDescriptions{'Time'}='Time steps (add
   unit)';
T.Properties.VariableDescriptions{'H2 saturation'}='Hydrogen
   gas saturation at the given time)';

description = ['Experiment 15. q = 2,5 mL/h. 40 bar.Cyclic
   injection i 5 cycles. Date:09.02.2022. '];


S = table({description}');  well.
S.Properties.VariableNames{'Var1'}='Experiment number: 15';
filename = 'Experiment 15/experiment15_data.xlsx';
%writes to file
writetable(S,filename,'Sheet','4154 Saturation','Range','A1',
   'AutoFitWidth',true);
writetable(T,filename,'Sheet','4154 Saturation','Range','A4',
   'AutoFitWidth',true);
```

Residual gas

End-point drainage and imbibition filtered images were analysed for each experiment by comparing the common area between drainage and imbibition for each cycle. A binary image of the intersection area was produced. The images were combined in one figure. The intersection area of the cycle was compared to the following cycle, and a binary image of residual gas during all cycles was created. The binary images were coloured to easier distinguish the processes.

```
close all;
clear;

N=5; %number of cycles.
%bg = imread('bg.jpg');
porosity = 0.446483652;
for i=1:N
drain_name = sprintf('C%d_drain.jpg',i);
imb_name = sprintf('C%d_imb.jpg',i);

im_drain = imread(fullfile(drain_name));
im_imb = imread(fullfile(imb_name));
%folder = sprintf('Ex15 C%d results',i);
%mkdir(folder);

RGB_imb = cat(3,im_imb*1, im_imb*0, im_imb*0); %(cat(3,R,G,B)
    %red
RGB_drain = cat(3,im_drain*0, im_drain*1,im_drain*1);  %drain
    magneta/blue

%imwrite(RGB_imb, fullfile(folder,sprintf('C%d_imb_RGB.jpg',i
   )));

%imwrite(RGB_drain, fullfile(folder,sprintf('C%d_drain_RGB.
   jpg',i)));
%Find colour: c = uisetcolor([0.6 0.8 1])

residual_bin = bitand(im_drain,im_imb); %common area (binary
   image, black and white)
%imwrite(residual_bin,sprintf('C%d_residual_bin.jpg',i));
RBG_rec = cat(3,residual_bin*1, residual_bin*0,residual_bin
   *1); % common area colour magneta
%imwrite(RBG_rec,fullfile(folder,sprintf('C%
   d_residual_bin_RBG_lila.jpg',i)));


% % Combine the images in 1
 fig = figure;
```

```
 %imshow(bg);
alpha(0.5);
hold on;
imshow(RGB_imb);
 hold on;
 alpha('color') %remove background
 imshow(RGB_drain) %add drainage image
 alpha('color')
 imshow(RBG_rec); %add common image to better observe colour.
     Not nesassary but a better colour contrast
 alpha('color');
 hold off;
%
 figname = sprintf('Ex 15 C%d residual',i);
 saveas(fig,figname,'jpg');


%residual gas
totpx_void = numel(residual_bin)*porosity;%Porosity: mean
   based on different labs with field of view.
residual_Sg= sum(residual_bin(:)>127);%
%black = sum(~white(:));
saturation_res(i) = residual_Sg/totpx_void*100;

%saturation draiange and imbibiton comparison
px_drain = sum(im_drain(:)>127); %<127 are black values.
px_imb = sum(im_imb(:)>127);
Sg_d(i) = px_drain/totpx_void*100;
Sg_i(i) = px_imb/totpx_void*100;

%relative to drainage
res_rel_drain(i)= saturation_res(i)/Sg_d(i)*100 ;%residual
   relative to drainage)

end

C1= imread('C1_residual_bin.jpg');
C2 = imread('C2_residual_bin.jpg');
C3 = imread('C3_residual_bin.jpg');
C4 = imread('C4_residual_bin.jpg');
C5 = imread('C5_residual_bin.jpg');

%common area of the cycles
res1 = bitand(C1,C2);
res2 = bitand(C2,res1);
res3 = bitand(C3,res2);
res4 = bitand(C4,res3);
res5 = bitand(C5,res4);
```

```
%count
%%
%count for each cycle comparison
residual_all(1) = sum(res1(:)>127)/totpx_void*100;
residual_all(2) = sum(res2(:)>127)/totpx_void*100;
residual_all(3) = sum(res3(:)>127)/totpx_void*100;
residual_all(4) = sum(res4(:)>127)/totpx_void*100;
residual_all(5) = sum(res5(:)>127)/totpx_void*100;

% %add colour
% RGB_res5 = cat(3,res5*0, res5*1, res5*0); %(cat(3,R,G,B) %
   pink
%
% %display and save
% fig = figure;
% imshow(RGB_res5);
% alpha('color');
% saveas(fig,'RGB_CommonAreaCycle1-5','jpg');
%%

%%
% Excel

cycle = 1:N;
%transpose
cycle = cycle.';
Sg_d = Sg_d.';
Sg_i = Sg_i.';
saturation_res = saturation_res.';
res_rel_drain = res_rel_drain.';
residual_all = residual_all.';

% S = table({description}'); %headline/description can be
   added to the file as well.
%S.Properties.VariableNames{'Var1'}='Experiments';
filename = 'ex15_residual gas.xlsx';%

T = table(cycle,Sg_d, Sg_i, saturation_res,res_rel_drain,
   residual_all);


T.Properties.Description = 'Ex15 residual gas extracted by
   combining end-point drainage and imbibition images in
   MATLAB.';

%description = 'Ex15 residual gas extracted by combining end-
   point drainage and imbibition images in MATLAB.';
%D = table(description);
```

```
writetable(T,filename,'Sheet',' Residual hydrogen ex15 v2','
   Range','A3','AutoFitWidth',true);
```

8.2 Appendix B

Uncertainties have been calculated for the measurements and calculations performed in this thesis. Uncertainties was calculated by standard deviation, uncertainty for a function and combined uncertainty:

Standard deviations for a sample N of a population:

$$std(x) = \sqrt{\frac{\sum_{i=1}^{N}(x_i - \bar{x})^2}{N-1}} \tag{8.1}$$

Uncertainty of a function f(x,y):

$$u(f(x,y)) = \sqrt{(\frac{\delta f}{\delta x}\Delta x)^2 + (\frac{\delta f}{\delta y}\Delta y)^2)} \tag{8.2}$$

Combined uncertainty:

$$u_T(x,y) = \sqrt{u(x)^2 + u(y)^2} \tag{8.3}$$

Relative uncertainty:

$$u_R(x) = \frac{u_T(x)}{x} \tag{8.4}$$

The uncertainty of the saturation based on the filtered images was calculated by:

$$\Delta x = \frac{S_{gm} - S_{gf}}{S_{gm}} \cdot 100\% \tag{8.5}$$

where the difference between the hydrogen saturation from filling in manually (S_{gm}) and the returned saturation from the script (S_{gf}) relative to S_{gm}. The combined uncertainty includes both the uncertainty of the filter (for constant saturations) and the uncertainty of the filter compared to manually mapping of hydrogen.

8.3 Appendix C

Saturation developments for cyclic injection for different capillary numbers are presented in the following figures. The time is the effective time when gas injection and withdrawal was performed.

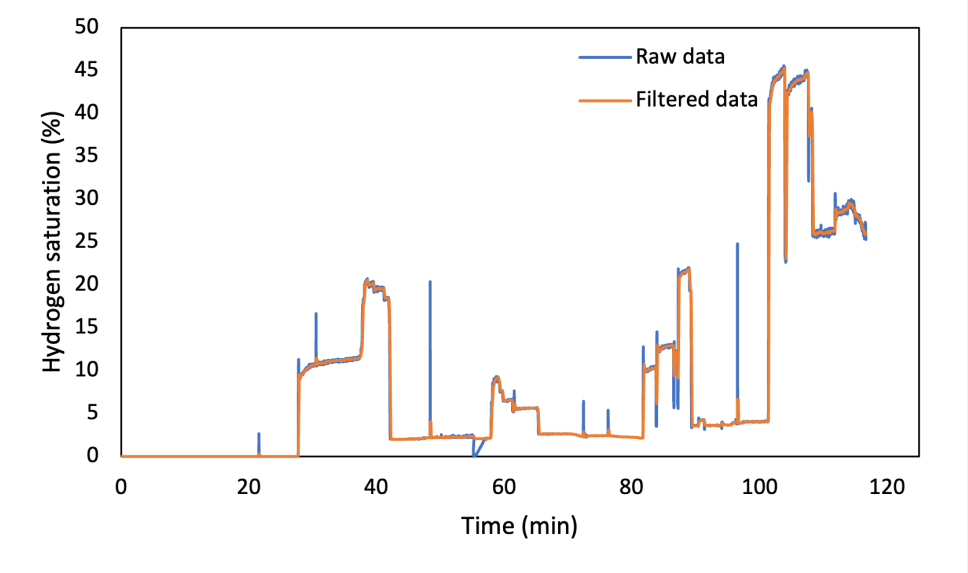

Figure 8.1: Hydrogen saturation for exp. B5-1 at $N_c = 7.59 \cdot 10^{-6}$.

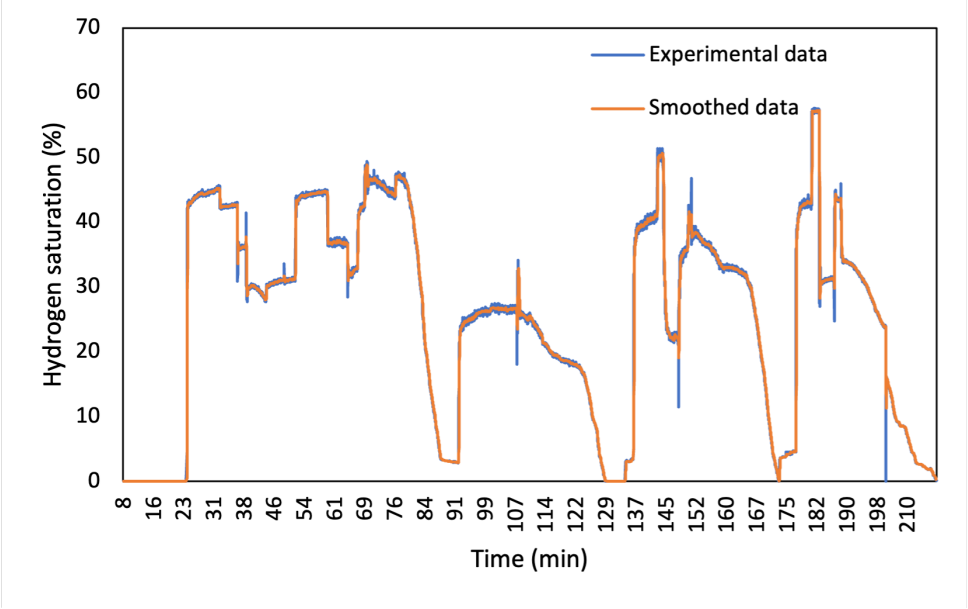

Figure 8.2: Hydrogen saturation for exp. B6-1 at $N_c = 1.90 \cdot 10^{-5}$.

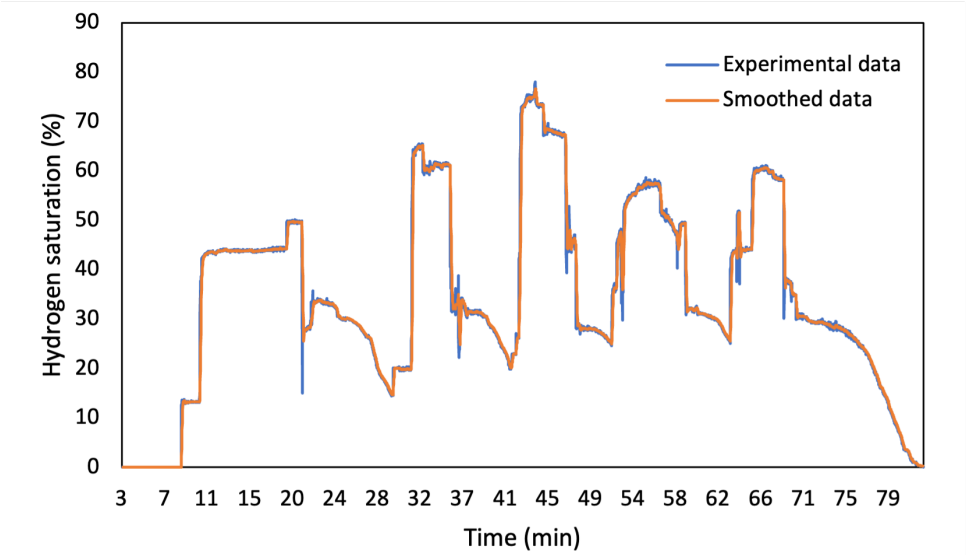

Figure 8.3: Hydrogen saturation for exp. B7-2 at $N_c = 3.80 \cdot 10^{-5}$.

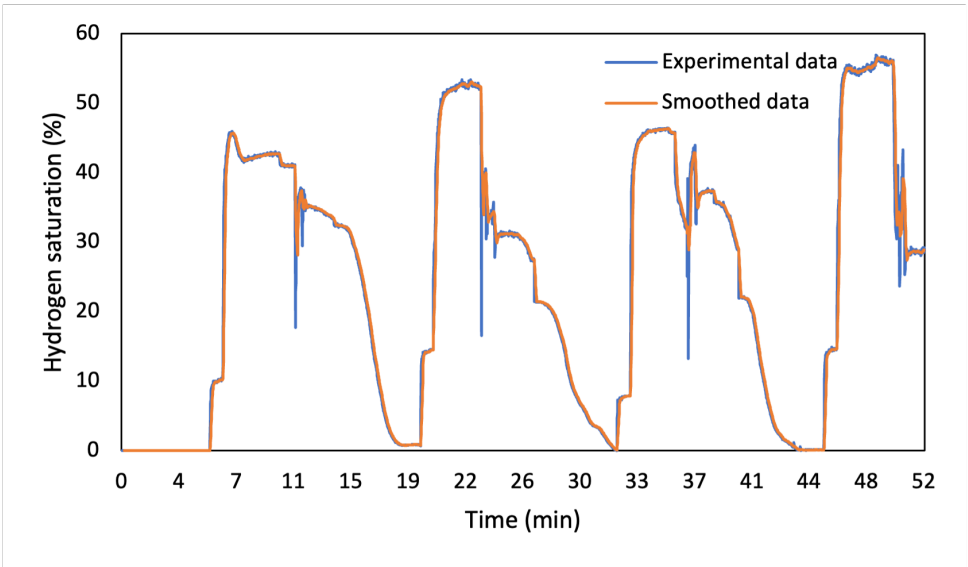

Figure 8.4: Hydrogen saturation for exp. B8-1 at $N_c = 7.59 \cdot 10^{-5}$.